AN ABSTRACT OF THE THESIS OF

Aristotel Popescu for the degree of Doctor of Philosophy in Mechanical Engineering presented on November 30, 2000. Title : An Experimental Study of Fluid Flow and Heat Transfer in Rectangular Microchannels.

Redacted for privacy

Abstract approved: _____
James R. Welty

This thesis reports on an experimental study of fluid flow and heat transfer in high aspect ratio, rectangular microchannels. A single channel with width of 10 mm was cut into polycarbonate spacers of various thickness, resulting in channel depths of 128 μm, 263 μm and 521 μm.

Tests conducted in the range of Re = 100 – 3800 showed friction factors generally larger, and transition to turbulence occurring at lower Reynolds numbers than predicted for macroscale channels. Experimental values of the friction constant were $\overline{f \cdot Re} = 24.2$ for an aspect ratio α^* = 20:1, $\overline{f \cdot Re} = 26.1$ for α^* = 40:1, and $\overline{f \cdot Re} = 26.0$ for α^* = 80:1, compared with classical values of 22.4, 23.2, and 23.6, respectively.

Heat transfer experiments were performed with a constant heat flux boundary condition from the bottom surface of the channel. Experiments conducted for Re = 300 – 900 and Pr = 3.6 – 3.8 showed small or no departure from macroscale predictions for channels with hydraulic diameters larger than 500 μm. Results for the 80:1 aspect ratio channel showed a significant departure from theoretical predictions. Experimental values of local Nusselt numbers were approximately 25 percent lower than predicted using macroscale theory. A computer code was developed to model the solution for energy equation in laminar flow, and predict asymptotic values for the laminar Nusselt number.

An Experimental Study of Fluid Flow and Heat Transfer in Rectangular Microchannels

by

Aristotel Popescu

A THESIS

submitted to

Oregon State University

in partial fulfillment of
the requirements for the
degree of

Doctor of Philosophy

Presented November 30, 2000
Commencement June 2001

Doctor of Philosophy thesis of Aristotel Popescu presented on November 30, 2000.

APPROVED

Redacted for privacy

Major Professor, representing Mechanical Engineering

Redacted for privacy

Head of Mechanical Engineering Department

Redacted for privacy

Dean of the Graduate School

I understand that my thesis will become part of the permanent collection of Oregon State University libraries. My signature below authorizes release of my thesis to any reader upon request.

Redacted for privacy

Aristotel Popescu, Author

ACKNOWLEDGEMENTS

Without the support of the following people, the work presented in this dissertation would not have been possible. For this reason, I would like to extend my sincere appreciation to the Department of Mechanical Engineering for continued financial support throughout the duration of my Ph.D. program, and to United States Department of Energy, through the Pacific Northwest National Laboratory (PNNL), for funding the research project from which this work originated.

I would also like to express my gratitude to the members on my committee, John Lee, Richard Peterson, Deborah Pence and Erik Skyllingstad, who provided insightful comments, encouragement and construction criticism. A special and respectful thought goes for the memory of Dwight J. Bushnell.

Most importantly, I would like to thank my advisor, James R. Welty, for his support, encouragement, and general guidance in my professional development. An outstanding educator and recipient of numerous awards for excellence in engineering education, he was willing to mentor me from both a research and a teaching perspective, even after his retirement from full academic service on December 31, 1996. He had a decisive influence over my future, and I was proud to have him as advisor and mentor. Being the last graduate student in his 42 year-long professional career, it is my pleasure to say: Thank you professor Welty! You saved the best for last!

Special thanks are extended to Gordon M. Reistad for his understanding and support throughout the program. I would like to thank Debbie Jimmerson, DyAnn McVicker for their help with student-related issues, and Steve Adams, Ken McCraken for technical assistance. Special thanks are also extended to my colleagues Kent Enfield for software assistance, Bertrand Dano for hardware assistance, and Brian Daniels for ideas and encouragement. Thanks are extended to Deborah Pence for assistance in uncertainty analysis, and to Jim Liburdy and members of MICROS group for insightful discussions.

I would like to thank David M. Pfund for his substantial help and pertinent observations throughout the experimental work and data analysis performed at PNNL. Continuous support from David Rector and Alireza Shekarriz, as well as technical assistance provided by Bill Combs and Mike White is greatly appreciated. Special thanks are extended to my friends Karl Seely, and Katarina and Chance Younkin.

Thanks are extended to my Romanian friends in Oregon and Washington, especially to Dan Onu and his wife Monica, Cleo and George Hirsovescu, and Peter Kiss and his wife Erika, for spiritual and material support, and for the wonderful moments we spent together in the last four years.

Finally, I would like to thank my wife, Mihaela Popescu, for her love and affection, and for sacrifices to provide a warm and familiar environment in our home away from home. Special thanks are extended to my brother, Gabriel-Eduard Popescu and to my parents, Iulia and Petru-Miltiadi Popescu, for their unconditional love and support, not only for the last few years, but always.

TABLE OF CONTENTS

LIST OF FIGURES

LIST OF FIGURES (Continued)

LIST OF TABLES

LIST OF APPENDICES

LIST OF APPENDIX FIGURES

LIST OF APPENDIX TABLES

NOMENCLATURE

Latin symbols

A	area
a	half width of the channel
b	half height of the channel
C_f	friction constant
c_p	specific heat
D	diameter
D_h	hydraulic diameter
F_m, G_n	constants for infinite series
f_D	Darcy friction factor
f_F	Fanning friction factor
H	channel height
h	heat transfer coefficient
k	thermal conductivity
L	length
$\dot{m}$	mass flow rate
n	normal direction
P	perimeter
p	pressure
q'	axial heat flux
q''	heat flux
R	electrical resistance
R_h	hydraulic radius
r, r_0	pipe radii
t	temperature
U	electrical power
$\dot{V}$	volumetric flow rate
W	width
u, v, w	velocity components
x	axial distance
x, y, z	orthogonal coordinate system

Dimensionless groups

Kn	Knudsen number
Nu	Nusselt number
Pe	Peclet number
Pr	Prandtl number
Re	Reynolds number

Greek symbols

α	thermal diffusivity
α^*	aspect ratio
β	grid aspect ratio
Γ	boundary
γ_m, λ_n	eigenvalues
Δ	difference
δ	boundary layer thickness
ε	benchmark error
μ	viscosity
ρ	density
τ	shear stress
θ	dimensionless temperature (Dirichlet boundary condition)
Θ	dimensionless temperature (Neumann boundary condition)
ω	uncertainty

Superscripts

$^+$	dimensionless
^{n}	iteration number

Subscripts

app	apparent
c	cross-section
e	entrance
fd	fully developed
hy	hydraulic
i,j	identifiers for grid nodes
H	specified heat flux
m	mean (average)
max	maximum
T	specified temperature
th	thermal
w	wall
x	local values

This thesis is dedicated to
my loving wife,
Mihaela Popescu

AN EXPERIMENTAL STUDY OF FLUID FLOW AND HEAT TRANSFER IN RECTANGULAR MICROCHANNELS

1. INTRODUCTION

Things normally start small and then grow. The life cycle of every living creature goes from small at birth, and grows through childhood, to maturity. Human habitats have grown from houses, to buildings, to skyscrapers. Our ability to travel has increased from a few miles on foot, to horses, to trains and airplanes, and now we can encircle the world or explore outer space.

We live in a macro world. The traditional machines we use everyday can be seen with the naked eye, can be touched with the human hand. In short, we have a direct interaction with this macromechanical world. The size of the machines in our macro world spans many orders of magnitude, ranging from sub-millimeter parts applied in watches, to machines that measure several hundred meters, such as commercial airplanes or oil tankers. Probably the world's largest machines are particle accelerators, like the LEP (large electron positron ring) at CERN in Geneva, with a diameter of 27 kilometers (van der Schoot, 1995).

Yet, in the last few decades, researchers and scientists have adventured toward the small end of the scale. It is clear from examining many major industries that one of the most significant trends of the last half of this century has been miniaturization. This has reduced the cost of products in real terms, while dramatically increasing the size and diversity of the market.

There is a striking difference between the products manufactured in late 1940s and the ones made in 1990s. The increase in efficiency and safety, ease of use and maintenance, and lower price are some of the undisputed features of the today's products. But, probably, the most obvious one is the decrease of the dimensions.

Even if the size of products has not decreased markedly, as with motor vehicles for example, the miniaturization of components has made it possible for many new features to be stuffed into the same space. Smaller engines with higher power output leave enough room in the engine compartment for power steering, power brakes, ABS, and electronic fuel injection. Also, the on board computer, safety systems, and environmental control systems are making the driver's life easier and more pleasant.

Similar comments apply to the aerospace industry, transportation, chemical plants and other process industries, where downsizing is not obvious but major improvements have been made to achieve improved safety, cleaner environment, and automation. Miniaturization allows chemical reactions to occur much more rapidly than in conventional reactors, because micro-instruments require minuscule volumes of reactants.

The most extraordinary progresses in miniaturization are made possible by advances in semiconductor technology (Service, 1996). In 1965, Intel Corp.'s co-founder Gordon Moore tossed out the kind of long-range prediction that makes most scientists squirm. Noting early trends in the fledgling microelectronics industry, Moore predicted that the number of transistors on computer chips would double every 18 months, thanks largely to continuous advances in techniques for carving features on silicon wafers, or lithography. Moore's prediction, which industry analysts soon dubbed "Moore's Law," turned out to be oddly prescient. The number of transistors on chips has, in fact, doubled about every 18 months for the past 35 years, helping to propel semiconductor production into a $150-billion-per-year industry (Figure 1.1.).

Microchips have miraculous power to miniaturize. Miniaturization begins with the transistor, which was invented in 1947 and exploded with the 1959 invention of the integrated circuit, a device incorporating multiple transistors on a single silicon chip the size of a fingernail. The earliest model transistor was smaller than the smallest vacuum tube it was meant to replace, and not needing a filament - it consumed far less power and generated virtually no waste heat. And there was almost no limit to how small it could be

made, once engineers learned how to etch electronic circuits, almost atom by atom, onto substrates of silicon. As late as the 1950s, the standard kitchen-table radio (AM only) had five vacuum tubes and a few dozen minor parts-resistors, capacitors and coils-hand-wired and individually soldered onto a chassis about the size of a hardcover book (Adler, 1997). Today that circuitry fits into a matchbook, while a microprocessor smaller than a postage stamp can carry the equivalent of 7.5 million transistors. The first silicon chips compressed computers from rooms full of vacuum tubes and relays into devices the size of a hardback book.

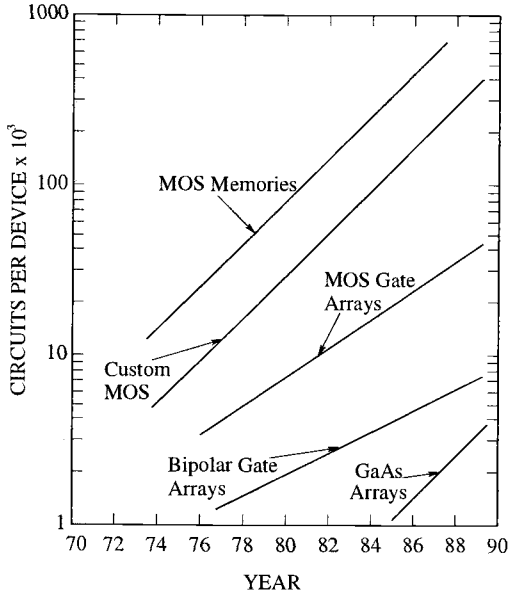

Figure 1.1. Semiconductor trends: circuits per chip (Hanemann, 1990)

The limiting factor in making most electronic appliances smaller is not the size of the electronic components but the human interface. There's no point in reducing the size of a laptop much further, pending the evolution of humans with smaller fingers. Today the impulse for computer miniaturization is no longer portability, but the speed of computation itself, i.e. reducing the time it takes an electronic signal, traveling at a substantial fraction of the speed of light, to get from one part of the circuit to another.

Now microchips of another sort are poised to perform the same feat of downsizing on analytical laboratories. Sorting out a sample's chemical constituents, sequencing DNA, or searching for mutations in a gene now requires benches laden with equipment. But if several researchers have their way, these tasks may soon require nothing more than a battery pack, some cunningly crafted microchips, and a digital readout.

Lots of small products are manufactured worldwide. How small is small? It is now possible to construct an entire gas chromatograph on a single semiconductor chip (Cotter, 1984), a two-dimensional laser array on a chip whose total area is less than 10 mm^2 (Peterson *et al.*, 1991), and a heat pump the size of a dime (Wegeng *et al.*, 1995). Miniaturization of electronics will make it possible to receive, transmit, and process data on wireless, handheld computers. Forerunners of nano-technology will involve medical devices - things put unobtrusively into your body to do something without hooking you up to a machine - something going via a needle tip into a vein or a tiny implant sampling your blood or measuring pH and wirelessly transmitting the results. Miniaturization creates enormous opportunities to put things precisely where they are needed.

Microelectromechanical Systems (MEMS), Micro Systems Technologies (MST, primarily in Europe), Mechatronics (primarily in Japan) and Micromanufacturing are relatively recent phrases that have become synonymous with the design, development, and manufacture of very small devices and systems. The function of these devices ranges from micro sensor elements to micro energy systems (Wegeng *et al.*, 1995). Also, an important micromanufacturing technology is the packaging of devices and sensors. Several existing technologies have been adapted to the miniaturization of structures, devices and systems, such as complementary micromachining (micromilling, microdrilling), bulk and surface micromachining of silicon, laser and focused ion beam micro-machining (Frazier *et al.*, 1995). Also, new technologies have been developed to meet the requirements of micromanufacturing, such as X-ray micromachining using the LIGA process (a German acronym: Röntgen**LI**thographie **G**alvanik **A**bformung, meaning X-ray lithography electrodeposition molding), and micro-electroplating (Joo *et al.*, 1995).

Microstructure technology has practical applications in many fields, including bioengineering and biotechnology, aerospace, communications, automobiles, energy, materials processing and manufacturing, environmental technologies etc. Also, it may provide new tools for a closer examination of thermal phenomena, often considered very difficult or impossible to investigate due to small length scales. Recent decades have witnessed rapid progress in research related to micro- and nano-scale transport phenomena, with important applications in technologies such as microelectronics.

The introduction of microelectronics in the form of LSI (Large Scale Integration), VLSI (Very Large Scale Integration) and ULSI (Ultra Large Scale Integration) technologies, which offer increasing number of gates per chip, has generally allowed the volume occupied by electronic equipment to decrease. The demand for faster circuits and increased capacity, however, has led to both increases in power dissipation of each circuit, and an increase in the number of circuits per unit volume. The net result has been increasing power densities at the chip (Figure 1.2.), module, and system levels of packaging, and a need for continuous improvements in the methods of heat removal. The expected life of a solid-state device depends on operating temperatures and also on temperature cycling, making the cooling problem even more challenging. The management of thermal environment at all structural levels of the electronic equipment must be coordinated to achieve this goal.

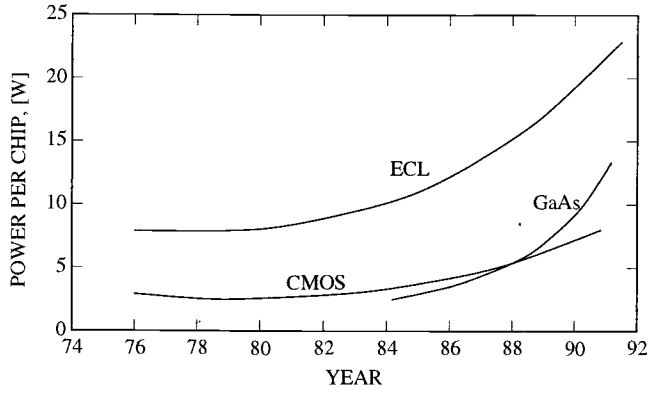

Figure 1.2. Power dissipation trends (Hanemann, 1990)

As for high-density microelectronic devices, there are other applications with contradictory requirements for high rates of heat dissipation accompanied by low allowable temperature rises. Increased circuit-component densities have raised heat dissipation rates to around 100 W/cm^2. This level of heat flux is comparable to that from a nuclear blast, but must be accommodated at a much lower temperature (Figure 1.3.).

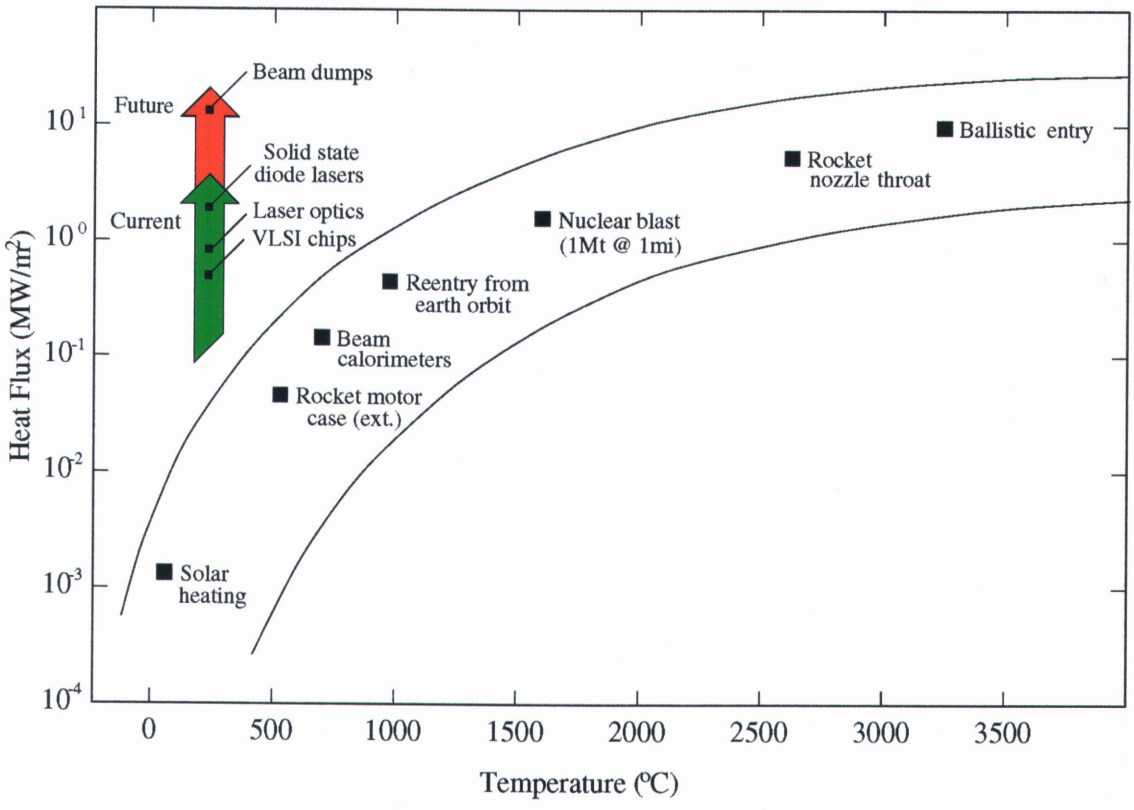

Figure 1.3. Perspective on microelectronic heat fluxes

Although transistor switching energies have decreased, these decreases have not kept pace with the increase in component density. Increases in the chip thermal conductivity or in the material to which the chips are attached have strong influences on thermal characteristics, and may significantly enhance the overall chip reliability. With the rapid progresses in microelectronics and the continuous demand for high-heat-flux

cooling researchers have been forced to look for new methods and techniques for heat removal. Air is a convenient coolant, but incapable of removing the high-heat-fluxes expected in the future generations of high-speed computers. Therefore, the new models of mainframe computers have already employed advanced cooling systems.

One innovative cooling technique that meets these requirements is the microscale heat sink. Advances in microfabrication technology allow the manufacturing of micro-heat exchangers consisting of multiple minute flow conduits with hydraulic diameters ranging from 10 to 10^3 μm. These micro-heat exchangers are characterized by extremely high surface area per unit volume of working fluid, low thermal resistance, low mass and low volume. Also, low inventory of working fluid is required. Their main disadvantage is the susceptibility to fouling, which requires the use of very clean working fluids.

A fundamental understanding of flow and heat transfer behavior on the microscale is essential for efficient design and analysis of systems and devices utilizing microstructures. Toward this end, the fundamental processes of fluid dynamics and heat transfer in microgeometries have received considerable attention in recent decades. The most attractive phenomenon related to scale is an apparent reduction of the friction factor and an increase in the heat transfer rate, compared to macroscale behavior. These advantageous characteristics have been applied to the development of heat exchangers, evaporators, and condensers, which are required of most thermal/fluid systems.

D.B. Tuckerman and R.F.W. Pease, at Stanford University, first introduced the concept of a "microchannel heat sink" in a paper published in 1981. Since then, several other researchers have published theoretical and/or experimental works, generating a significant amount of information in the area of microscale flow and heat transfer processes. The heat transfer between the coolant and the heat sink contributes a significant fraction of the total thermal resistance in electronic component packages.

Then, what is the purpose of the present work?

The analysis of heat transfer in microstructures is essential for their successful design and fabrication. Often it is not known whether heat transfer in microstructures can be analyzed with macroscale theories, i.e., methods which do not consider dependence of the transport mechanism on the structure dimension.

If macroscale heat transfer theory is applied to a microstructure in a situation for which it is inappropriate, then a significant error in the calculated heat transfer can result. Such an error can render the device to be non-functional or cause it to perform in a sub-optimal manner. If the thermal conductivity of thin films in a multi-layer electronic chip is overestimated, then the heat removal rate during chip operation can be lower than expected, yielding an operating temperature that is too high and results in a degradation of chip performance. The designer of microstructures must have a criterion to decide whether macroscale heat transfer theory can be applied to a given device or if microscale theory must be used.

Recently, microscale heat transfer phenomena have received intensive interest due to the emergence of thermal microsensors, high-temperature superconductive films, micro heat pipes, micro heat exchangers, etc. The studies published thus far have presented neither a microscale heat transfer theory that is generally applicable to microstructures, nor conditions or criteria upon which it is possible to decide whether or not macroscale theory is applicable for a microstructure.

At this time, the differences in fundamental mechanisms are highly speculative, as results presented are inconclusive due to discrepancies between various investigations. Wu and Little (1983, 1984) reported friction factors greater than classical values for laminar and turbulent gas flow through channels etched in silicon and glass, a premature transition to turbulence, and slightly higher heat transfer rates. They suggested that this might be due to the high relative roughness of the surfaces. Urbanek *et al.* (1993) also showed that friction factors were higher than predicted by theory, without providing any explanation. The data presented in these two studies conflict with other investigations.

The University of Pennsylvania group (Harley and Bau, 1989, Pfahler *et al.*, 1990a, 1990b, 1991) showed that as channel depth decreased, there was deviation from macroscale theory yielding higher laminar friction factors that changed with Reynolds number. Choi *et al.* (1991) measured friction factors in microtubes with inside diameters of 3 – 81 μm using nitrogen gas. They found that, for small tube diameter, the friction factor constant was $f \cdot Re = 53$ instead of 64 as for macrochannels. Yu *et al.* (1995) confirmed that the friction factors are lower than predicted by macroscale theory. Harley and Bau (1989) experimentally measured friction factors in channels of trapezoidal and square cross sections. They found that C_f ranged from 49 for square channels to 512 for trapezoidal ones. The results of Wu and Little (1983) indicated a transition from laminar to turbulent flow at Reynolds number of 400 – 900. Peng *et al.* (1994a) found experimentally that transition to turbulent flow began at Re = 400 to 1500, with smaller values for smaller size channels.

A few papers have reported more radical differences between classical theory (macroscale behavior) and experiments on laminar flows in microchannels. Some authors have reported friction factors varying as Re^{-1} (classical behavior) with one investigation reporting f to vary as $Re^{-1.98}$ (Peng *et al.*, 1994a). Nitrogen gas flow was in agreement with predicted behavior, but for silicone oil the product $(f \cdot Re)$ was not constant. Pfahler *et al.* (1990a) suggested that this result was due to the fact that silicone oil is a non-Newtonian fluid.

As mentioned above, experimental results that have been published to date by various authors are limited and sometimes contradictory. One problem is that the experiments involved a specific configuration. Theoretical analyses, presented to date, have described system behavior using macroscale models. There is insufficient data in the literature to answer basic questions as to the effect of microchannel geometry on fluid flow and heat transfer behavior, the constitutive relationship between flow rate and friction pressure losses, or the characteristics of fluid-flow-regime transitions or heat transfer regime transitions.

As presented extensively in a succeeding chapter dealing with a review of the literature, data published to date cover a wide variety of geometrical configurations, substrate materials, fluids used, fluid flow rates and temperatures. The geometry of the channels varies from circular cross section (Choi *et al.*, 1991, Yu *et al.*, 1995) to square (Harley and Bau, 1989, Peng and Wang, 1993), rectangular (large majority of the cited references), trapezoidal (Rujano and Rahman, 1995) and V-shaped (Peterson *et al*, 1991). The size of the channels varies over a very wide range starting with micron sizes (Choi *et al.*, 1991) going up to millimeter (10^3 μm) sizes (Adams, 1997). Some authors are concerned with small channels, in the millimeter range. Various methods were used to manufacture the microchannels: micromachining, etching, chemical etching, laser, and lithographic methods. Substrate materials varied also: glass (Wu and Little, 1983), silicon, copper (Goldberg, 1984), aluminum (Kishimoto and Ohsaki, 1986), nickel, stainless steel (SS316), brass, indium phosphide (Phillips, 1990), and titanium. Fluids used include gases, such as air (Mahalingham, 1985), nitrogen (Harley *et al.*, 1995, Yu *et al.*, 1995), hydrogen, argon; and liquids, such as water, silicon oil, refrigerants, methanol and liquid nitrogen.

The work presented in this thesis has been done with the goal of establishing and clarifying the differences between system behavior at microscale dimensions compared to the macroscale and to confirm theoretical predictions with experimental data.

Experimental variables have been carefully identified and controlled. All components of the test apparatus have been carefully chosen to minimize experimental measurement errors. The test loop used was designed so that quantitative experimental data would be augmented by qualitative observations through a flow visualization system (video photo microscopy) of the phenomena occurring in the microchannel.

2. LITERATURE REVIEW

A search of the literature, in an attempt to extract any organized collection of applied mechanics problem, is by no means an easy task. Moreover, the majority of heat transfer problems have not as yet been solved to a satisfactory degree, due to the interrelationship of many geometrical and operative parameters. Under these circumstances, the present chapter will provide only a chronological presentation of the work that has been done and what appears to lie ahead in the area of fundamental research in microscale fluid flow and heat transfer.

The body of literature is very large, and most of the reports are written from the viewpoint of equipment developers. Moreover, no list and exposition of research topics can be comprehensive within a reasonable length.

2.1. Microchannel fluid flow and heat transfer

D.B. Tuckerman and R.F.W. Pease, at Stanford University, first introduced the concept of a "microchannel heat sink" in a paper published in 1981. Since then, several other researchers have published theoretical and/or experimental works, generating a significant amount of information in the area of microscale flow and heat transfer processes. The heat transfer between the coolant and the heat sink contributes a significant fraction of the total thermal resistance in electronic component packages. It has been widely recognized that increasing the area of the heat sink in contact with the coolant can enhance the heat transfer and, therefore, the use of fins is common. However, it has not been generally recognized that for laminar flow the heat transfer coefficient is inversely proportional to the width of the channel.

Tuckerman and Pease (1981a, 1981b, 1982) designed and tested a very compact, water-cooled heat sink for silicon integrated circuits. At a power density of 790 W/cm^2, a maximum substrate temperature rise of 71°C above the input water temperature was measured. By allowing such high power densities, it was predicted that this heat sink could greatly enhance the feasibility of ultrahigh-speed VLSI circuits. The design of these heat sinks was optimized using the presented theory, the resulting configuration having a channel width of 57 μm, channel height of 365 μm, and wall thickness of 57 μm. The channel configurations used in the experimental investigation had channel widths of 50 μm to 56 μm and heights of 287 – 320 μm. A Pyrex cover plate was anodically bonded over the channels and manifold.

Wu and Little (1983) measured friction factors for the flow of gases in fine channels used for micro-miniature Joule-Thomson refrigerators. The test microchannels (width 130 – 200 μm; depth 30 – 60 μm) were fabricated using photolithographic techniques. Silicon and glass were used as substrate materials, with nitrogen, hydrogen and argon used as cooling fluids. The tests involved both laminar and turbulent flow regimes. The results showed different characteristics than those expected in traditional flows. This was attributed to surface roughness in the channels. It was observed that the rougher the surface of the channel, the earlier the transition from laminar to turbulence occurred. Transition Reynolds numbers were Re = 900 for a glass substrate with treatment, and Re = 350 for glass substrate without treatment. Comparisons were made with the Moody chart for round pipes.

Subsequently, Wu and Little (1984) published their results of measurements of the heat transfer characteristics of gas flow in micro heat exchangers. Microchannels in the counterflow heat exchangers were fabricated using the same photolithography technique as in their former work. Channel dimensions were different this time, widths being about 500 μm with depths of 100 μm. Tests were conducted for both laminar and turbulent flow regimes. The results indicated that for the channels heated on one side, the position of the heat source did not appear to be a significant factor in determining the heat transfer in turbulent flow, while for the laminar zone it appeared to have some effect.

The transition zone occurred at Re = 1000 to 3000. The average heat transfer coefficient was larger for the two-sides heated channel than for one-side heated channel. Roughened channels demonstrated higher heat transfer coefficients, but the friction factor was higher also. Tests showed Reynolds' analogy not to be valid for the rough channels tested.

Acosta *et al.* (1985) studied mass and momentum transport characteristics in large-aspect-ratios channels with widths ranging from 188 to 508 μm. The experimental data obtained in both laminar and turbulent flow (Re = 1300 – 22,000) through roughened and nearly smooth microchannels indicated that roughness does not affect laminar flow performance, but significantly affects the turbulent flow performance. According to the author, there is no good theory to predict the hydrodynamics of rough surfaces.

Hwang *et al.* (1987) proposed a thermal module design as a basis for a high performance, high power dissipation vehicle suitable for VLSI/ULSI applications. Water flowing through the channels in the underlying structure removes the heat generated in chips. Twenty-seven channel designs were studied and, finally, two optimal designs were considered: 1000 μm deep (5066 μm width) and 100 μm shallow (4600 μm width) channels. The water flow rate of 499 cm^3/s and 39 cm^3/s, respectively, insured a maximum temperature rise of 19°C relative to the inlet water temperature.

Nayak *et al.* (1987) continued the work of Hwang *et al.* (1987). Their results confirmed the findings of the previous work. For the deep channel design, the maximum device temperature rise was 18°C for a power dissipation of 42 W/chip and a flow rate of 126 cm^3/s. For the same power dissipation, the shallow channel design had a temperature rise of 19°C for a flow rate of 19 cm^3/s.

Harley and Bau (1989) measured friction factors in a channel having a trapezoidal cross-section of 33 μm deep and 63 μm / 111 μm wide, and in a rectangular channel of 50 μm in width and 100 μm deep. Planar photolithographic micro-machining techniques were used to produce the channels in a silicon wafer. In contrast with the classical value of ($f \cdot Re$) = 48, friction constant values were found, experimentally, to range from 49 for rectangular channels to 512 for the trapezoidal channels.

Harley *et al.* (1989) extended the previous work to smaller channels, with depths of 1.7 μm and 0.8 μm, and a width of 100 μm. Experimental observations for the 1.7 μm deep channel are in rough agreement with theoretical predictions. However, in the case of a 0.8-μm-deep channel, the friction constant was found to be about three times larger than the theoretical value, and values of C decreased with increase in Re. The authors assumed that the difference was due to the deviations from Navier - Stokes predictions, but they fail in predicting the critical value of the channel size.

Missaggia *et al.* (1989) operated a two-dimensional GaInAsP / InP diode laser array with high power dissipation (up to 500 W/cm^2) into a silicon microchannel heat sink. A value of 0.070°C cm^2/W was obtained for the thermal resistance. By halving the coolant temperature, the optical output power was more than doubled. The total output power obtained in this manner exceeded that of more efficient array mounted on a copper heat sink at room temperature. The channels were 400 μm deep and 100 μm wide. Water was used as coolant, at a flow rate of 20 cm^3/s ($Re \approx 2000$) and a pressure drop of 482 kPa along the microchannels.

Bier *et al* (1990) reported on a technology to build compact cross-flow micro heat exchangers made of aluminum alloys, copper, stainless steel and titanium. Using water as the working fluid, it was possible to transfer (in a cubic transfer volume of 1 cm^3) about 20 kW at mean logarithmic differential temperature of about 60 K. This corresponded to volumetric heat transfer coefficients of more than 300 MW/m^3-K. The maximum value was 324 MW/m^3-K, corresponding to a heat transfer coefficient of from water to water of approximately 22,800 W/m^2-K, at a water flow rate of 12.5 l/min.

Pfahler *et al.* (1990a) conducted an experimental investigation of fluid (liquid and gas) flow in extremely small channels. This investigation was one of a series to determine the fundamental characteristics of friction in liquid and gas flow in small channels. It was found that in relatively large flow channels, the experimental observations were in rough agreement with the predictions from Navier-Stokes equations. However, for the smallest of channels, a deviation from Navier-Stokes equations was observed.

Pfahler *et al* (1991) continued the efforts in this area and presented measurements of the friction factor or apparent viscosity of fluids for flow of isopropyl alcohol and silicone oil in channels of 0.5 μm to 50 μm depth. Results showed that resistance to fluid motion, or apparent viscosity, was consistently smaller than predicted by conventional incompressible theory. Also, for liquids, the apparent viscosity decreased with decreasing channel depth. While for the largest channel the experimental results indicated very good agreement with theoretical predictions, as the channel size decreased, the apparent viscosity had lower values than predicted by theory for a given pressure drop. Distinctly different behavior was observed between the non-polar silicone oil and polar isopropyl alcohol. Results of gas flow indicated a similar difference between the measured friction factor and incompressible theory predictions. A trend of decreasing friction factor with decreasing Reynolds numbers was observed.

Weisberg *et al.* (1990) conducted a theoretical study of heat transfer in multiple channel devices with uniformly distributed heat sources. This study indicated that the heat transfer coefficient attained a local maximum at the midpoint (both height and width) of the channel. As a result, more heat will flow upward in the fin and the fin temperature tends to be more uniform than predicted by the constant-heat-transfer-coefficient model. This will be especially true when the thermal conductivity of the solid is much larger than that of the liquid.

Wang *et al.* (1991) experimentally confirmed the work of Peterson *et al.* (1991), and evaluated the thermal performance and hydraulic resistance of two micro heat exchangers using a hot/cold water test loop. Different materials and different aspect ratios (width/depth of 15:1 for SS316, and 1.25:1 for brass, respectively) were used for heat exchangers. Pressure drops were found to be proportional to the fluid axial velocity, as expected, but the entrance length was much shorter than expected. The effect of the thermal entrance length on heat transfer was more obvious in the SS316 case than for brass case. This is due to the material conductive heat transfer coefficient. Measured volumetric heat transfer coefficients were as high as 2.3 MW/m^3-K (SS316) and 7 MW/m^3-K (brass). The Nusselt numbers were independent of Reynolds number for

the brass micro heat exchanger and increased with Reynolds number for the SS316 micro heat exchanger. The authors concluded that the size of the channels and the materials used are of importance for designing micro heat exchangers.

Choi *et al.* (1991) investigated the friction factor, inner wall roughness, and convective heat transfer coefficients for laminar and turbulent nitrogen gas flow in microtubes with inside diameters ranging from 3 μm to 81 μm. Experimental results indicated significant departures from correlations used for conventionally-sized tubes. For microtubes having inside diameters smaller than 10 μm, the friction correlation ($C = f \cdot Re$) produced a value of $C = 53$ rather than 64. Measured Nusselt numbers for convective heat transfer in turbulent flow were as much as seven times the values predicted by the traditional macro-scale analysis. One suggested reason for this result was the suppression of the turbulent eddy motion in the radial direction, due to small channel diameters. Measured heat transfer coefficients in laminar flow exhibited a Reynolds number dependence, in contrast to the conventional predictions for fully established laminar flow, in which Nusselt number is constant.

Flik *et al.* (1991, 1992) published a work showing regime maps delineating the boundaries between macroscale and microscale heat transfer regimes. These maps relate the geometric dimensions separating the two regimes to temperature for conduction in solids; to temperature, pressure and Reynolds number for convection in gases; and to temperature of the emitting medium for radiative heat transfer. Material purity and defect structure strongly influences the regime boundaries. Microstructures pertaining to a given technology are marked on these maps to determine whether macroscale heat transfer theory is applicable.

Arpaci (1992) proposed a new thermal microscale to relate the microscales and the integral scales to heat transfer correlations. The new *mesomicroscale* was developed to clarify the foundations of correlations on the turbulent forced convection for fluids (gases, liquids and oils). Also, a heat transfer model for $Pr \geq 1$ is proposed and tested. The results revealed that the model agrees very well with the experimental data as well as with all earlier correlations developed without any references to microscales.

Beskok and Karniadakis (1992) present a numerical method to simulate time dependent slip-flow for values of Knudsen number less than 0.1 in complex micro-domains encountered in micro-devices. Navier-Stokes and energy equations were as the governing equations. However, in the lower Knudsen number limit (with small deviation from the Maxwellian standard distribution for molecular motion) the Navier-Stokes equations were modified using the Chapman-Enskog theory for the transport coefficients. Also, in the higher Knudsen number limit the only closed form equation that is strictly applicable is the Boltzmann equation. The validation of the method was obtained by comparing the numerical results for simple prototype flows (Poiseuille, Couette) with analytical solutions. The results demonstrate that a simulation approach can be employed to efficiently predict momentum and energy transport in micro-devices.

Peng and Wang (1993), Wang and Peng (1994), Peng *et al.* (1994b) and Peng *et al.* (1995) have investigated single-phase flow in rectangular microchannels (600 μm x 700 μm) with water or methanol as the working fluid. They found that the transition from laminar to turbulent flow regime occurred at about $Re \approx 1000 - 1500$, which is notably lower than the value observed in macroscale flow ($Re \approx 2500$). In fully developed turbulent flow, the heat transfer coefficient for one test section could be described using the well-known Dittus - Boelter correlation, simply by adjusting the coefficient from the value of 0.023 (for macroscale data) to the value of 0.00805. However, their data generally showed radically different behavior from the predictions based on macroscale flow and heat transfer models. The authors concluded that single-phase convection on the microscale is distinctly different from the behavior observed in conventional macroscale flow in tubes and channels. The heat transfer rates are significantly augmented on the microscale, and are affected by local fluid properties, fluid velocity and channel geometry.

Bowers and Mudawar (1994a; 1994b), Gersey and Mudawar (1995a; 1995b), and Sturgis and Mudawar (1999a; 1999b) conducted tests in rectangular microchannels with internal diameter of 510 μm and in mini-channels of internal diameter of 2.54 mm, using refrigerant R-113 or FC-72 as working fluids. The results showed a relatively low

pressure drop in the mini-channel, even in boiling flow, while for the microchannel tests, a very large increase in pressure drop was encountered in two-phase flow. Based on wall temperature behavior, the heat transfer regime was assumed to be that of nucleate boiling. A distinct critical heat flux was observed on the order of 200 W/cm^2.

Peng and Peterson (1995) experimentally investigated the effect of geometry on single-phase forced convection for a range of microchannel sizes. The microchannel depth was 700 μm and the width varied from 200 – 800 μm. Results showed heat transfer in the laminar and transition flow regimes in the microchannels to be significantly different from the behavior observed in macroscale channels. For some conditions, the transition from laminar flow occurred for $Re \approx 300$ and the flow became fully turbulent at $Re \approx 1000$. The transition boundary and heat transfer behavior in both laminar and transition flow regimes were found to be strongly affected by the liquid temperature, liquid velocity and the microchannel size.

Peng and Peterson (1996a) continued their research in the area of microchanneled structures and presented the experimental results on single-phase forced convective heat transfer and flow characteristics of water in microchannel structures/plates with small rectangular channels having hydraulic diameters of 0.133 – 0.367 mm for distinct geometric configurations. The results indicated that the geometric configuration has a significant effect on the single-phase convective heat transfer and flow characteristics.

Yu *et al.* (1995) continued the work of Choi *et al.* (1991), and performed a series of experiments systematically measuring pressure drop across microtubes with diameters of 19, 52 and 102 μm, for Reynolds number ranging from 250 to over 20,000. They found that laminar flow friction factor could be expressed as a function of Reynolds number using the relation $f = 53/Re$, for tests with both nitrogen and water. Results showed the pressure drop across the microtube to be lower than for a conventional macroscale tube, where the friction factor is described by the relation $f = 64/Re$.

Cuta *et al.* (1996) conducted an experimental study of heat transfer and pressure drop in a microchannel heat exchanger. Refrigerant R-124 was used as working fluid in 1 mm deep and 0.27 mm wide microchannels. Conditions tested included a range of Reynolds numbers between 100 and 570, uniform heat flux up to about 40 W/cm^2, in both single-phase and two-phase flow. Results showed a significant increase of the heat transfer coefficient above the expected value in macroscopic flow for the same Reynolds number range. In single-phase flow, Nusselt number increased with Reynolds number, while remaining approximately constant in two-phase flow. The overall results showed substantial improvement thermal performance of miniature size heat exchangers, without significant penalty in pressure drop.

Peng and Peterson (1996b) also conducted experiments for binary mixtures (water and methanol), for the same geometrical configurations. It was found that the laminar heat transfer ceased at Re = 70 – 400, depending upon the flow conditions, and fully turbulent convective heat transfer was achieved at Re = 200 – 700, function of the hydraulic diameter of the microchannel. Again, the authors found that the channel geometry has a significant influence on the fluid flow and heat transfer characteristics.

Shih *et al.* (1996) examined flow through a very small channel, 40 μm wide and 1.2 μm high, manufactured using fabrication procedures similar to those for producing integrated circuit chips. Mass flow rates of the fluids (helium and nitrogen gases, high Knudsen numbers – larger than 0.01) were of the order of 10^{-12} kg/s (low Reynolds numbers – of the order of 10^{-2}). The authors modeled the flow using the Navier-Stokes equations together with a slip boundary condition. The helium data are in reasonable agreement with the slip flow model, except for the inlet pressure. The nitrogen results deviate from theoretical predictions, and the authors did not explain these discrepancies.

Adams *et al.* (1997) investigated turbulent, single-phase forced convection of water in circular micro channels. Channel diameters were 0.76 mm and 1.09 mm; water inlet velocities ranged from 3 to 19 m/s (corresponding to Reynolds numbers of 3200 and 23,000), while the Prandtl numbers ranged from 4.21 to 6.43. Nusselt numbers for

the 0.76-mm channel were significantly higher than those predicted by traditional large channel correlations. Data for the 1.09-mm channel deviated from predicted macroscopic behavior, but the deviation was significantly less than in the 0.76-mm case.

Harms *et al.* (1997) obtained experimental results for single-phase forced convection in deep microchannels. The channels tested were 251 μm wide and 1030 μm deep, chemically etched in a silicon substrate measuring 2.5 cm by 2.5 cm. All tests were performed using deionized water as the working fluid, where the liquid flow rate ranged from 5.47 cm^3/s to 118 cm^3/s. A critical Reynolds number of 1500 was found.

Kawano *et al.* (1998) experimentally and theoretically examined the performance of microchannel heat exchanger systems used for cooling electronic components. The experimental setup consisted of an array of 110 channels (57 μm wide and 180 – 370 μm deep, with a 100 μm pitch) etched in silicon. For Reynolds numbers in the range 0 – 200 the measured pressure drop was in good agreement with the analytical results obtained based on the assumption of fully developed laminar pipe flow. For $Re > 200$, the values obtained experimentally were slightly higher than the theoretical predictions.

Papautsky *et al.* (1998a, 1998b) used a numerical model based on micropolar fluid theory (includes the effect of fluid molecules on the continuum) to describe fluid flow behavior and experimentally verified the model using micromachined channels. Experimental data were obtained for room-temperature water with Reynolds numbers in the 1 to 100 range. The data indicated an increase in the friction factor, especially at low Reynolds numbers. The channels were 12,750 μm long, 1500 μm wide and 30 μm deep.

Webb and Zhang (1998) assessed the ability of existing correlations to predict single-phase and two-phase heat transfer and friction in channels having small hydraulic diameters, between 0.1 and 2.0 mm. Existing equations overpredict the data obtained by Wang and Peng (1994). The authors have developed an equivalent Reynolds number model that improved predictions for small diameter tubes, from 0.96 to 2.13 mm. However, it was stated that more data are needed for channel diameters less than 1.0 mm.

This review suggests that there are several hydrodynamic and thermal effects that should be considered on the microscale. For gas flow in very small channels, the continuum assumption may break down when the mean free path is of the order of the channel dimensions. At these channel sizes, wall relative roughness, fluid viscosity, and fluid polarity become important factors. Also, it is not clear at what order of dimensions slip flow becomes important. In addition, two- and three-dimensional effects must be considered, as the characteristic lengths are reduced to the same order of magnitude as the thickness of thermal or hydrodynamic boundary layer.

Generally, the continuum equations that express conservation of mass, momentum and energy break down for finite values of *Kn*. Considering the flow of air (mean free path ~ 10^{-7}m) associated with characteristic dimensions varying from 100 μm to 0.1 μm, the corresponding Knudsen number varies from 0.001 to 1. In the lower Knudsen number limit (mesoscale), the deviation from continuum behavior is still sufficiently small and the Navier-Stokes equations, with minimal modifications, may be used with good accuracy. However, it has been found that in the higher limit of Knudsen number (microscale) the only closed equation that is strictly applicable is the Boltzmann equation that involves molecular velocities as the dependent parameters, instead of the macroscopic quantities.

Based on the relevant investigations in single-phase microscale fluid flow and heat transfer several conclusions can be made.

- There is no universally accepted theory to predict the behavior of liquid flow in microchannels.
- Friction factors in laminar flow are apparently lower that macroscale predictions.
- The Reynolds analogy appears to be invalid in the microscale regime.
- Turbulent heat transfer is apparently higher than predicted by macroscale theory.

2.2. Macrochannel fluid flow and heat transfer

In the previous section, comparisons between microscale behavior and macroscale theory were made. Scientists have shown that even at the macroscale, theory cannot take into account all phenomena that occur in fluid flow and heat transfer in rectangular channels. The following papers describe some of these phenomena.

Clark and Kays (1953) considered the problem of laminar flow heat transfer in tubes of rectangular and triangular cross-section. A numerical relaxation method was used to obtain limiting magnitudes of the Nusselt number. Boundary conditions of both constant heat input and constant wall temperature were examined. Experimental data are presented for square tubes with both constant temperature and constant heat input wall conditions, and, for a rectangular tube of aspect ratio 2.62, for constant wall temperature. These data, together with the limiting Nusselt number results, provide a rational basis for estimating entrance length effects for rectangular tubes, and result in a correlation for Nusselt number applicable to the design of gas-flow heat exchangers.

In a short communication, Schmidt and Newell (1967) have presented additional values of the Nusselt number for fully developed laminar flow through rectangular and isosceles triangular ducts of various aspect ratios. Two types of boundary conditions were investigated: constant wall temperature and constant heat flux per unit length with a uniform wall temperature for the conducting surfaces at each cross-section. Results were also obtained for configurations where one or more walls were adiabatic. Assumptions made to determine the magnitude of Nusselt number were: fully developed profiles for velocity and temperature, constant fluid properties, no viscous dissipation, negligible natural convection, and negligible axial heat conduction. Results were in good agreement with the work of Clark and Kays (1953). The Nusselt number, for infinite parallel plates, in the case of constant heat flux boundary condition is 8.2353 (analytical method) and 8.2351 (numerical method) for both sides conducting, and 10.7692 (analytical method) and 10.7696 (numerical method) for one side conducting and one adiabatic.

Bhatti and Savery (1977) studied the problem of simultaneous development of velocity and temperature fields in a straight channel with uniform heat flux. The analytical solution to the flow development problem was based on the application of macroscopic mechanical energy equation in the entrance region. The temperature field was determined using the Karman - Pohlhausen method. Local Nusselt numbers were calculated for nine Prandtl number fluids and an asymptotic value of 35/17 was reached for fully developed flow and temperature conditions. The comparison between the analytical predictions for the local Nusselt number of previous investigators and the present analysis shows a maximum deviation of 15 percent. For the most part, the results of the analyses agree within 5 percent. The authors found the local Nusselt number predictions of various investigators to be in close agreement with one another. Therefore, it appeared that, in the entrance region of a straight channel, heat transfer rates are rather insensitive to momentum diffusion rates.

Bhatti and Savery (1978) developed a semi-analytic solution to the problem of simultaneously developing velocity and temperature fields in a straight channel with uniform wall temperature. Heat transfer results were calculated for 11 fluids covering the Prandtl number range from 0.01 to 10,000. Local Nusselt numbers approached an asymptotic value of 1.5, and the mean Nusselt number approached an asymptotic value of 1.9. Calculated results were in good agreement with reports of previous investigators.

Osborne and Incropera (1985) published an experimental study to determine hydrodynamic and thermal conditions in laminar flow of water between horizontal parallel plates with uniform, asymmetric heat fluxes. Flow visualization and temperature measurements revealed the existence of a buoyancy-driven flow, which strongly influenced bottom plate condition, but had a weak influence on top plate conditions. Heat transfer at the top plate was dominated by forced convection, while heat transfer at the bottom plate was characterized by mixed convection, with heat transfer coefficients exceeding those associated with pure forced convection by as much as a factor of seven. For the range of heat fluxes considered, top and bottom plate flow conditions were independent of the heat flux at the opposite plate.

Maddox and Mudawar (1989) performed experiments to assess the feasibility of cooling microelectronic components by means of single-phase and two-phase forced convection. An inert fluoro-carbon liquid (FC-72) was circulated upward through a vertical rectangular channel at velocities up to 4.1 m/s. Their results demonstrated that the low thermal resistances required for cooling microelectronic heat sources could be achieved with single-phase forced convection using high fluid velocity coupled with surface enhancement.

2.3. Microfabrication techniques

The transition from our macro world to the micro world is accompanied by surprises and changes in perspective. Micro manufacturing is fundamentally different from large-scale manufacturing, thus scientists and engineers working in the microscale area have been forced to develop new techniques to manufacture microdevices.

In surface micromachining technology, layers are deposited and patterned on a substrate. Sacrificial material is deposited where open areas or clearance tolerances are desired; structural material is deposited where the final part is desired. After deposition, the sacrificial material is removed, and the desired mechanical device remains.

In bulk micromachining, the wafers used by the electronics industry are sliced from a single pure crystal of silicon. Under the correct conditions, chemicals etch the different crystallographic planes within the silicon at different rates. This anisotropic etching usually removes material from the faces of {1 1 1} planes much more slowly than other planes. This differential etching and ingenuity allow the fabrication of a wide range of parts. Clever design, corner compensation, and careful control of the rate at which different planes etch into each other can form a variety of shapes. More complicated shapes can be obtained by bonding different wafers and other materials. Anodic bonding and silicon fusion bonding are two of the most popular methods for bonding wafers together. Both methods require high-temperatures.

The LIGA process exposes poly-methyl methacrylite plastic with synchrotron radiation through a mask. The exposed plastic is then washed away, leaving vertical wall structures with spectacular accuracy. Structures measuring 1/3-millimeter high and several millimeters on a side can be made accurate to a few tenths of a micron. Metal is then plated onto the structure, replacing the washed away plastic. This metal piece can become the final part or can be used as an injection mold for parts made out of a variety of plastics.

There are many papers published to date describing processes for specific applications. The following papers were reviewed due to their general character, as information for the common reader, and not for the manufacturing engineer.

Kaminsky (1985) describes refined and very exact processing procedures for manufacturing geometrically highly precise silicon structures. The processing procedure is refined using a specially designed etching system utilizing wet chemical orientation and concentration etching techniques. The structures have excellent large and small-scale uniformity. The author reports production of features as small as 0.2 μm.

Ehrfeld *et al.* (1987) described the LIGA process and associated principles of fabrication. Figures presented in the paper show an increased accuracy of the features manufactured and the authors analyze the potential fields of application for microstructure products: micro-filtration, carrier structures, synthetic fibers, microoptics, sensors and actuators.

Bier (1990) described a mechanical method for manufacturing microstructural bodies based on the surface shaping of foils by precision cutting with microtools. Electron beam welding, laser welding, and diffusion bonding of micro heat exchangers were performed. The method of construction consisted of generating patterns on foil surfaces by precision cutting with profiled microdiamonds. The next step was to join the foils to become a microstructural body. These compact cross-flow micro heat exchangers made of aluminum alloys, copper, stainless steel and titanium have a wide spectrum of

applications that extends from collimators for X-rays, microfilters, microcatalyzer supports, to perforated microstructural bodies with up to 40,000 holes/cm^2, micro heat pipes and finned plate micro heat exchangers.

Hoopman (1990) reported on the development of several proprietary processes, for fabricating structures containing microchannels. These structures could be planar or three-dimensional. Typical microchannels had hydraulic diameters of 10 mm to 1mm, with length-to-diameter ratios of 50 to 5000. Microchannel center-to-center distances were geometry dependent and could be as small as 100 μm. The electrical discharge machining (EDM) process was successfully used to fabricate plates with micro fins containing one microchannel, which are particularly well suited for liquid/gas heat exchangers. The process had been used to make copper and nickel microchanneled structures. Another process presented is used to make round microchannels and has the capability of producing channels that vary in shape and/or size along the length of the channel.

Wise (1991) examined fabrication technologies and proposed future technologies associated with microelectromechanical systems (MEMS). One by one, bulk and surface micromachining, wafer-to-wafer bonding and electroforming technologies (LIGA) are described. Even if the author describes their applications to micro-sensors and actuators fabrication, it is mentioned that these methods offer the designer a rich array of processes for the creation of microstructures in batch and with very high precision.

Dario *et al.* (1995) outlines the motivations for developing new microfabrication technologies, especially those considered as "non-traditional" in the microelectronics domain, and the perspectives offered by this approach for fabricating miniature, micro and nanodevices. These methods are intended to overcome the limitations of planar silicon technology. The authors consider four representative "non-traditional" technologies: LIGA process, micro electro-discharge machining (EDM), micro stereo lithography, and the combination of biological and artificial microfabricated structures ("hybrid technologies").

3. THEORETICAL APPROACH

The purpose of this chapter is to review the conventional hydrodynamic flow and heat transfer theories and correlations used for pipe flow. The discussion will be extended to include channel flow and heat transfer in rectangular channels of various aspect ratios. The applicable differential equations and boundary conditions for velocity and temperature are for steady, laminar flow through constant-cross-section ducts.

3.1. Hydrodynamic fluid flow theory

The velocity distribution of a fluid flowing through a duct will undergo a development from the initial profile at the entrance of the duct to a fully developed profile at a location far downstream (Figure 3.1.). Correspondingly, the pressure gradient in the region will differ from that of a fully developed flow. The pressure decreases as a result of the wall shear stress and the change in momentum.

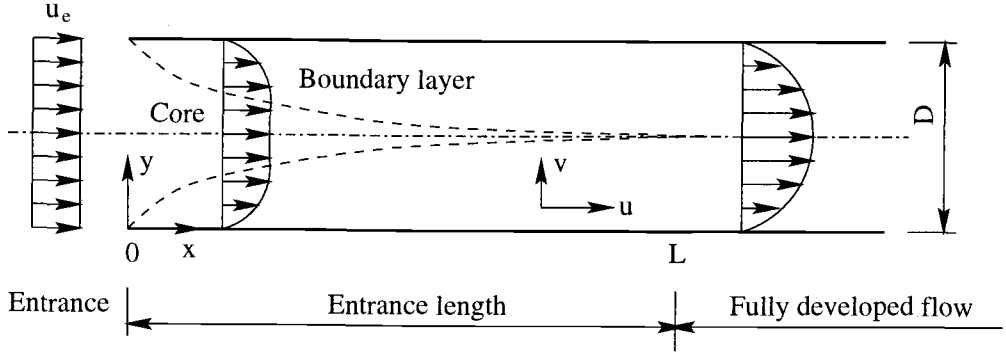

Figure 3.1. The developing flow in the entrance region of a duct

Flow is said to be *laminar* when the velocities are free of macroscopic fluctuations at any point in the laminar flow field. Laminar flow, also referred to as viscous or streamline flow, is characteristic of a viscous fluid flow at low Reynolds number. For steady state laminar flow, all velocities at stationary points in the flow field remain constant with respect to time.

The laminar flow in a two-dimensional stationary straight duct is designated as *hydrodynamically fully developed* when the fluid velocity distribution at a cross-section is of an invariant form, i.e. independent of the axial distance x.

The *boundary layer thickness* (δ) for flow over a flat plate is defined as the distance from the wall where the velocity is 99 percent of the free stream value. For pipe flow, the boundary layer starts at the tube entrance and will continue to grow until the shear layers meet.

The *hydrodynamic entrance region* of a duct is that region where the velocity boundary layer is developing from zero thickness at the entrance to the pipe radius far downstream. In this region, the velocity profile changes from the initial profile at the entrance to an invariant form downstream, as a result of the viscous fluid behavior. In this region, the flow is designated as hydrodynamically developing. The hydrodynamic entrance length is defined as the duct length required to achieve velocity or pressure development within a given range (usually 1 percent) of the corresponding fully developed values. The central portion of the velocity profile generally develops more slowly than the portion of the profile adjacent to the wall. Therefore, the hydrodynamic entrance length is defined here as the length necessary to achieve a centerline velocity equal to 99 percent of the fully developed value.

Most of the analytical studies on this region involve approximations such as neglecting the cross-stream velocities, in order to solve the continuity and momentum equations simultaneously. Experimental velocity and pressure measurements cited by Hartnett and Kostic (1989) have noted that approximate solutions using the linearization

method predict faster developments in velocity and pressure distributions, whereas the numerical methods that take into account the cross-stream velocities show better agreement.

Consider a stationary duct with the boundary Γ. The fluid flowing through it is idealized as liquid or low-speed gas with fluid properties ρ, μ, c_p, and k constant (i.e., independent of fluid temperature). In this case, the continuity equation must be solved simultaneously with Navier - Stokes equations. In the absence of gravitational effects, terms in the y and z momentum equations are an order of magnitude smaller than the corresponding terms in the x momentum equation and thus may be neglected. For this case, pressure is a function of x only.

The corresponding conservation equations for incompressible flow are

$$\frac{\partial u}{\partial x}+\frac{\partial v}{\partial y}+\frac{\partial w}{\partial z}=0 \tag{3.1.}$$

$$u\cdot\frac{\partial u}{\partial x}+v\cdot\frac{\partial u}{\partial y}+w\cdot\frac{\partial u}{\partial z}=-\frac{1}{\rho}\cdot\left(\frac{dp}{dx}+\frac{dp}{dy}+\frac{dp}{dz}\right)+\nu\cdot\left(\frac{\partial^2 u}{\partial x^2}+\frac{\partial^2 u}{\partial y^2}+\frac{\partial^2 u}{\partial z^2}\right) \tag{3.2.}$$

Assuming no-slip at the wall and that the velocity profile is uniform at the entrance, then:

$$u,v,w=0 \quad \text{on} \quad \Gamma \tag{3.3.}$$

$$u=u_e=u_m \quad \text{at} \quad x=0 \tag{3.4.}$$

For fully developed, steady state, laminar flow in a two-dimensional duct the momentum equation (3.2.) reduces to

$$\frac{\partial^2 u}{\partial y^2}+\frac{\partial^2 u}{\partial z^2}=-\frac{1}{\mu}\cdot\frac{dp}{dx}=\text{const.} \tag{3.5.}$$

The *fluid mean axial velocity* is defined as the integrated average axial velocity with respect to the cross-section flow area, A_c:

$$u_m = \frac{1}{A_c} \cdot \int_{A_c} u \cdot dA \tag{3.6.}$$

As expressed in Kays (1966), the *local shear stress* at the wall for a Newtonian fluid flowing through a duct is

$$\tau_w = -\mu \cdot \left(\frac{\partial u}{\partial n} \right)_w \tag{3.7.}$$

The local wall shear stress is defined as the average wall shear stress with respect to the perimeter of the duct. In particular, for axisymmetric flow in a rectangular duct (Figure 3.2.), at any cross section x, is expressed as

$$\tau_x = -\frac{\mu}{2 \cdot (a+b)} \cdot \left[\int_{-a}^{a} \left(\frac{\partial u}{\partial y} \right)_{y=b} dz + \int_{-b}^{b} \left(\frac{\partial u}{\partial z} \right)_{z=a} dy \right] \tag{3.8.}$$

The flow length average (mean) wall shear stress is defined as

$$\tau_m = \frac{1}{x} \cdot \int_0^x \tau_x \cdot dx \tag{3.9.}$$

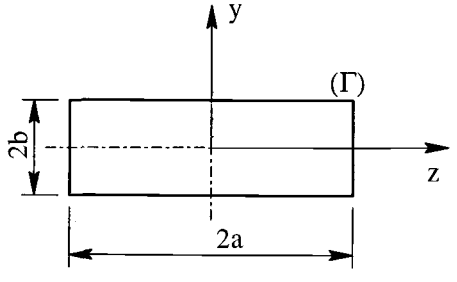

Figure 3.2. Cross-section geometry of the rectangular duct

The *Darcy friction factor* relates roughness effects to pressure drop in pipes and is defined by

$$f_D = \frac{8 \cdot \tau_w}{\rho \cdot u_m^2} \tag{3.10.}$$

The Darcy - Weisbach equation is derived by solving the energy and momentum equations for fully developed pipe flow and combining the result with the Darcy friction factor equation. This equation is used to determine pressure drop in pipes. The Darcy - Weisbach equation holds true for both laminar and turbulent flow.

$$\Delta p = f_D \cdot \frac{L}{D_h} \cdot \frac{\rho \cdot u_m^2}{2} \tag{3.11.}$$

For steady, laminar, fully-developed flow in round pipes the Darcy friction factor becomes

$$f_D = \frac{64}{Re} \tag{3.12.}$$

The *Fanning friction factor*, f_F , is an alternative form, commonly found in the chemical engineering literature. These two friction factors are related by

$$f_D = 4 \cdot f_F \tag{3.13.}$$

The region of developing flow has a higher pressure gradient than the fully developed flow region. This is easy to determine by considering the definition of wall shear stress. Near the entrance, the boundary layer is very small. At the wall, the velocity equals zero ("no-slip" condition), and at a short distance away the velocity is 99% of the free stream value. The change in velocity with respect to the radial direction is very large, which means that the shear stress is large. This condition relates to a larger friction factor and, thus, a higher pressure gradient in this region.

For the case of fully developed flow, the velocity profile is invariant at any cross section along the duct. Therefore, the pressure drop along a distance (L) of the duct is

$$\frac{\Delta p}{\rho \cdot u_m^2/2} = f \cdot \frac{L}{R_h} \tag{3.14.}$$

In the above equations, the hydraulic diameter is used so that the equations may be used for various cross-sections. The hydraulic diameter is proportional to the ratio of cross-section area and wetted perimeter, and is defined as

$$D_h = \frac{4 \cdot A_c}{P_{wetted}}, \qquad R_h = \frac{D_h}{4} = \frac{A_c}{P_{wetted}} \tag{3.15.}$$

The Reynolds number (Re_{D_h}) based on hydraulic diameter is defined as

$$Re_{D_h} = \frac{\rho \cdot u_m \cdot D_h}{\mu} \tag{3.16.}$$

Using the above definitions, and based on the solution of the differential equation, for the fully developed region it can be shown that

$$\left(f \cdot Re_{D_h}\right) = -\frac{1}{\mu} \cdot \frac{dp}{dx} \cdot \frac{D_h^2}{2 \cdot u_m} = \text{const.} \tag{3.17.}$$

where the constant is dependent on the geometry of the duct cross section.

The *dimensionless hydraulic axial distance* in the flow direction for the hydrodynamic entrance region is defined as

$$x_{hy}^{+} = x/\left(D_h \cdot Re\right) \tag{3.18.}$$

The *hydrodynamic entrance length* (L_{hy}) is defined as the duct length required to achieve a duct section maximum velocity of 99% of the corresponding fully developed magnitude, when the entering flow is uniform. The dimensionless hydrodynamic entrance length is expressed as

$$L_{hy}^{+} = L_{hy} / (D_h \cdot Re) \tag{3.19.}$$

The fully developed laminar velocity profile and friction factor of a Newtonian fluid in simple geometries, such as circular tubes or parallel plates, can be easily obtained by solving the one-dimensional momentum equation. In contrast, the two-dimensional analysis required for fluid flow in rectangular ducts is more complex. The analytical solution is available in the literature (Marco and Han, 1955).

Shah and London (1978) and Hartnett and Kostic (1989) made a summary of previous works, showing that the given equation for the velocity profile

$$u_{(y,z)} = \frac{16a^2}{\pi^3} \cdot \left(\frac{-dp/dx}{\mu} \right) \cdot \sum_{i=1}^{\infty} \left[\frac{(-1)^{i-1}}{(2i-1)^3} \right] \cdot \left\{ 1 - \frac{\cosh\left[(2i-1) \cdot \pi y / 2a \right]}{\cosh\left[(2i-1) \cdot \pi b / 2a \right]} \right\} \cdot \cos \frac{(2i-1) \cdot \pi z}{2a} \tag{3.20.}$$

involves considerable computational complexity. The approximate solution suggested in the literature to describe the laminar velocity profile is

$$\frac{u}{u_{max}} = \left[1 - \left(\frac{y}{b} \right)^m \right] \cdot \left[1 - \left(\frac{z}{a} \right)^n \right] \tag{3.21.}$$

The exponents m and n in equation (3.21.) have been evaluated solving the continuity and momentum equations using finite difference methods and matching the velocity profile to the empirical equation.

$$m = \begin{cases} 2 & \text{for } \alpha^* \le 1/3 \\ 2 + 0.3 \cdot (\alpha^* - 1/3) & \text{for } \alpha^* > 1/3 \end{cases}$$

$$n = 1.7 + 0.5 \cdot (\alpha^*)^{-1.4} \qquad \text{for } 0 \le \alpha^* \le 1 \tag{3.22.}$$

The agreement between the approximate equation and the exact series solution is within 2 percent over most of the cross section, but close to the corners the difference may be above 35 percent. The greatest difference is encountered in the case of square duct. Also, should be noted that

$$\frac{u_{max}}{u_m} = \left(\frac{m+1}{m}\right) \cdot \left(\frac{n+1}{n}\right) \tag{3.23.}$$

Bailey (1996, Table 3.1.) presents the values of laminar friction factor for various rectangular channel aspect ratios, α^*, where $0 < \alpha^* < 1$.

Table 3.1. Laminar friction constant for various aspect ratio rectangular channels

α^*	$(f \cdot Re_{D_h})$
0.000	96.00
0.050	89.91
0.100	84.68
0.125	82.34
0.167	78.81
0.250	72.93
0.400	65.47
0.500	62.19
0.750	57.89
1.000	56.91

Shah and London (1978) have presented an equation for the Fanning friction factor that is accurate within 0.05 percent of analytical value:

$$f \cdot Re = 24 \cdot \left[1 - 1.3553 \cdot \alpha^* + 1.9467 \cdot (\alpha^*)^2 - 1.7012 \cdot (\alpha^*)^3 + 0.9564 \cdot (\alpha^*)^4 - 0.2537 \cdot (\alpha^*)^5\right] \quad (3.24.)$$

The apparent friction factor accounts for both the wall shear stress and momentum change caused by the developing velocity profile. Hartnett and Kostic (1989) showed that the analytical predictions for the developing flow in rectangular-shaped channels were generally higher than experimentally determined values.

To account for developing flow in the mathematical model, the x^+ ratio is calculated for the length of the tube. Next, ($f_{app} \cdot Re_{D_h}$) is found by linear interpolation between the tabulated values presented in the literature (e.g., Bailey, 1996). Langhaar has derived a correlation (Welty *et al.*, 1984) that expresses, analytically, the entrance length required for fully developed laminar flow, according to

$$\frac{L_{hy}}{D_h} = 0.0575 \cdot Re \quad (3.25.)$$

In many situations flow is never fully developed, thus the friction factor will be higher than that predicted from equations for fully developed flow.

3.2. Heat transfer theory

Laminar flow heat transfer rates in ducts depend on the duct geometry, flow inlet velocity and temperature profiles, and wall temperature and/or heat flux boundary conditions. These conditions are difficult to produce even in the laboratory. This subchapter discusses the theoretical base needed to interpret experimental results. However, it is recognized that this theory is founded on idealizations of geometry and boundary conditions that are not necessarily well duplicated in applications or in the laboratory. In this review, the effects of natural convection, phase-change, mass transfer, and chemical reactions are considered negligible.

In convective heat transfer, both molecular conduction processes and gross fluid movement accomplish the transport of energy to or from a surface. Pure conduction exists at the wall, but away from the wall thermal energy transport takes place by fluid mass motion as well as by conduction. Thus, convection heat transfer process requires knowledge of both heat conduction and fluid flow.

If the fluid motion is induced by some external means such as pump, blower, or fan the process is referred to as forced convection. If the motion of the fluid arises solely due to external force fields such as Coriolis body forces, centrifugal forces, or gravity, acting on density gradients induced by the transport process itself, the process is referred to as natural or free convection.

As in the previous subchapter, concepts of thermal boundary layer, thermal entrance region, and thermally fully developed flow are important. A fundamental assumption of hydrodynamic boundary layer approximations is that the fluid immediately adjacent to the surface is at rest relative to the body. Fluid velocity thus changes from its free stream value to zero at the body surface.

Similar concepts apply to the thermal problem. Thermodynamic equilibrium requires that the fluid adjacent to a surface be at the same temperature as the surface. The region very near the surface, in which the temperature changes from surface temperature to the free stream temperature, is called *thermal boundary layer.*

The *thermal entrance region* of a duct is that region where the thermal boundary layer is developing. In this region, the dimensionless temperature profile of the fluid changes from the initial profile at the point where the heating is started to an invariant form downstream. The flow in this region is referred to as thermally developing flow. The velocity profile in this region could be either developed or developing. Thermally developing flow with a developing velocity profile is referred to as simultaneously developing flow.

The hydrodynamic boundary layer is not necessarily of equal thickness as the thermal boundary layer; similarly, the hydrodynamic entrance length may differ from the thermal entrance length.

The thermal entrance length, L_{th}, is defined as the duct length required to achieve a value of local Nusselt number equal to 105% of the value for fully developed flow, when the entering fluid temperature profile is uniform.

Laminar flow in a two-dimensional stationary duct is designated as thermally fully developed when the dimensionless fluid temperature distribution at a cross-section (equation (3.33.)) is invariant with x; this may be expressed as

$$\frac{\partial}{\partial x}\left(\frac{t_{m,w}-t}{t_{m,w}-t_m}\right)=0 \qquad (3.26.)$$

However, note that, unlike the velocity u for fully developed flow, t is a function of (y, z) as well as x. Hydrodynamically and thermally developed flow is designated throughout simply as fully developed flow.

The solution to the temperature problem involves solving for the fluid and wall temperature distribution and/or heat transfer rate between the wall and the fluid. Several assumptions are commonly made, these being constant fluid properties, flow is steady and laminar, walls are smooth, body forces are negligible and the fluid is forced through the duct by some external means, unrelated to the temperature field in the fluid. Also, the cross-section area of the duct remains constant. Two cases of interest are those of fully developed flow, both hydrodynamically and thermally, and thermally developing flow, with developed or developing velocity profiles.

The energy equation is solved in addition to the fluid flow problem, equations (3.1.) and (3.2.). The form of the energy equation, when the assumptions stated above apply, is

$$u \cdot \frac{\partial t}{\partial x} + v \cdot \frac{\partial t}{\partial y} + w \cdot \frac{\partial t}{\partial z} = \alpha \cdot \left(\frac{\partial^2 t}{\partial x^2} + \frac{\partial^2 t}{\partial y^2} + \frac{\partial^2 t}{\partial z^2} \right) \qquad (3.27.)$$

The effects of thermal energy sources, viscous dissipation and flow work can be included in the energy equation, by adding corresponding terms.

Assuming a uniform temperature distribution at the point where heating/cooling begins, it follows:

$$t = t_e \quad \text{at} \quad x = 0 \qquad (3.28.)$$

Thermal boundary conditions, which describe the temperature and/or heat flux conditions at the inside surface of the duct, may be classified in three groups:

- specified axial wall temperature distribution, t_w (Dirichlet)
- specified axial wall heat flux distribution, q' (Neumann)
- specified combinations of axial wall temperature and heat flux distributions

Around the periphery of the duct, Γ, any combination of t_w and q'' may be specified. These boundary conditions may be applicable to thermally developing and thermally developed flows. Shah and London (1978) present a general classification of thermal boundary conditions and their application.

The mixed mean fluid temperature is defined as the temperature that characterizes the average thermal energy state of the fluid, and it is often referred to as mass-averaged temperature, bulk fluid temperature, or mixing-cup temperature

$$t_m = \frac{1}{A_c \cdot u_m} \cdot \int_{A_c} u \cdot t \cdot dA_c \tag{3.29.}$$

The peripheral mean wall temperature is defined as

$$t_{m,w} = \frac{1}{P} \cdot \int_{\Gamma} t_w \cdot ds \tag{3.30.}$$

The heat flux is related to wall and fluid bulk mean temperatures through the concept of heat transfer coefficient, h. The local heat transfer coefficient is defined as

$$q''_x = h_x \cdot \left(t_{m,w} - t_m\right) \tag{3.31.}$$

The mean (flow length average) heat transfer coefficient is the integrated average of the local value from $x = 0$ to x

$$h_m = \frac{1}{x} \cdot \int_0^x h_x \cdot dx \tag{3.32.}$$

For constant axial wall temperature boundary conditions, the non-dimensional temperature is defined in terms of wall temperature, t_w, and mixed mean temperature, t_m

$$\theta = \frac{t_w - t}{t_w - t_m} \tag{3.33.}$$

whereas for constant axial wall heat flux boundary conditions, the non-dimensional temperature may be defined as:

$$\Theta = \frac{t - t_e}{q'' \cdot D_h / k} \tag{3.34.}$$

The Nusselt number is defined as the ratio of convective conductance h to the pure molecular conductance

$$Nu_x = \frac{h_x}{k / D_h} = \frac{h_x \cdot D_h}{k} = \frac{q''_x \cdot D_h}{k \cdot (t_{m,w} - t_m)} \tag{3.35.}$$

The mean (flow length average) Nusselt number in the thermal entrance region is based on h_m and is expressed as

$$Nu_m = \frac{h_m \cdot D_h}{k} = \frac{1}{x} \cdot \int_0^x Nu_x \cdot dx \tag{3.36.}$$

The Prandtl number is a non-dimensional group representing a fluid property modulus. It is defined as the ratio of kinematic viscosity (diffusivity for momentum, or for velocity) to thermal diffusivity (diffusivity for heat, or for temperature):

$$Pr = \frac{\nu}{\alpha} = \frac{\mu / \rho}{k / \rho \cdot c_p} = \frac{\mu \cdot c_p}{k} \tag{3.37.}$$

The Peclet number represents the relative magnitude of the thermal energy convected to the fluid to the thermal energy axially conducted within the fluid. The effect of axial conduction is small for $Pe > 10$, and completely negligible for $Pe > 100$.

$$Pe = \frac{\rho \cdot c_p \cdot u_m \cdot D_h}{k} = \frac{u_m \cdot D_h}{\alpha} \quad \Rightarrow \quad Pe = Re \cdot Pr \tag{3.38.}$$

Two simple general boundary conditions are the constant heat rate per unit tube length, and constant surface temperature. These boundary conditions are shown by Sparrow and Patankar (1977) to be special cases of a more general exponential heat flux boundary condition.

For the case of constant heat rate per unit tube length, considering constant heat transfer coefficient h, it follows that $q''_w = h \cdot (t_w - t_m) = \text{constant}$, and then $(t_w - t_m)$ is constant. Thus, for fully developed conditions

$$\frac{\partial t}{\partial x} = \frac{dt_w}{dx} = \frac{dt_m}{dx} \tag{3.39.}$$

The case for constant surface temperature can be expressed mathematically as $dt_w/dx = 0$, and it follows that

$$\frac{\partial t}{\partial x} = \frac{t_w - t}{t_w - t_m} \cdot \frac{dt_m}{dx} \tag{3.40.}$$

The corresponding temperature variations with tube length for these two conditions are shown in Figure 3.3.

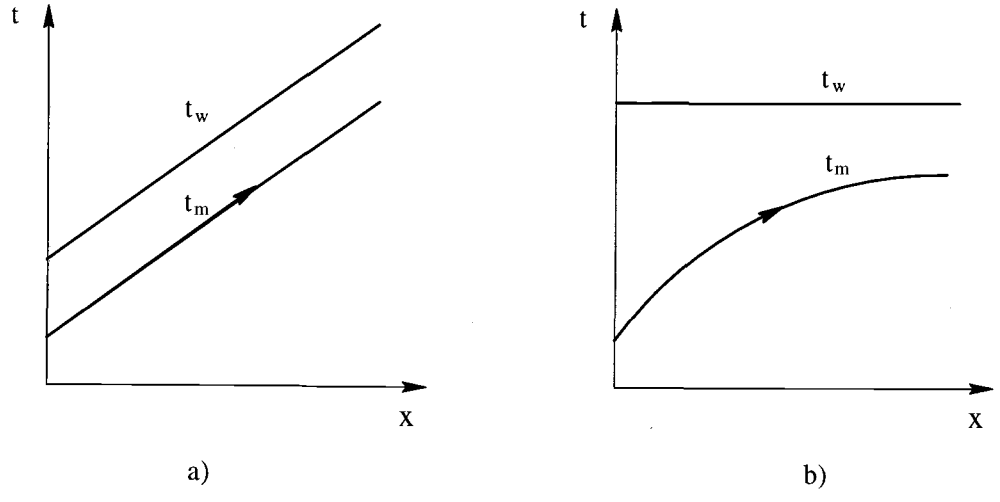

Figure 3.3. Temperature variations for a) constant heat rate per unit tube length, and b) constant surface temperature

3.2.1 Circular cross section pipes

For the constant heat rate problem, the solution of the energy equation with applicable boundary conditions for heat transfer in round pipes involves the parabolic velocity profile and determines the temperature profile, *t*. Next the mean mixed temperature can be evaluated. In order to determine the conductance *h*, the surface heat flux can be evaluated from a simple energy balance on a differential control volume. Therefore, from equation (3.31.) it follows

$$q''_w = h\cdot(t_w - t_m) \quad \Rightarrow \quad \frac{r_0\cdot u_m\cdot\rho\cdot c_p}{2}\cdot\frac{dt_m}{dx} = h\cdot\frac{11}{96}\cdot\frac{2\cdot u_m}{\alpha}\cdot\frac{dt_m}{dx}\cdot r_0^2 \quad \Rightarrow$$

$$h = \frac{48}{11}\cdot\frac{k}{D} = 4.364\cdot\frac{k}{D} \tag{3.41.}$$

and, in non-dimensional form

$$\frac{h\cdot D}{k} = Nu = 4.364 \tag{3.42.}$$

This is only true for laminar flow and for special case of fully developed velocity and temperature profiles. This independence results from the fact that energy transport is a purely molecular conduction problem under these conditions.

For the constant surface temperature problem, for fully developed flow and temperature, the parabolic velocity profile is substituted in the energy equation as before, but in this case, the solution is in the form of an infinite series:

$$\frac{t_w - t}{t_w - t_m} = \sum_{n=0}^{\infty} C_{2n}\cdot\left(\frac{r}{r_0}\right)^{2n} \tag{3.43.}$$

and the corresponding Nusselt number can be shown to be

$$Nu = 3.657 \tag{3.44.}$$

3.2.2 Rectangular cross section ducts

As well as in fluid flow problem, analysis of heat transfer in rectangular ducts requires a more complex two-dimensional analysis. The achievement of an analytic solution is fairly complicated and, ultimately, a computer must be used.

For constant heat rate boundary condition, the solution can be found by analogy, as in fluid flow, with the solution for the small deflection of a thin plate under a uniform lateral load, with the plate simply supported along all edges (Marco and Han, 1955). The Nusselt number Nu_H can be expressed as

$$Nu_H = \frac{64}{\left(1+\alpha^*\right)^2 \cdot \pi^2} \cdot \frac{\left[\sum_{m=1,3,\ldots}^{\infty} \sum_{n=1,3,\ldots}^{\infty} \frac{1}{m^2 \cdot n^2 \cdot \left(m^2 + n^2 \cdot \left(\alpha^*\right)^2\right)}\right]^2}{\left[\sum_{m=1,3,\ldots}^{\infty} \sum_{n=1,3,\ldots}^{\infty} \frac{1}{m^2 \cdot n^2 \cdot \left(m^2 + n^2 \cdot \left(\alpha^*\right)^2\right)^3}\right]} \qquad (3.45.)$$

Shah and London (1978) determined a six-digit-accurate formula by taking into account first 250 terms of each series, the expression being

$$Nu_H = 8.235 \cdot \left[1 - 2.0421 \cdot \alpha^* + 3.0853 \cdot \left(\alpha^*\right)^2 - 2.4765 \cdot \left(\alpha^*\right)^3 + 1.0578 \cdot \left(\alpha^*\right)^4 - 0.1861 \cdot \left(\alpha^*\right)^5\right] \qquad (3.46.)$$

This formula provides results accurate within 0.03 percent. The authors redefined the Nusselt number with the hydraulic diameter based on wetted perimeter instead of heated perimeter, as presented in earlier work. They reported the new values of Nusselt number for specified heat rates on one, or more than one, walls heated. Hartnett and Kostic (1989) presented the same data with another codification of the combinations of heated and adiabatic walls (Figure 3.4.).

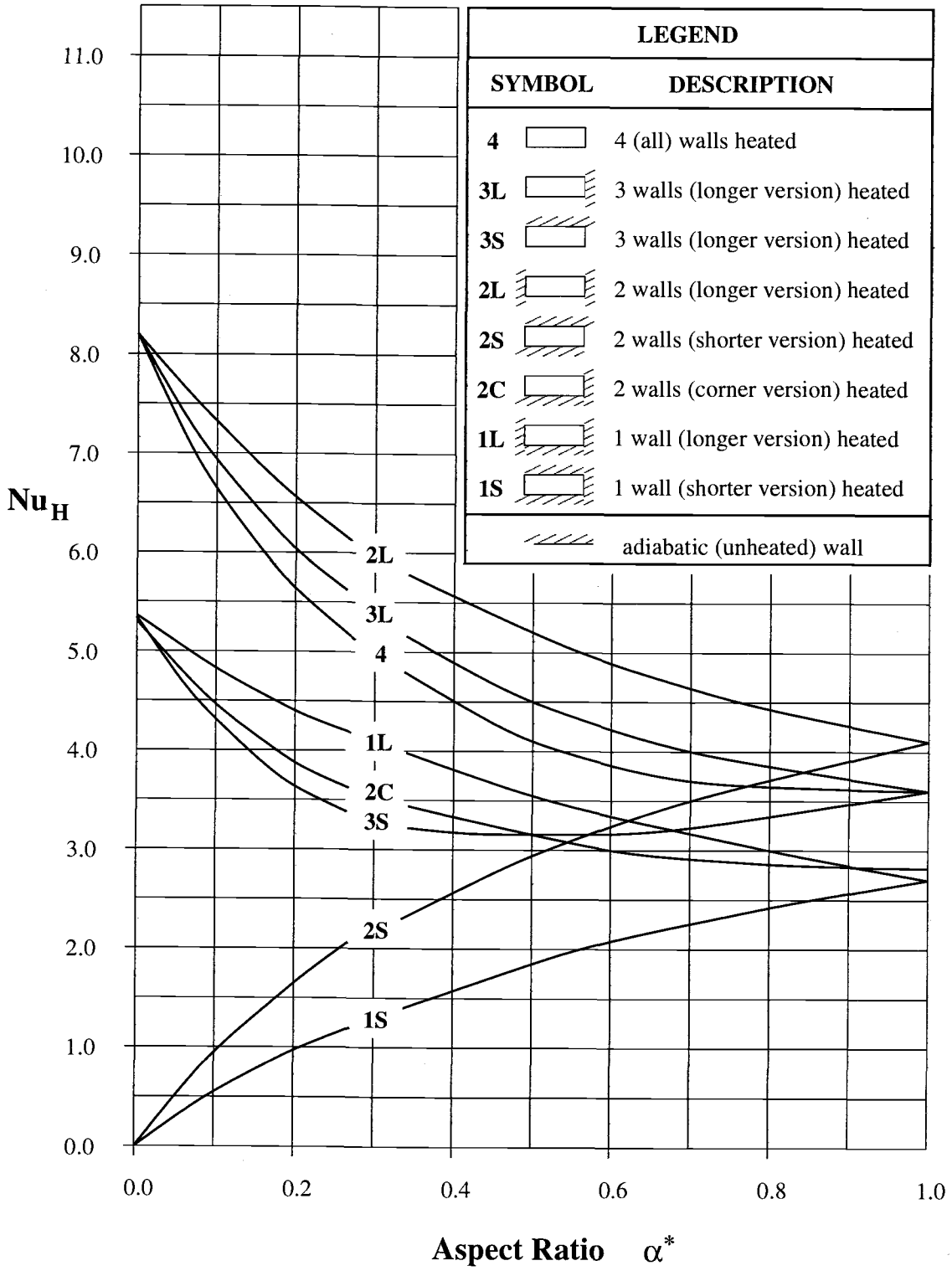

Figure 3.4. Fully established laminar Nusselt number values for specified constant heat rate boundary condition as a function of the aspect ratio for different combinations of heated and adiabatic walls (Hartnett and Kostic, 1989).

Of particular interest for the present work, is the case of infinite parallel plates heated on one side. Infinite parallel plates represent the limiting case of ducts with rectangular cross-sections, for very small values of the aspect ratio ($\alpha^* < 0.1$). The Nusselt number for fully developed velocity and temperature profiles for this case is

$$Nu = 5.385 \tag{3.47.}$$

Clark and Kays (1953) numerically evaluated fully developed Nusselt numbers in the case of specified wall temperature, for flow in rectangular ducts of various aspect ratios. Subsequently, several other investigators have refined this treatment and Shah and London (1978) and Hartnett and Kostic (1989) present generalized results in both tabular and graphical form. It is noted that the results for non-symmetric heating are not as accurate as those for symmetric heating. For this kind of boundary conditions,

$$Nu_H = 7.541 \cdot \left[1 - 2.610 \cdot \alpha^* + 4.970 \cdot (\alpha^*)^2 - 5.119 \cdot (\alpha^*)^3 + 2.702 \cdot (\alpha^*)^4 - 0.548 \cdot (\alpha^*)^5\right] \tag{3.48.}$$

This expression gives the Nusselt number as a function of aspect ratio alone. Values are accurate within 0.1 percent.

3.2.3 Thermal entry length problem

For the thermal entrance region, the dimensionless distance in the flow direction is specified as

$$x_{th}^+ = \frac{x}{D_h \cdot Pe} = \frac{x}{D_h \cdot Re \cdot Pr} \tag{3.49.}$$

The dimensionless thermal entrance length is expressed as

$$L_{th}^+ = \frac{L_{th}}{D_h \cdot Pe} = \frac{L_{th}}{D_h \cdot Re \cdot Pr} \tag{3.50.}$$

For the exact solution to the thermal entry length problem, the continuity and momentum equations must first be solved to determine u, v, and w. Thermal entry length problems are of three categories:

- the velocity profile is fully developed and remains fixed while the temperature profile develops
- the velocity and temperature profile are developing simultaneously
- the temperature profile starts developing at some point in the hydrodynamic entry region

The relative rate of development of velocity and temperature profiles in the entrance region depends upon the fluid Prandtl number (equation (3.37.)). For $Pr = 1$, the velocity and temperature profiles developing at the same rate if both are uniform at the entrance. For $Pr > 1$ the velocity profile develops more rapidly than temperature profile. For $Pr > 5$, the velocity profile leads the temperature profile sufficiently that a solution based on an already fully-developed velocity profile will apply accurately, even though no hydrodynamic starting length is considered. For $Pr < 1$, the situation is reversed; the temperature profile develops more rapidly than velocity profile. The case of a fully developed velocity profile before the temperature profile starts to develop represents the limiting case of $Pr = \infty$, which is a good approximation for highly viscous fluids. For the other limiting case, $Pr = 0$, the velocity profile never develops (remains uniform) while the temperature profile is developing. This idealized case approximates the behavior of liquid metals.

The thermal entry length problem with simultaneously developing velocity and temperature profiles is also referred to as the combined-entry-length problem. The thermal entry length problem of the first category above, which is valid for any fluid, is identical to the combined entry length problem for $Pr = \infty$. Thus the combined entry length solution for $Pr = \infty$ is also a solution for fluids of any Prandtl number, with a developed velocity profile and developing temperature profile. In a similar manner, the combined entry length solution for $Pr = 0$ also refers to the solution of any fluid with uniform velocity profile (slug flow) and developing temperature profile.

Solution to the problem for round pipes is given by Kays and Crawford (1993) using the normalized form of the energy equation. The form of Nu_m is

$$Nu_m = \frac{1}{2 \cdot x^+} \cdot \ln \frac{1}{\theta_m} \tag{3.51.}$$

where the non-dimensional mixed mean temperature is expressed as

$$\theta_m(x^+) = \frac{t_w - t_m}{t_w - t_e} \tag{3.52.}$$

The energy equation is linear and homogeneous and can be solved by the method of separation of variables, the solution of this Sturm-Liouville type problem being

$$\theta_m = 8 \cdot \sum_{n=0}^{\infty} \frac{G_n}{\lambda_n^2} \cdot \exp\left(-\lambda_n^2 \cdot x^+\right) \tag{3.53.}$$

The local and mean Nusselt numbers are then readily evaluated as

$$Nu_x = \frac{\sum_{n=0}^{\infty} G_n \cdot \exp\left(-\lambda_n^2 \cdot x^+\right)}{2 \cdot \sum_{n=0}^{\infty} \frac{G_n}{\lambda_n^2} \cdot \exp\left(-\lambda_n^2 \cdot x^+\right)} \tag{3.54.}$$

$$Nu_m = \frac{1}{2 \cdot x^+} \cdot \ln \left[\frac{1}{8 \cdot \sum_{n=0}^{\infty} \frac{G_n}{\lambda_n^2} \cdot \exp\left(-\lambda_n^2 \cdot x^+\right)} \right] \tag{3.55.}$$

The eigenvalues λ_n and the constants G_n for these infinite series are given in tabular form. For large x^+ the series become increasingly more convergent, until finally, for $x^+ > 0.1$, only the first term is of significance. Thus, the thermal entry length is determined to be approximately $x^+ = 0.1$.

The boundary conditions are such that the temperature gradient at the wall is infinite at $x^+ = 0$, and therefore, $Nu_x = \infty$. At points far down the tube, the value of Nusselt number will approach the value for the fully developed condition discussed above. A graphic representation of the solution is presented in Figure 3.5.

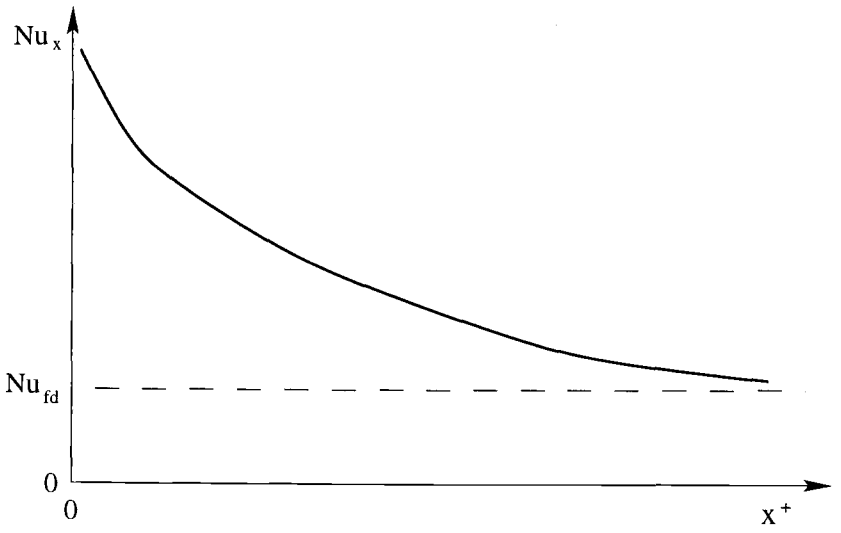

Figure 3.5. Variation of local Nusselt number in the thermal entry region of a tube

The uniform heat flux, thermal entry length problem has been solved in a similar manner, the new boundary condition being one with a constant temperature gradient at the surface. The non-dimensional temperature is expressed by equation (3.34.). The solution for the local Nusselt number, is:

$$Nu_x = \left[\frac{1}{Nu_\infty} - \frac{1}{2} \cdot \sum_{m=1}^{\infty} \frac{\exp\left(-\gamma_m^2 \cdot x^+\right)}{F_m \cdot \gamma_m^4} \right]^{-1} \qquad (3.56.)$$

In a constant heat flux problem the mixed mean temperature of the fluid varies linearly with x^+. For the thermal entrance length, the mean fluid and the wall surface temperatures, plotted as functions of distance along the tube, appear as in Figure 3.6.

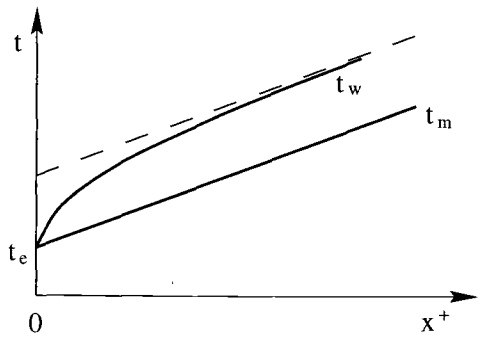

Figure 3.6. Temperature variations in the thermal entry region of a tube with constant heat rate per unit of tube length

For the case of rectangular cross section ducts, the non-dimensional axial distance is expressed as

$$x_{th}^{+} = \frac{2 \cdot (x/D_h)}{Re \cdot Pr} \tag{3.57.}$$

Thermal entry length solutions for the entire family of rectangular ducts with constant heat rate boundary condition have been computed numerically and are presented in Table 3.2. (Kays and Crawford, 1993) and Table 3.3. (Shah and London, 1978).

Table 3.2. Nusselt numbers for the rectangular ducts with constant heat rate axially, thermal entry length solution (Kays and Crawford, 1993)

x^+	Nu_x				
	$1/\alpha^* = 2a/2b$				
	1	2	3	4	∞
0	∞	∞	∞	∞	∞
0.01	7.10	7.46	8.02	8.44	
0.02	5.69	6.05	6.57	7.00	8.80
0.05	4.45	4.84	5.39	5.87	
0.10	3.91	4.38	5.00	5.62	8.25
0.20	3.71	4.22	4.85	5.45	
∞	3.60	4.11	4.77	5.35	8.235

Table 3.3. Axial and mean Nusselt numbers for thermal entry length, fully developed velocity profile, constant heat rate (Shah and London, 1978)

$\frac{1}{x^+}$	Nu_x				Nu_m			
	Aspect Ratio, α^*				Aspect Ratio, α^*			
	1.0	0.5	1/3	0.25	1.0	0.5	1/3	0.25
0	3.60	4.11	4.77	5.35	3.60	4.11	4.77	5.35
10	3.71	4.22	4.85	5.45	4.48	4.94	5.45	6.03
20	3.91	4.38	5.00	5.62	5.19	5.60	6.06	6.57
30	4.18	4.61	5.17	5.77	5.76	6.16	6.60	7.07
40	4.45	4.84	5.39	5.87	6.24	6.64	7.09	7.51
60	4.91	5.28	5.82	6.26	7.02	7.45	7.85	8.25
80	5.33	5.70	6.21	6.63	7.66	8.10	8.48	8.87
100	5.69	6.05	6.57	7.00	8.22	8.66	9.02	9.39
120	6.02	6.37	6.92	7.32	8.69	9.13	9.52	9.83
140	6.32	6.68	7.22	7.63	9.09	9.57	9.93	10.24
160	6.60	6.96	7.50	7.92	9.50	9.96	10.31	10.61
180	6.86	7.23	7.76	8.18	9.85	10.31	10.67	10.92
200	7.10	7.46	8.02	8.44	10.18	10.64	10.97	11.23

There is a discrepancy between the data presented in the two works cited. The data from Shah and London (1978) and Hartnett and Kostic, (1989), following the same original work of Wibulswas, are represented graphically in Figure 3.7.

The thermal entrance length is the duct length required for the local Nusselt number to come within 5 percent of the fully developed value. For thermally developing flow, the data for constant surface temperature and constant heat rate boundary conditions are presented graphically in Figure 3.8. as functions of the aspect ratio, α^*. The thermal entrance length for a constant-heat-rate boundary condition is well behaved, varying monotonically from a value of approximately 0.01 for plane parallel plates to a value of about 0.066 for a square duct.

In the case of constant wall surface temperature boundary condition, there is some uncertainty associated with the values presented in the literature. A value of $L_{th}^+ > 0.055$ is suggested (Kays and Crawford, 1993) for engineering calculation of rectangular ducts of aspect ratios larger than 0.2.

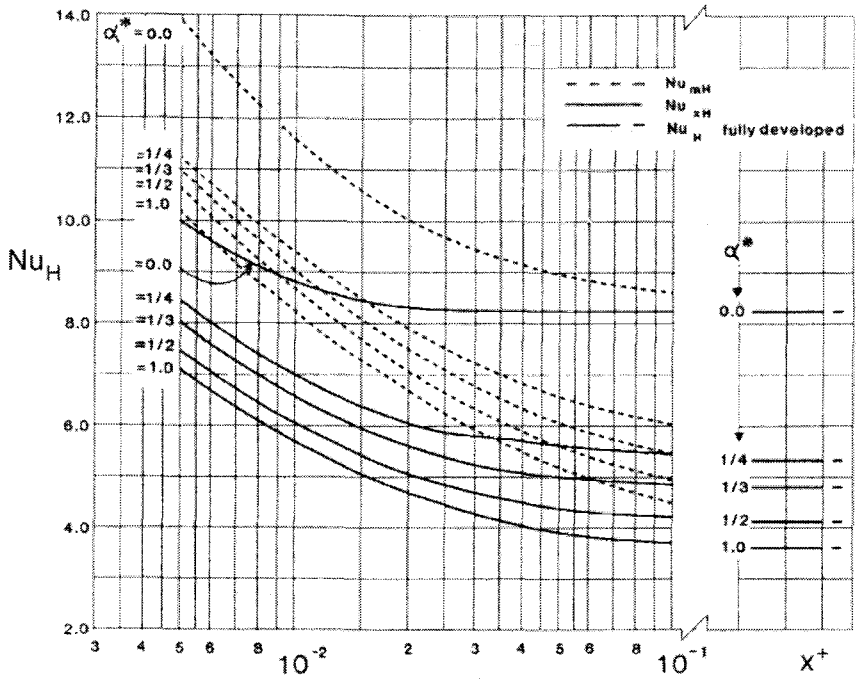

Figure 3.7. Thermally developing Nusselt number as a function of non-dimensional axial distance and the aspect ratio for the constant heat rate boundary condition (Hartnett and Kostic, 1989)

In the case of simultaneously developing velocity and temperature profiles, the departure from the thermally developing Nusselt number at a given axial position depends on the Prandtl number.

Shah and London (1978) presented results of the simultaneous developing case for both the constant heat rate and constant wall surface temperature cases. Values are represented as functions of non-dimensional axial distance and aspect ratio, for Pr = 0.72. Data presented in Table 3.4. neglect the effects of axial momentum and thermal diffusion. It is specified that the transverse velocity components v and w are zero. The authors presented a comparison of mean Nusselt number variation as a function of Prandtl number, from $Pr = 0$ (slug flow) to $Pr = \infty$ (developed flow), as well as the results from other researchers for a rectangular duct with an aspect ratio of 0.5.

Table 3.4. Axial and mean Nusselt numbers for thermal entry length, simultaneously developing flow, constant heat rate (Shah and London, 1978)

$\frac{1}{x^+}$	Nu_x				Nu_m			
	Aspect Ratio, α^*				Aspect Ratio, α^*			
	1.0	0.5	1/3	0.25	1.0	0.5	1/3	0.25
5	-	-	-	-	4.60	5.00	5.57	6.06
10	4.18	4.60	5.18	5.66	5.43	5.77	6.27	6.65
20	4.66	5.01	5.50	5.92	6.60	6.94	7.31	7.58
30	5.07	5.40	5.82	6.17	7.52	7.83	8.13	8.37
40	5.47	5.75	6.13	6.43	8.25	8.54	8.85	9.07
50	5.83	6.09	6.44	6.70	8.90	9.17	9.48	9.70
60	6.14	6.42	6.74	7.00	9.49	9.77	10.07	10.32
80	6.80	7.02	7.32	7.55	10.53	10.83	11.13	11.35
100	7.38	7.59	7.86	8.08	11.43	11.70	12.00	12.23
120	7.90	8.11	8.37	8.58	12.19	12.48	12.78	13.03
140	8.38	8.61	8.84	9.05	12.87	13.15	13.47	13.73
160	8.84	9.05	9.38	9.59	13.50	13.79	14.10	14.48
180	9.28	9.47	9.70	9.87	14.05	14.35	14.70	14.95
200	9.69	9.88	10.06	10.24	14.55	14.88	15.21	15.49
220	-	-	-	-	15.03	15.36	15.83	16.02

Table 3.5. Thermal entrance length, simultaneously developing flow, constant heat rate, for Pr = 0.7 (Shah and London, 1978)

Rectangular Duct, α^*	$L^+_{th\,H}$
0	0.017
1/8	0.079
1/4	0.136
1/3	0.170
1/2	0.230
1	0.340
Circular pipe	0.053

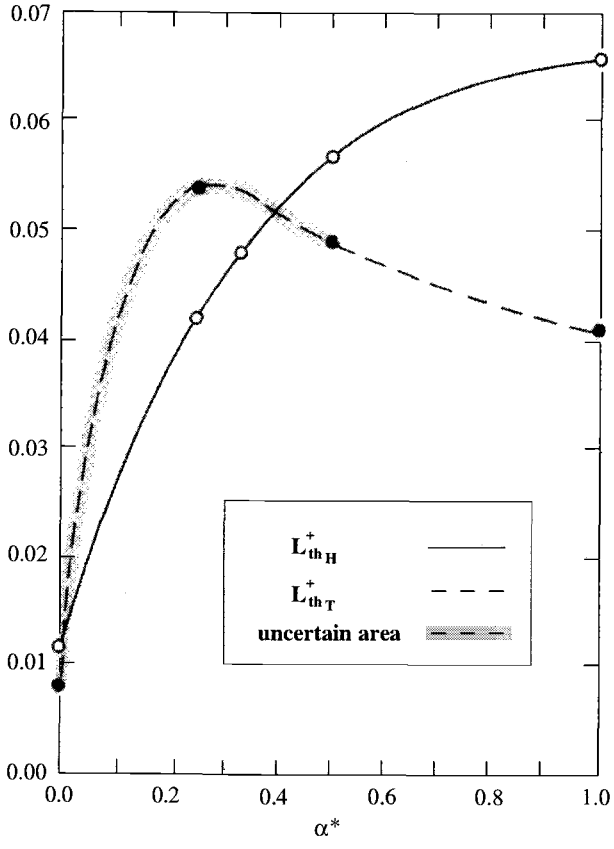

Figure 3.8. Thermal entrance length for thermally developing flow

The thermal entrance length for simultaneously developing flow decreases monotonically with the aspect ratio (Table 3.5). It is interesting to note that the thermal entrance length for rectangular ducts with $\alpha^* > 0$ are significantly higher than those for parallel plates, and the value for a square duct is one order of magnitude larger than that for a circular tube.

4. EXPERIMENTAL DEVICE AND MEASUREMENTS

The purpose of this effort is to examine the hydrodynamic and heat transfer behavior associated with fluid flow in microchannels of rectangular cross-section.

The test loop was designed in a modular manner, capable of accommodating various set-ups depending on the specific requirements of the intended experimental research. The test section was fabricated in a sandwich structure that formed a single rectangular micro-channel. While the width of the channel remained constant, the depth is variable, allowing measurements to be taken in a progressive manner, from macroscale to microscale.

4.1. Experimental device

The physical layout of the experimental device, including details of the components and instrumentation, is described in this section. The same test section was used for both fluid flow and heat transfer measurements.

4.1.1 Set-up for fluid flow measurements

The loop configuration for the pressure drop and friction factor measurements is shown in detail in Figure 4.1. The test section was installed in a high-turndown, low noise, water flow system. The once-through system is driven by water main pressure, thus did not require a pump.

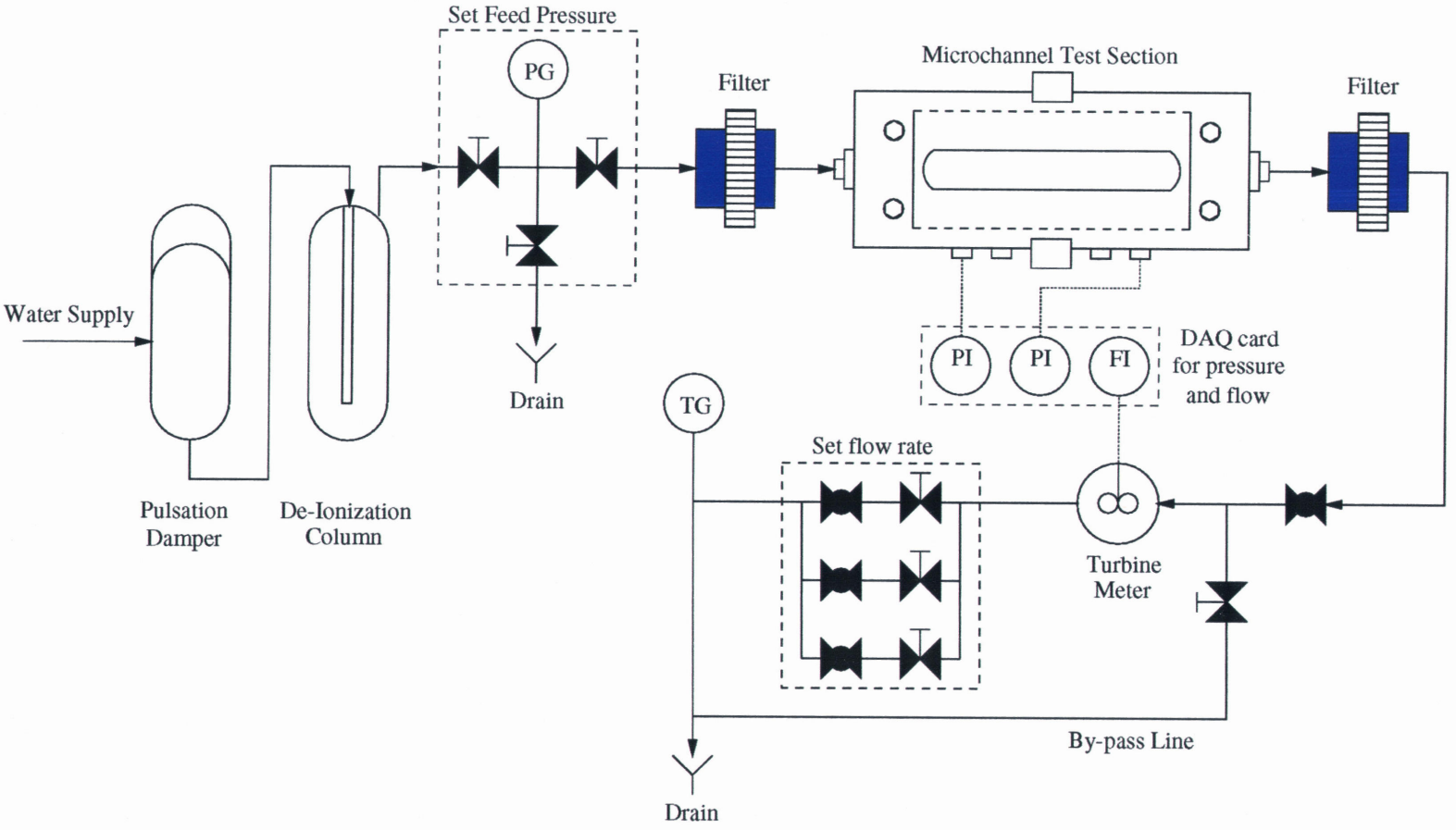

Figure 4.1. Test loop configuration for fluid flow measurements

Water enters the system through a pressurized pulsation damper, having a volume of approximately 19 liters and an air-reservoir pressure of 2-bar gauge. From there, it flows through a de-ionization column and then through a set of manual valves, used to control the pressure of the experiment at the downstream pressure sensor in the test section, by varying a bleed flow to a drain.

Before entering the test section, the water flows through a filter with a nominal pore size of 1.6 microns (Glass Microfibre Filters, supplied by Whatman, Inc.). When exiting the test section, water flows through another similar filter.

The next section of the flow loop consists of a manifold of three needle metering valves (Nupro SS-SS4-EP-VH and Nupro SS-4MG-EP-MH), used to control the flow rate between 15 and 1000 ml/min. Water flow into the control section is controlled with ball valves. Flow rates are measured with miniature turbine meters with high turndown, McMillan models 102-3P (15 – 100 ml/min) and 102-6P (100 – 1000 ml/min).

The test section was designed to yield both high precision measurements and to allow flow visualization. It is composed of four plates, clamped together in a sandwich structure, which is shown assembled and disassembled in Figure 4.2.

A single microchannel is formed by a polycarbonate spacer/gasket (3) sandwiched between a clear, 3.2 mm thick, polycarbonate Lexan® top plate (2) and a 1.2 mm thick, polyimide Cirlex® bottom plate (4). The fluid within the channel can be viewed through the clear top. The thickness of the spacer, which defines the depth of the channel, can be varied to allow progression from microchannel to near macrochannel flow. The width of the channel cut into spacer, fixed at 10 mm, produces approximately 2-D flow, thereby simplifying comparisons with the theoretical description of the flow. The sandwich rested on a 12.7-mm thick, polycarbonate support plate (5). The whole assemble was held together between stainless steel top (1) and bottom (6) pressure plates by screws and a clamping mechanism (7).

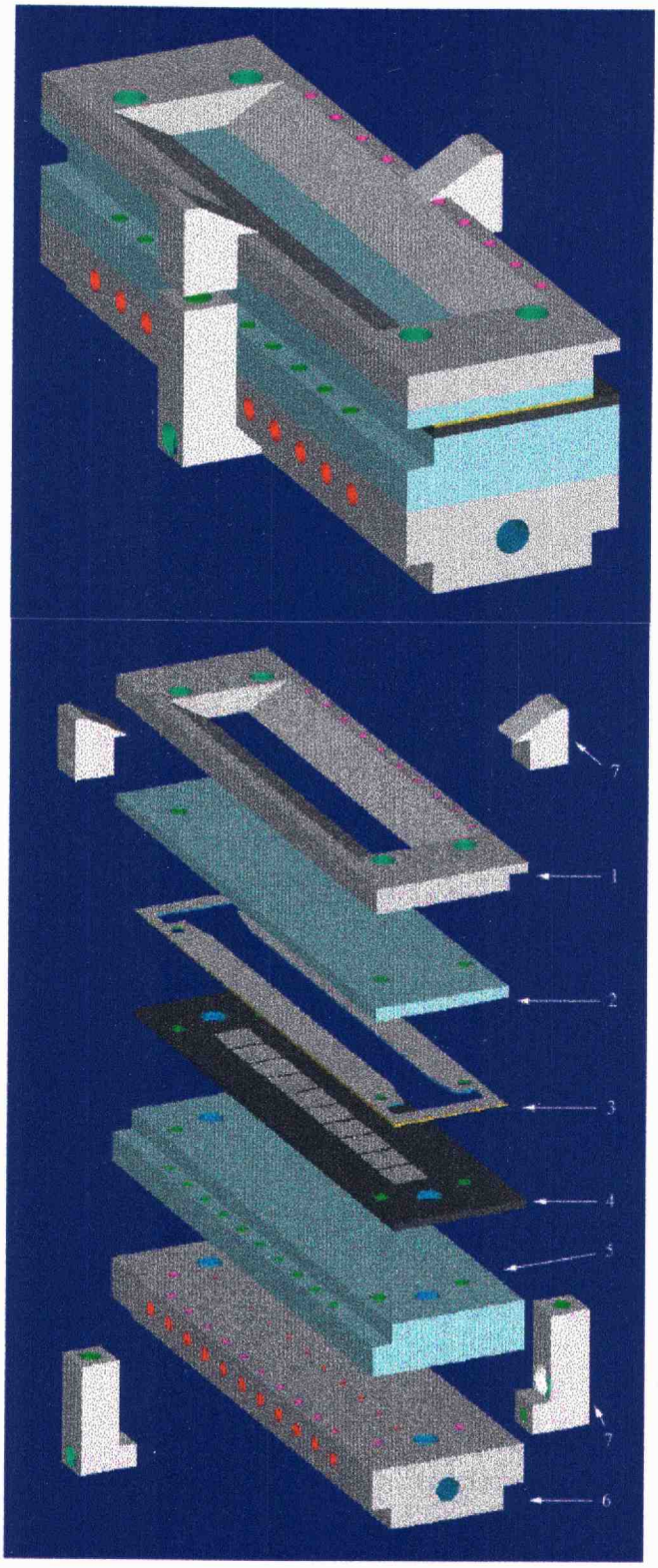

Figure 4.2. Test section (top - assembled; bottom - disassembled)

The polycarbonate support plate and the bottom pressure plate include passageways for fluid in- and outflow, and for pressure taps. A series of eleven pressure ports (spaced at 10.16 mm intervals) are located in the bottom stainless steel pressure plate that forms the bottom of the clamping mechanism. These ports are connected to the channel through the holes drilled in the 12.7 mm thick polycarbonate support plate and polyimide channel base. The pressure taps drilled in the polyimide bottom plate at an offset from the channel centerline are of 0.5 mm in diameter.

The bodies of the transducers are threaded into the ports in the bottom stainless steel plate. The ENDEVCO models 8510C-100 and 8510C-50 are rugged miniature, high sensitivity piezoresistive pressure transducers. They feature four-arm strain gage bridges, self-contained hybrid temperature compensation, excellent linearity, high shock resistance and high stability during temperature transients. Both sensors were calibrated with compressed air using a temperature compensated Heise gauge.

The data acquisition system (DAQ) is build with components supplied by Strawberry Tree™ Inc. and specially designed connectors. The WorkBench™ software associated with the system is using LabVIEW-like icons and wiring for easy programming. It has limited possibilities, but covers the requirements of the present research. The Analog Connection PC (ACPC) simplifies data acquisition and control. Designed for laboratory and industrial use such as data logging, process monitoring, and process controlling, it measures temperature, pressure, flow and other analog/digital inputs from sensors and instruments. Each card has two terminal panels.

A particular emphasis of the experimental research is the augmentation of the traditional measurements with qualitative observation of the flow regimes within the channel. The flow visualization used multiple-pulsed particle-image-velocimetry (PIV). The clear top surface of the channel allows the fluid to be viewed under a microscope (Zeiss – Axioskop). A syringe pump injected a dye into the microchannel through a pressure tap hole. The dye streams are observed to determine if the flow is laminar or turbulent. The interior of the channel is illuminated with a laser beam. The images are captured with a camera placed on the top of the microscope and recorded on a videodisk.

4.1.2 Set-up for heat transfer measurements

The working fluid for heat transfer measurements is restricted to refrigerant HCFC-124 (known as R-124) operating in a low-pressure range, 0 – 100 psi. Although environmentally friendly, the R-124 fluid has to be contained in a closed loop. A schematic of the set-up for heat transfer measurements is presented in Figure 4.3.

The test section is installed in a high-turndown, low noise system that is driven by pressure difference between two reservoirs. The "hot" reservoir is maintained at high temperature, high-pressure using external heaters, and controls the pressure in the system. The "cold" reservoir is cooled using an ice bath, which maintains low pressure and low temperature in the cylinder.

Two tube-in-shell heat exchangers are used to control the temperature of the fluid flowing through the loop. The high-pressure, high temperature refrigerant from the hot reservoir flows through the glass microfiber filter before entering the first heat exchanger. A JULABO heating/cooling device regulates the temperature of the fluid in the shell of the first heat exchanger, thus controlling the temperature of the working fluid. When exiting the test section, the temperature of the refrigerant is high, and therefore, after passing through the second glass microfiber filter, enters in the second heat exchanger to lower its temperature.

The data acquisition system is used to record values of flow rate, temperature at the flow meter, pressure at the mid-point of the test section, temperatures at the bottom and top surface of the test channel, and voltage/power supplied to the heaters.

The system required 40 channels to record data from 26 resistance temperature detectors (RTD), 10 heaters, 2 pressure transducers, and 2 flow measurements. In the test channel there are 24 RTDs (11 on the bottom and 13 on the top), while the other 2 are at flow meters, to determine temperature variation (density compensation).

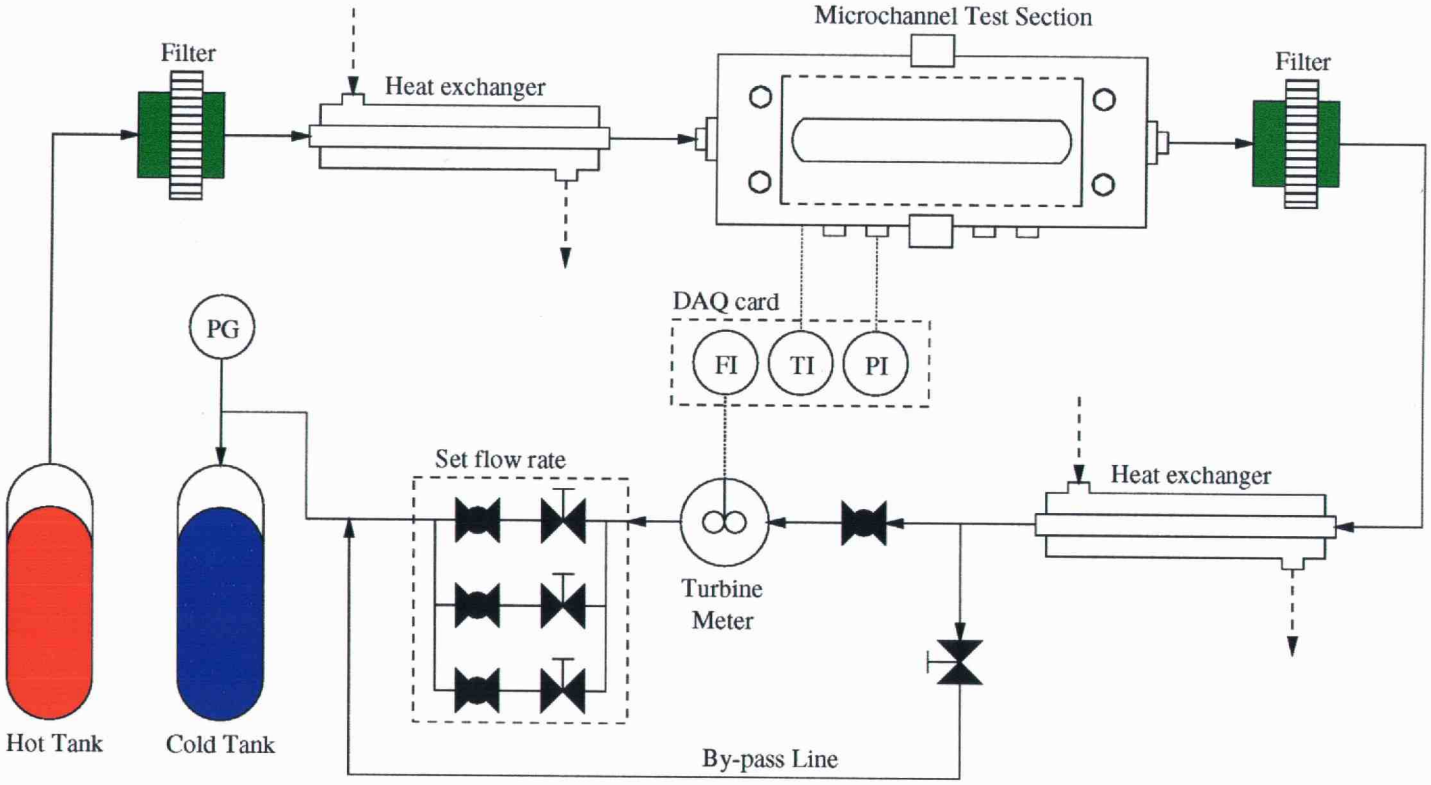

Figure 4.3. Test loop configuration for heat transfer measurements

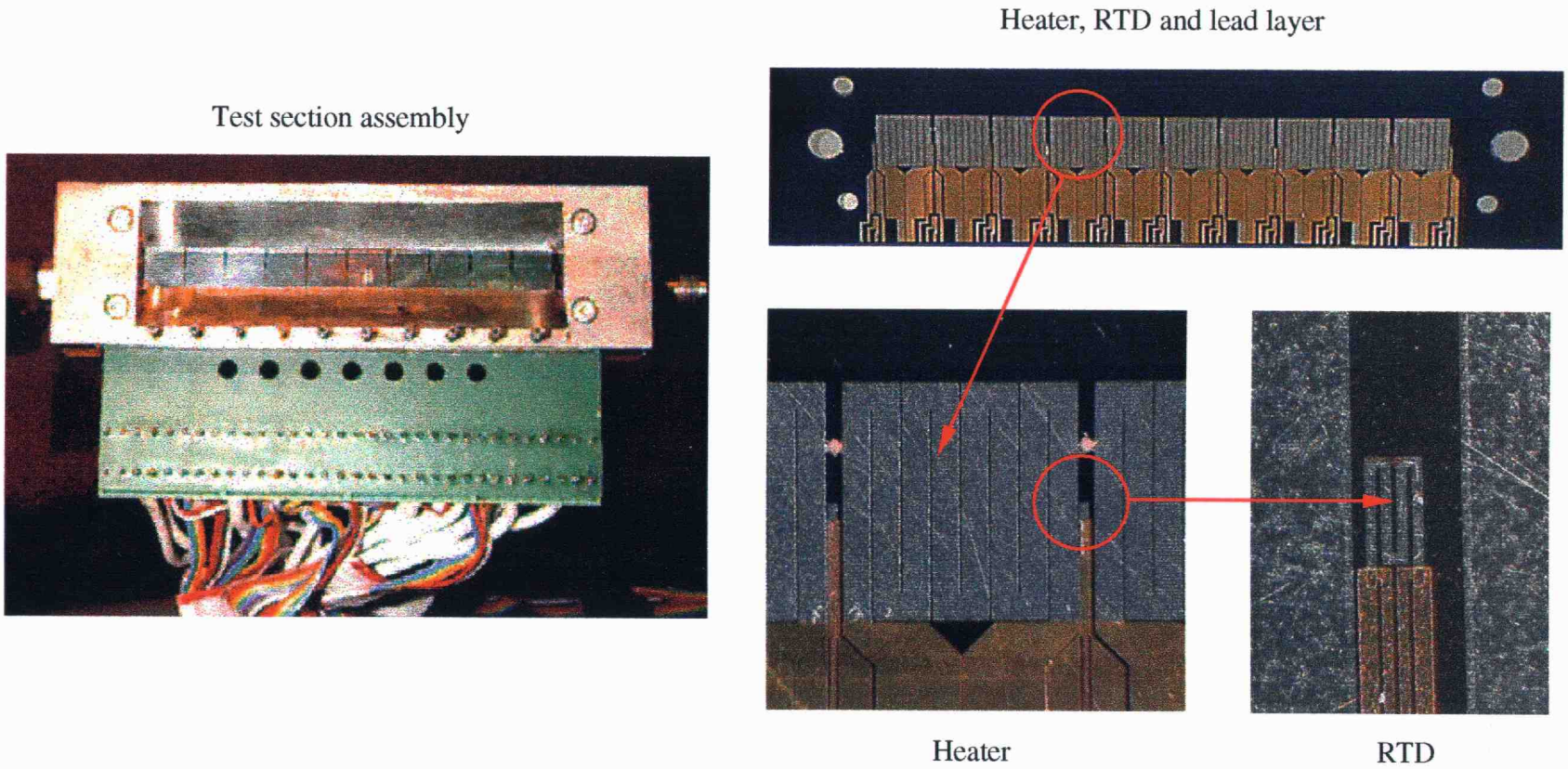

Figure 4.4. Test section assembly and details of the heater plate

The heater plate (item 4 in Figure 4.2) that forms the bottom of the channel is a non-conductive polyimide, thermally treated to resist high temperatures. Several thin films were deposited to form the RTDs, heaters and leads (Figure 4.4).

The heater plate was designed such that it can provide boundary conditions of both a uniform surface temperature and a uniform heat flux.

A series of ten heaters were deposited on the polyimide substrate, each being controlled individually from the heater control panel. The heater shape is that of a thin-film platinum serpentine with 8 passes, 0.867 cm^2 of active surface, connected through gold leads to the gold tabs at the edge of the plate. The pressure taps as well as the low power (1μW) resistance temperature detectors (RTDs) are placed in the 0.71-mm gaps between the heaters, before the first heater, and after the last heater. The active tip of each RTD is deposited on the centerline of the channel, and consists of a 4-pass platinum serpentine, approximately 350 μm wide and 675 μm long. The gold leads that connect the active element and the tabs at the edge of the plate are set in a four-wire configuration (two for signal, two for power) to eliminate errors caused by the resistance of the lead wires. Dimensional details of heater plate geometry are specified in appendices.

A specially designed printed circuit board (PCB) in contact with the lead ends on the edge of the heater plate makes the connection with the data acquisition system.

The wiring from PCB is connected to the terminal panels, and through cables to the analog card inside the computer. The heater terminals are connected to the heater control panel that provides manual heater controls. This procedure is less precise, but the decrease in precision does not affect, on large scale, the measurements. Heaters are controlled individually, each circuit including a Variac, isolation transformer, rectifier and capacitor filter.

4.2. Experimental measurements

All instrumentation used in this work was calibrated against local standards. An end-to-end calibration was performed for all instruments, that is from the sensor to the data acquisition board. Details regarding calibration and uncertainty analyses are provided in the appendices.

The software was programmed to read, analyze and log the data from the analog inputs. For each channel, several types of icons were used:

- **analog input** icons, to read the analog signal from the transducers
- **calculation icons**, to zero the initial signal value, to average the signal, transform the reading from voltage to proper measuring units
- **meter icons**, to monitor values of the required parameters

For some channels, where limiting values were mandatory, alarms were set using **alarm** icons, with both audio and video signals. A **log** icon was used to record all required information in a file that was later analyzed using data processing software.

4.2.1 Channel depth measurements

The sandwich construction of the test section allows the study of a variety of channel depths by changing the thickness of the spacer. The geometry of the spacer remains unchanged, except for the thickness. For pressure and heat transfer measurements, microchannels with mean depths of 521 μm, 263 μm, and 128 μm were assembled with a smooth polyimide bottom plate. For comparison with macroscale behavior in the same channel, a control spacer with mean depth of 1,050 μm was also used. For pressure measurements only, a rough polyamide bottom plate was used in a channel with mean depth of 257 microns.

Efforts were made to accurately measure channel depths *in situ*. Mean channel depths were measured with the test section mounted on a vertically translating stage with a micrometer adjustment and the assembly placed under a microscope. Measurements were made using a 10X objective lens, with numerical aperture (NA) of 0.25 and a photographic depth of field of approximately 8.5 μm. The microscope's optics were aligned and the illumination apertures were stopped down to allow the sharpest focus. The microscope was focused on the top and bottom surfaces of the microchannel, and channel depths were determined from the differences in micrometer readings. Final focusing was made on a video image captured with a camera mounted on the microscope. For all cases except the 128 microns-deep channel, the microchannel was pressured with water at approximately 2 bar gauge pressure. Measured micrometer readings were then multiplied by the refractive index of water to arrive at the depth of the channel. Measurements were made at 9 points along the channel centerline and 9 more approximately 2 mm away from the wall. Mean channel depths and uncertainties in the mean are presented in the appendices.

4.2.2 Surface roughness measurements

The sandwich construction of the test section and the relative ease of assembly and disassembly allow the channel walls to be replaced by new walls roughened to a specified degree. Surface profilometry was performed on disassembled parts.

Surface roughness on the top polycarbonate and the bottom polyimide plates were measured with a white light interferometer (Zigo New View 200 Optical Profilometer). The instrument allowed non-contact profilometry with 5Å vertical resolution and 1.1 μm lateral resolution. In addition to providing quantitative measures of the sizes of surface features (relief map), the instrument provided false color images of selected portions of the surface. Figure 4.5 shows both plan and section views for the smooth top and bottom plates, as well as the roughened bottom plate. Details on the amplitude of roughness and a sample of the output of the profilometer are presented in the appendices.

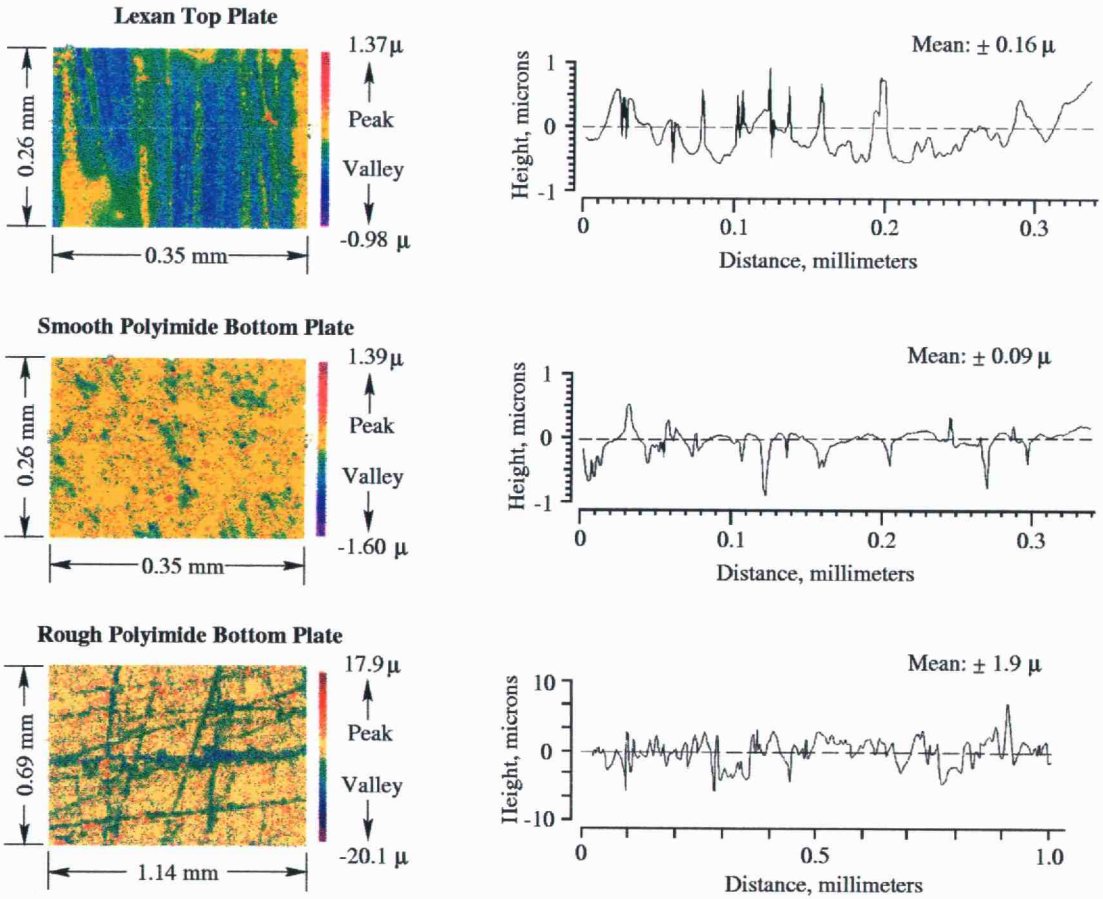

Figure 4.5. Surface roughness measurements for top and bottom surfaces.

4.2.3 Fluid flow measurements

As discussed above, pressures within the test section were measured with a pair of miniature pressure sensors (ENDEVCO models 8510C-100 and 8510C-50) threaded into ports in the bottom stainless steel plate. By running each experiment at an approximately constant downstream pressure (within the range of 1.75 to 2.7 bar gauge), the offset between the two sensors was held constant, enabling it to be measured and subtracted from the pressure drop readings. The resulting pressure drops through the test section were $\leq$ 0.95 bar gauge. The test section was grounded to the signal-conditioning unit to reduce 60Hz noise in the indicated pressure.

The signal received from the probe is processed and amplified using a field selectable isolated strain gauge (bridge) to DC transmitter, supplied by Absolute Process Instruments Inc., model API 4059G. The transmitter accepts strain gauge (bridge) input and provides an isolated DC voltage or current output. The 4059G circuitry contains a stable source of excitation voltage for use with bridge-type transducers. Also, it includes filtering and processing to allow effective use of low-level transducers. Some of the features of this transmitter are non-interactive zero/span controls, wide range of input/output parameters, easy set-up, input/output loop tracker LED's. The linearity of the signal is better than 0.1% of span, and temperature stability is better than 0.02% of span per degree C.

Pressures are acquired at a rate of 1000Hz and flow rates are acquired at a rate of 10 Hz. The readings are sample averaged for intervals of one second in length and the averages are logged to the computer's hard disk every second.

The plates in the bottom part of the test section assembly were sealed together (leak-proof) using thin layers of silicone vacuum grease. Air was bled from the system, in particular from the pressure ports, to reduce noise in the transducer signal.

The pressure drop was measured across selected portions of the channel. One transducer was installed at a fixed location, while the other was moved to various pressure ports down the length of the channel, such that a pressure profile at a fixed flow rate was obtained. The pressure drop is shown in Figure 4.6 in a 263 μm deep channel vs. the distance from the channel inlet, at a fixed flow rate of 685 ml/min (Re = 2336).

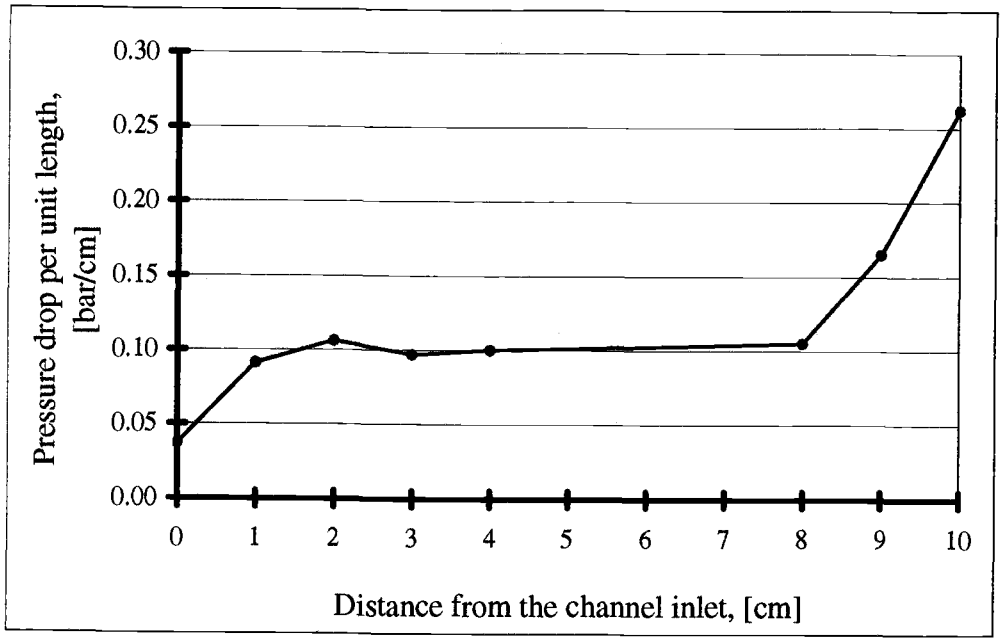

Figure 4.6. Pressure drop profile along the microchannel

Values were obtained by numerically differentiating a time-averaged pressure profile curve. In the inlet region of the channel the pressure drop was less that 0.1 bar/cm, while in the outlet region was greater than 0.1 bar/cm. In the middle 6 cm of the channel, the pressure drop was approximately constant at a value of 0.1 bar/cm. Thus, in the central portion of the channel the distance between the taps does not influence the measurements. For all determinations of the friction factor, upstream and downstream pressure sensors were installed at tap positions 3.048 cm away from the inlet and outlet regions, along the 4.064-cm middle region of the channel.

The offset between the two pressure transducers was measured for each experiment and was then subtracted from the recorded pressure drop. The offset was measured by stopping the flow and measuring the difference between the pressure indicated by each sensor, the result being averaged over several minutes of data collection. The magnitude of the offset varied from experiment to experiment due to variations in the mounting torque or electrical environment.

All experiments were run from high flow rate to low flow rate, except for the 1,050-micron-thick control spacer, where the experiments were run in both ways without observing any hysteresis. Valves were set to obtain the maximum flow rate through the channel, i.e. the lowest pressure at the downstream sensor. Flow rates were reduced in increments of approximately 10 – 25 ml/min. Averaged data were logged every second for 3 – 10 minutes at each flow rate. Temperatures, recorded every 15 minutes, during the experiment, showed small changes without influence on the measurements.

A Reynolds dye stream experiment was performed in the 263 μm-deep, smooth channel to verify the transition Reynolds number. The fluorescent dye used for flow visualization was a concentrated solution of Rhodamine 6G. Using a syringe pump, the dye was injected through a pressure tap hole in the microchannel at a maximum rate of approximately 5ml/min. The tap was positioned 2.032 cm from the inlet of the channel and 2 mm away from the sidewall. The Rhodamine particles were collected at the downstream filter.

The absorbance and emission spectra of Rhodamine 6G are broad, with maxima at roughly 525 nm and 555 nm, respectively. As a light source for dye excitation was used a Q-switched, frequency doubled Nd:YLF laser, operating at a wavelength of 534nm, which essentially floods the viewfield of the microscope. A pair of mirrors was used to direct the beam into the top of the test section. The output from the laser was pulsed at a frequency of 500 Hz. Scattered green light that entered the microscope was removed with a low-pass filter mounted within the body of the microscope. The fluorescent yellow light emitted from the dye was passed to a CCD-based video camera mounted on the microscope located at a position 5.08-cm downstream from the injection

point. The camera used was a JVC model KYF30BU 3-CCD color video camera mounted to the camera port of the microscope with a coupler (Diagnostic Instruments, model U31N). The camera was operated in its "high resolution" mode, wherein the entire frame is read once altogether at a 1/30sec rate. In this mode, the camera had a resolution of 640 horizontal by 480 vertical lines. The actual resolution of the system, as measured with a microscope stage-mounted graticule, was 340 pixels/mm, when viewing through a 10X objective lens. The camera's electronic shutter was operated at a speed of 1/500 of a second. Images were recorded on a laser videodisk recorder (Sony, model LVR 3000). Images were then captured later on a Power Macintosh computer model 8100/80AV running the image processing program NIH Image, version 1.61 (public domain software from the National Institutes of Health). In addition to capturing images, NIH Image was used for preliminary image processing which, in this case, was limited to adjusting the brightness and contrast of the image.

4.2.4 Heat transfer measurements

The refrigerant R-124 (1-chloro-1,2,2,2-tetrafluoroethane), used in heat transfer studies, flows from a warm, high-pressure reservoir to a cold, low-pressure reservoir. To minimize heat losses toward the environment, all piping and test loop components were insulated, except the top window in the test section.

The low flow rate flow meter (McMillan 102-3P) was used, as flow rates through the system varied from 20 ml/min to 100 ml/min. Both flow rate and the temperature at the flow meter were recorded by the data acquisition system to determine the compensation in density due to temperature variation.

A single pressure transducer (ENDEVCO model 8510C-100) was mounted in the test section, in the middle of the channel, i.e. at 5.080 cm from the inlet. The pressure indication was used for calibration of the RTDs and heaters on the heater plate and to determine the pressure in the test section during measurements. The pressure sensor was connected to the data acquisition system in the same manner as for flow measurements.

Due to manufacturing complications, the process of depositing RTDs on the topside of the channel was abandoned. Therefore, the data acquisition system collected and stored temperature information only from the bottom side of the channel.

Signals from the RTDs were collected through the specially designed PCB, which was in mechanical contact with the ends of the leads. For each experimental set-up, an end-to-end calibration was performed for each heater and each RTD, to eliminate the unknowns from the circuit. Details on calibration methodology and uncertainty analysis are given in the appendices.

The heater plate was attached to the 12.5 mm thick polycarbonate support plate, and the latter was, in turn, attached to the stainless steel bottom pressure plate, with thin, uniform layers of silicone glue. Special attention was given to remove sealant from the pressure tap holes, mounting screw holes, and from the inlet and outlet ports, as small bits of hardened sealant could interfere with the measurements or congest the microchannel or the piping toward the downstream filter.

The test section was carefully assembled with the desired polycarbonate spacer and the plates were tightened together using mounting screws and clamping mechanism. Two additional C-clamps were used to ensure that the test section was leak-proof, as the spacer was not glued to the heater plate or top clear Lexan® plate. A vacuum pump was used to remove air from the system, and to check whether or not the test loop was sealed. The refrigerant R-124 was then allowed to flow from the hot reservoir.

The temperature of the fluid used to cool the upstream heat exchanger is maintained at 4°C; for the downstream heat exchanger the temperature was maintained at 3°C. The fluid temperature at the microchannel inlet was approximately 10°C, because of heat losses to the environment. The test loop was located in an air-conditioned room, with air temperature of around 20°C. The air temperature was measured during the experiment using a regular thermometer and values were logged separately. The temperature of the hot bath was maintained in the range 38 – 42°C ensuring a hot

reservoir pressure of 60 – 85 psi. The bath temperature was carefully monitored and a safety relief valve was set at 100 psi (about 45°C). Even though properly insulated, the cold bath experienced temperature variations ranging from 7°C to 15°C, but this did not influenced the measurements.

For each spacer thickness of 128 μm, 263 μm and 521 μm, the measurements were taken at five different flow rates varying from 20 ml/min to 100 ml/min in roughly equal increments of 20 ml/min. Therefore, values of the flow rates were not exactly the same for all measurements, but close enough such that a comparison could be made.

Once a flow rate was set, power was supplied to each heater to provide a uniform heat flux boundary condition. The power output from the heaters was adjusted incrementally, in roughly equal steps, from zero watts/heater to a maximum value. This maximum value was reached when small bubbles, and thus two-phase flow, were observed at the last heater. As a check at the end of the experiment, the power output was brought back to zero and another measuring was made.

A period of 15 – 25 minutes elapsed between establishing each power output level, and data logging to assure that the system was in steady state.

Software was programmed to record the temperature of the bottom surface and to evaluate the heater resistance according to the calibration. Voltages supplied from the heater control panel were recorded as well and, using temperature corrected values for resistances, the software performed the computation and displayed power values on the monitor display. The averaged data for temperature, voltage and power were logged every second for 1 – 3 minutes at each measuring condition.

At the end of each experiment, fluid was removed from the test loop.

5. THEORETICAL MODEL AND DATA ANALYSIS

A significant amount of data was collected using the test loop presented in the previous chapter. In the following sections of this chapter, experimental results for fluid flow and heat transfer for rectangular channels ranging from macroscale to microscale will be presented and discussed. The results are compared with theoretical values determined using macroscale fluid flow and heat transfer theory presented in Chapter 3.

Based on the heat transfer theory presented, a computer program was developed to numerically model the heat transfer process for fluid flow in a large aspect ratio rectangular channel (2-dimensional flow).

5.1. Fluid flow; friction factors and pressure drop

In fluid flow studies, Reynolds number (Re), Darcy friction factor (f), and friction coefficient ($f \cdot Re$) were calculated for each operating condition. Reynolds numbers were calculated based on the mean hydraulic diameter of the channel. In classical fluid flow theory, the friction coefficient for developed laminar flow is a function of aspect ratio and is independent of Reynolds number (Shah and London, 1978).

Each of the following plots includes approximately 7,000 data points logged at a rate of one point per second. Each point represents an average over one second of 1,000 or 10 measured data for pressure or flow rate, respectively. The thin dashed lines represent the upper and lower limit, respectively, of the confidence interval for the quantity ($f \cdot Re$), obtained from the uncertainty analysis. The heavy dashed line represents the classical result for developed laminar flow in a rectangular duct.

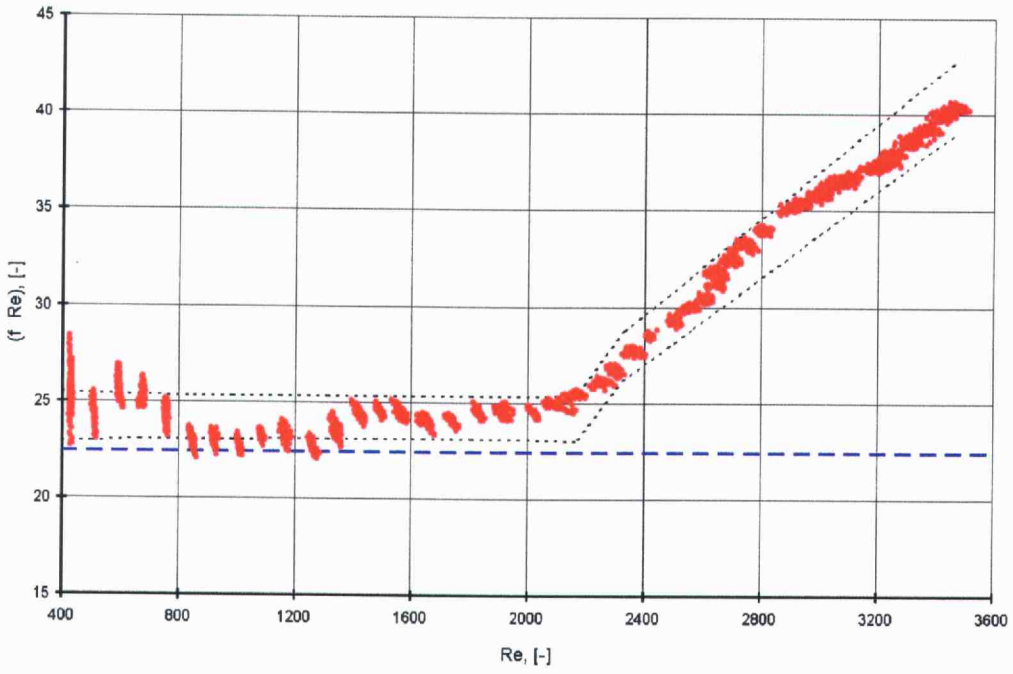

Figure 5.1. Friction coefficient for the 521 µm deep channel, smooth bottom

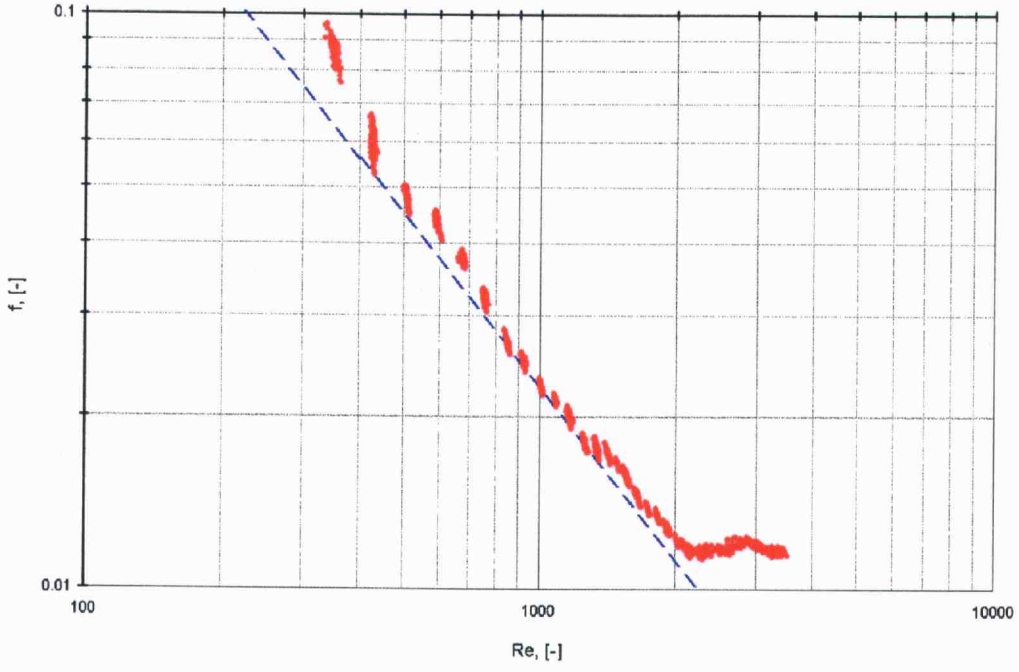

Figure 5.2. Friction factor for the 521 µm deep channel, smooth bottom

In Figure 5.1 the friction coefficient is shown as a function of Reynolds number for the 521 μm deep channel, with a smooth bottom plate. For developed laminar flow in a rectangular duct with an aspect ratio of 19.19:1, the classical result is $(f \cdot Re) = 22.4$ (Shah and London, 1978).

The average of the friction constant $(\overline{f \cdot Re})$ remained constant at approximately 24.2 ± 1.3 for Reynolds numbers less than about 2,200. This was presumed to be the region of laminar flow. The small oscillations seen in $(\overline{f \cdot Re})$ with flow at low Reynolds numbers were the result of a slight non-linearity of the turbine flow meter. The measured value of the friction constant was significantly higher than the classical value.

The friction factor (Figure 5.2) is seen to become constant, with a value of 0.012, at high Reynolds numbers. A constant friction factor indicates fully turbulent flow in a rough conduit. No power law behavior was observed for the turbulent friction factor. The transition to turbulence occurred at the Reynolds number where $(\overline{f \cdot Re})$ began to increase with *Re*. In this case, the transition is seen to occur at a Reynolds number of approximately 2,200. As noted by Peng *et al.* (1994a), the transition to turbulent flow occurs at relatively low *Re* in microchannels.

Dye stream experiments were also performed to verify the flow regimes indicated by the measurements of the friction factor. Unfortunately, the images for this channel depth were not sharp enough to be useful.

Similar results are shown in Figure 5.3 for the 263-μm deep channel with a smooth bottom plate. The theoretical value of 23.2 for the friction factor in the laminar regime is shown to be substantially below the experimental result of 26.1 ± 2.3. The fact that the deviation from macroscale theory persisted as the channel depth was reduced by 50 percent, indicates that entrance length effects are not the cause. Entrance contributions to pressure drop must decrease with decreasing channel depth, for fixed transducer locations.

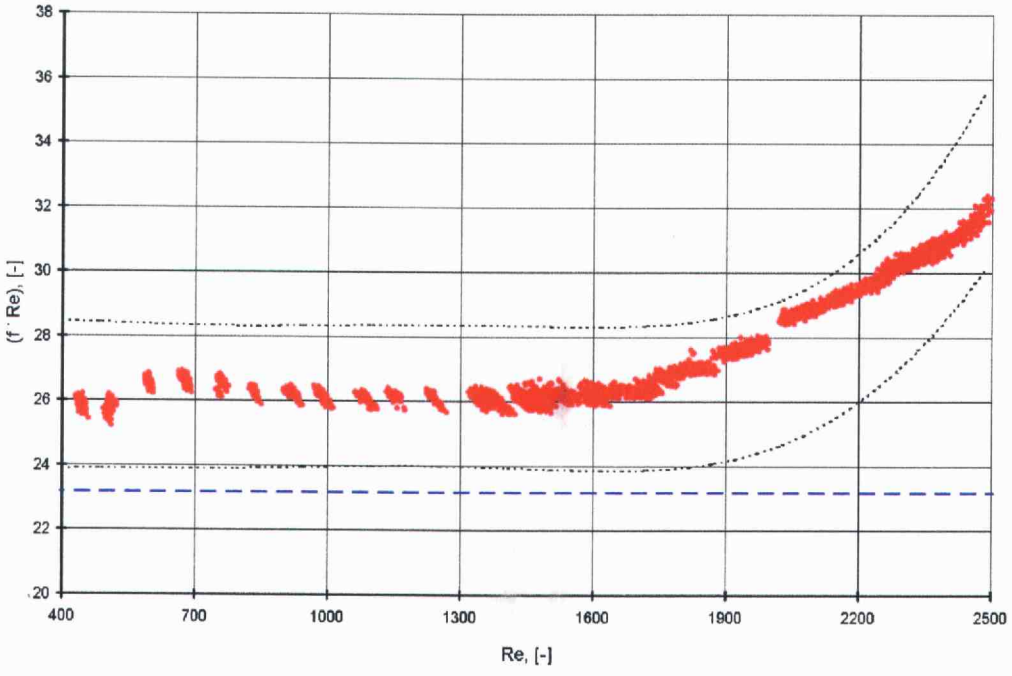

Figure 5.3. Friction coefficient for the 263 µm deep channel, smooth bottom

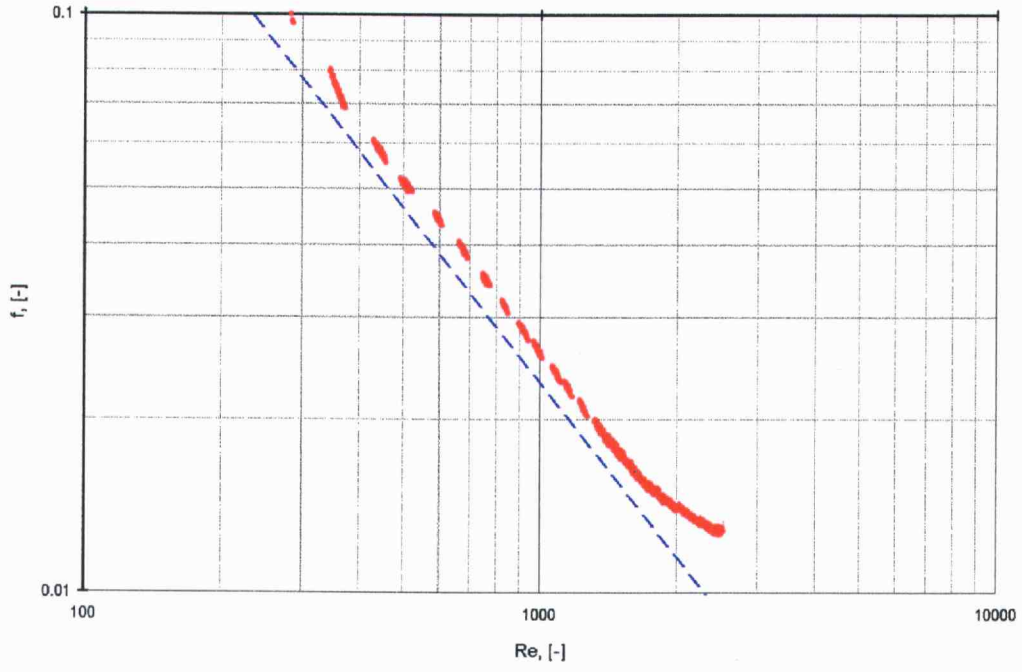

Figure 5.4. Friction factor for the 263 µm deep channel, smooth bottom

For this channel, the product $\overline{f \cdot Re}$ was an increasing function of Re for Reynolds numbers greater than approximately 1,700 and was constant for lower Reynolds numbers. The transition to turbulence occurred at lower Reynolds numbers as the channel depth was reduced.

A dye stream flow visualization of the experiment was performed to verify that the flow actually was laminar for $Re < 1{,}700$ and turbulent otherwise. As presented in the previous chapter, the dye was injected through a pressure tap positioned 2.032 cm from the inlet of the channel and 2 mm away from the wall of the channel. Images were recorded at a position 5.080 cm downstream from the injection point.

Dimensions for the video photomicrographs shown in Figure 5.5 are approximately 1.88 mm × 1.41 mm. The plane of the image is parallel to the microchannel and is positioned at mid-channel. The photographs presented are for four different flow rates. In the upper left image, the Reynolds number was 1,511. The width of the dye stream in the figure is approximately 0.5 mm, the same as the diameter of the injection hole. The edges of the stream are sharp, indicating little transverse mixing. At this low flow rate, the regime was laminar. In the upper right image, the flow was still laminar for $Re = 1{,}586$. The appearance of the dye stream is nearly identical with the one for the previous flow rate. Increasing the Reynolds number to 1,723 caused the dye stream to expand and become diffuse, the lower left image showing much more transverse mixing of the dye, and the flow regime was thus turbulent. The change in the width of the dye stream occurred at approximately the same flow rate as the change in slope of the friction constant curve. The image in the lower right corner of Figure 5.5, where $Re = 2{,}064$, is showing more transverse mixing, thus fully turbulent flow.

The transition Reynolds number obtained from the plot in Figure 5.3 agreed with the value observed in the flow visualization experiment. The turbulent friction factor approached a value of 0.013 at high Reynolds numbers for the 263-μm deep, smooth microchannel.

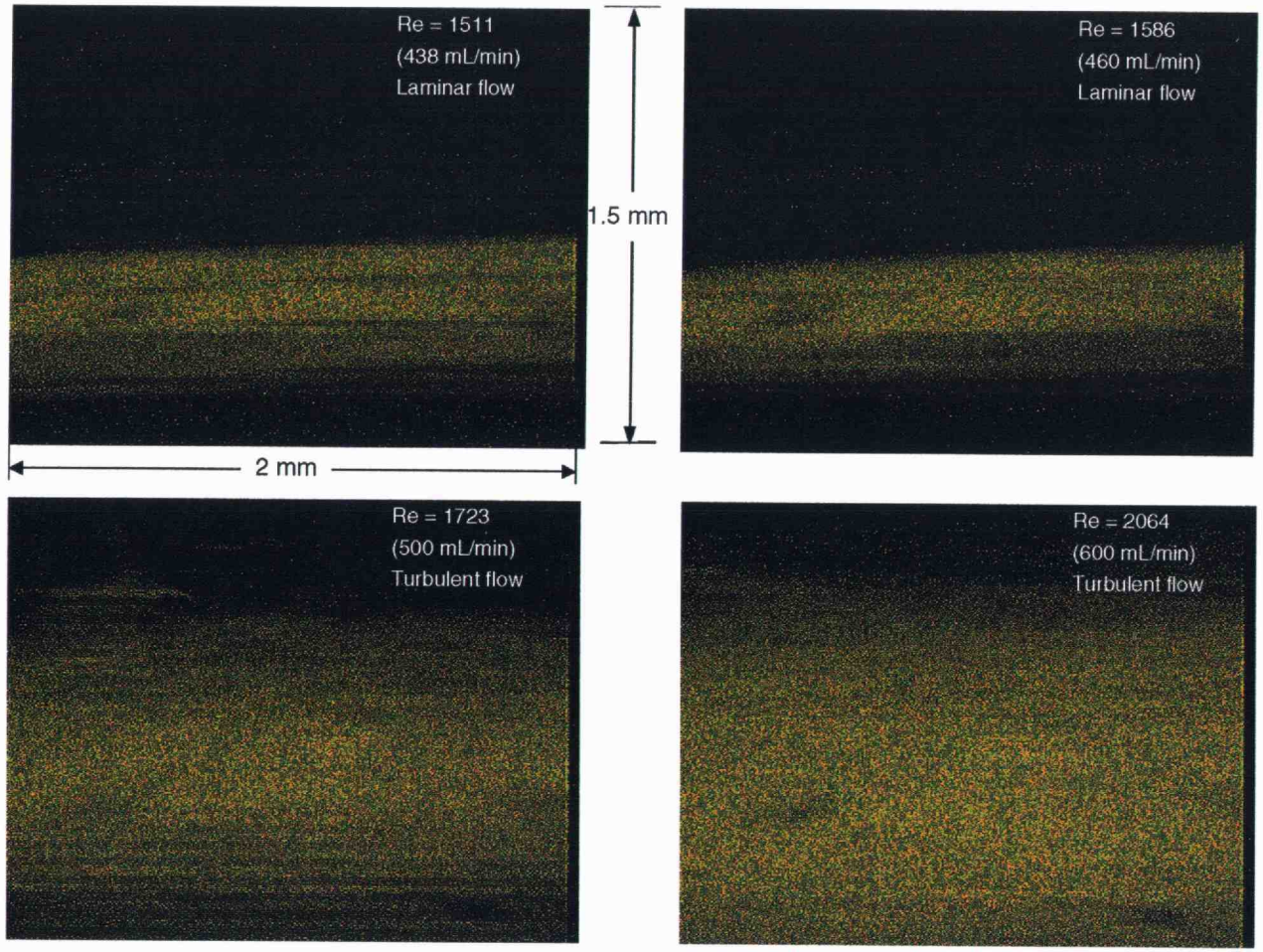

Figure 5.5. Reynolds dye experiment in a 263-μm deep channel

Notes: Dye was injected 2cm downstream from inlet, and pictures were taken 7 cm from inlet; liquid flows from left to right.
The imaged plane was rotated slightly.

The smallest channel examined had a depth of 128-μm; it was assembled with a smooth bottom plate. For this channel size, high-pressure drops did not allow turbulent flow to occur.

The results for the friction constant and friction factor vs. *Re* plotted in Figure 5.6 and Figure 5.7 are from two separate experiments. At low flow rates, the model 102-3P McMillan flow-meter was used; experiments for Reynolds numbers up to 800 employed the model 102-6P McMillan flow-meter. Flow was laminar over the range of Reynolds numbers examined. Average value of the friction constant at low *Re* was approximately 26.0 ± 2.8, which agreed with the classical value of 23.6 within the uncertainty of the experiment. The uncertainty in depth for this channel size was ± 5 μm, which is relatively large, making it difficult to distinguish measured friction factors from theoretical values.

As the high flow rates necessary to achieve turbulent flow regime were not attainable, the asymptotic value of the friction factor (Figure 5.7) could not be determined.

Experiments were also performed in a 1050 μm-deep channel that served as a control. For Reynolds numbers less than about 600, uncertainties in the transducer offset were high. For Reynolds numbers higher than about 1000 there was a possibility of undeveloped flow.

The product $\overline{f \cdot Re}$ was 21.8 for Reynolds numbers between 600 and 900, with uncertainties being ±1.4 at Re=600, and ±1.0 at Re=900. This result was in rough agreement with the theoretical value of 21.1. However, the offset between the pressure transducers was not reproducible to the accuracy required for these low-pressure drop, macrochannel experiments.

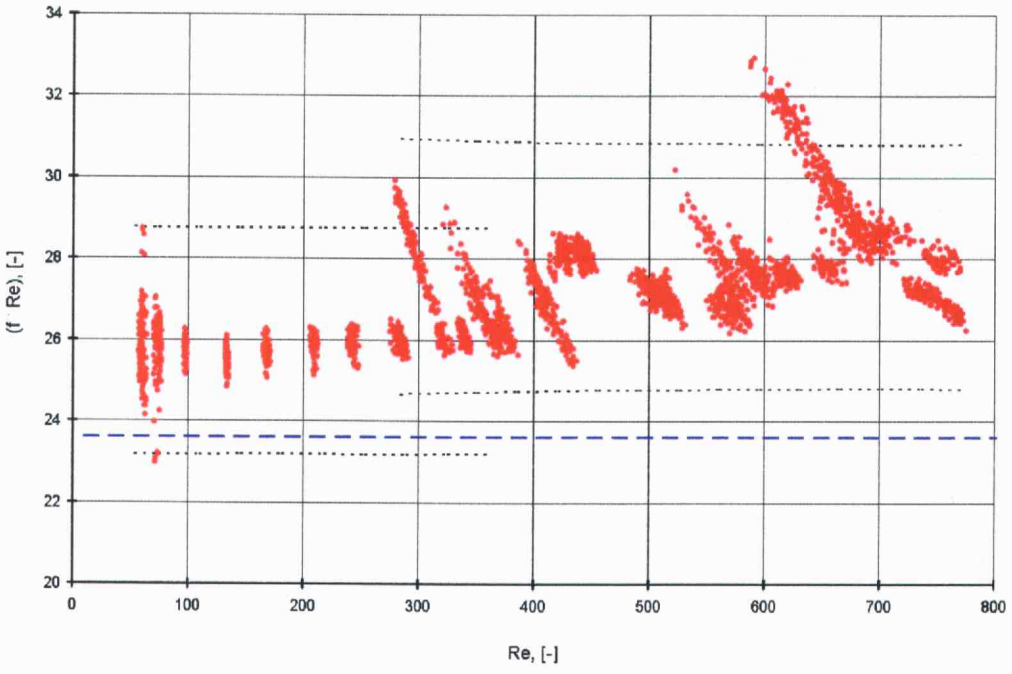

Figure 5.6. Friction coefficient for the 128 μm deep channel, smooth bottom

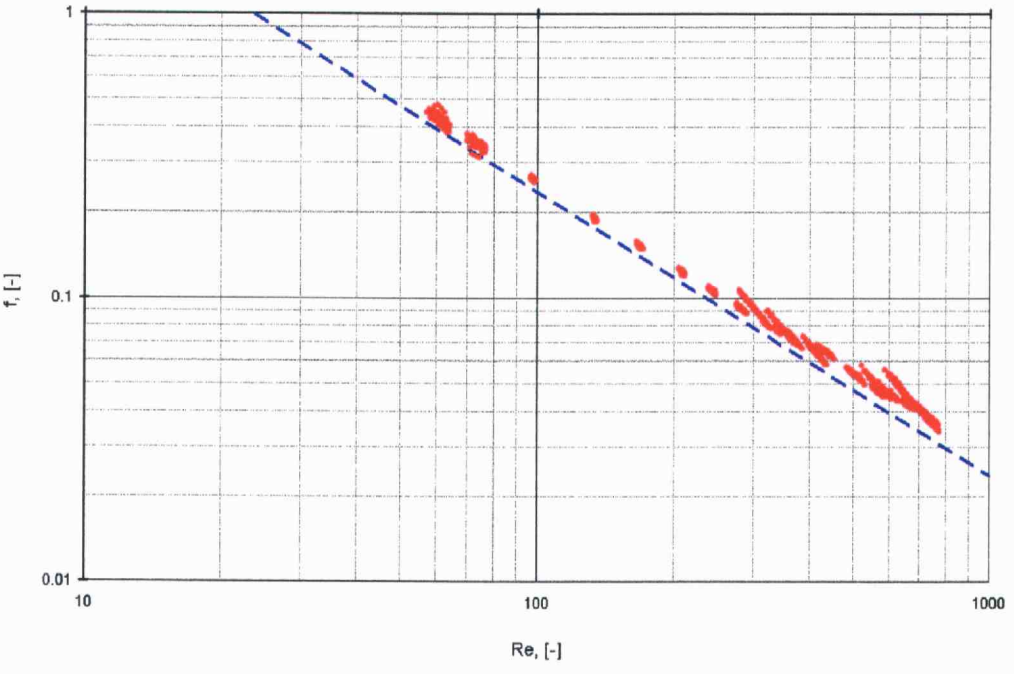

Figure 5.7. Friction factor for the 128 μm deep channel, smooth bottom

Friction factors in laminar flow increased well above theoretical values when the bottom wall of the channel was rough. Results obtained for the flow in the roughened 257-μm-deep channel showed values of $f \cdot Re$, plotted for $Re > 600$, approach an asymptotic value at approximately 29.0 ± 2.4, significantly above the theoretical value of 23.2. The plot may have some slight curvature at lower Reynolds numbers, but the uncertainty in the friction constant is large enough to encompass any presumed curvature. The value of Reynolds number for the transition to turbulent flow did not appear to shift from the value of 1,700 obtained in the smooth, 263-μm-deep channel. From friction factor results alone, it was difficult to determine the exact transition point. The friction factor in the turbulent regime approached a value of 0.016, considerably higher than the value for the smooth channel. Plotted in Figure 5.8 are friction coeffcients versus Reynolds number in two channels with nominal depths of 260mm. One curve displays the results with the smooth bottom plate installed, the other displays the results obtained with the rough bottom plate.

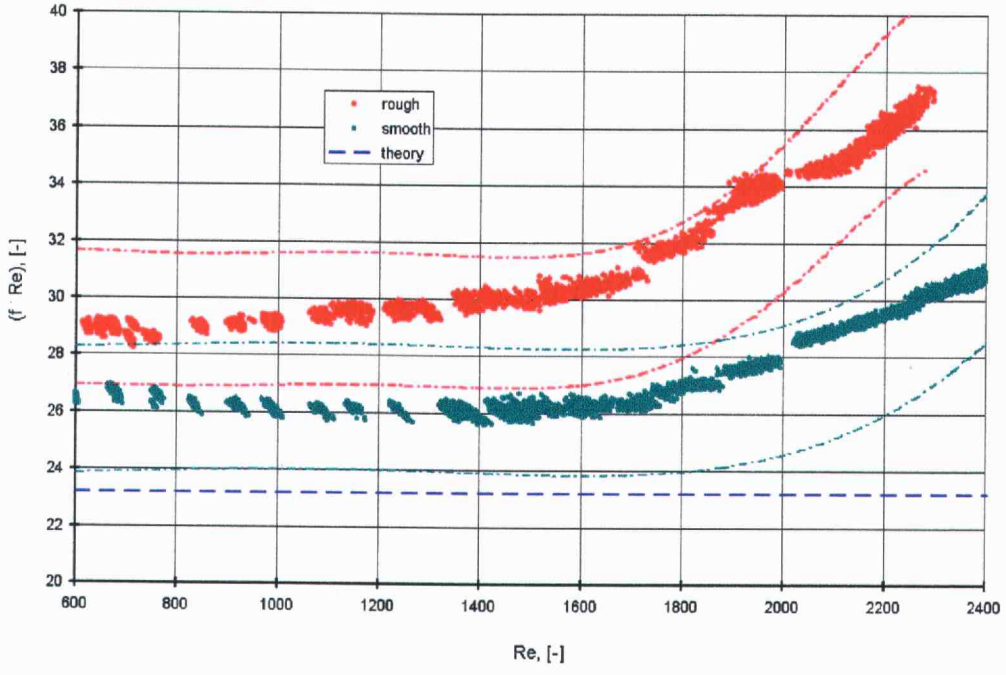

Figure 5.8. Friction constants for channels with nominal depths of 260 μm

5.2. Numerical model

To model heat transfer in rectangular channels numerically, several simplifying assumptions were made.

First of all, fluid flow was assumed to be developing in the first part of the channel, thus, at the location where heating started, the velocity profile was fully developed. Therefore, a fully developed parabolic velocity profile was assumed for the entire heated region. Second, the heating is assumed uniformly distributed from the surface of the heater's serpentine. Thus, a reasonable approximation is that the heating process can be represented on the vertical mid-plane of the channel. The computer model is thus two-dimensional. To meet stability and convergence criteria, grid sizes could not be decreased below certain values. This required some round off of the exact values of the channel depth, as follows: 520 μm instead of 521 μm, 260 μm instead of 263 μm, and 130 μm instead of 128 μm.

As input data, experimentally measured values of flow rate and power input were used. To have a common base for comparison, all computer runs were made with an assumed inlet fluid temperature of 10°C. For easier debugging and data handling, the code was divided in two parts. The first part determined the temperature profile at the mid-plane along the microchannel. The second part computed values of the Nusselt number and displayed the results.

For both parts, the code took into consideration the temperature dependency of the fluid parameters. The manufacturer delivered the refrigerant along with the properties table for density (ρ), specific heat (c_p), thermal conductivity (k), kinematic viscosity (μ), from which thermal diffusivity (α), dynamic viscosity (ν), and Prandtl number (Pr) may be obtained. The values from properties table were plotted in a graph and trendlines were determined (Figure 5.9.), for easier computer code implementation.

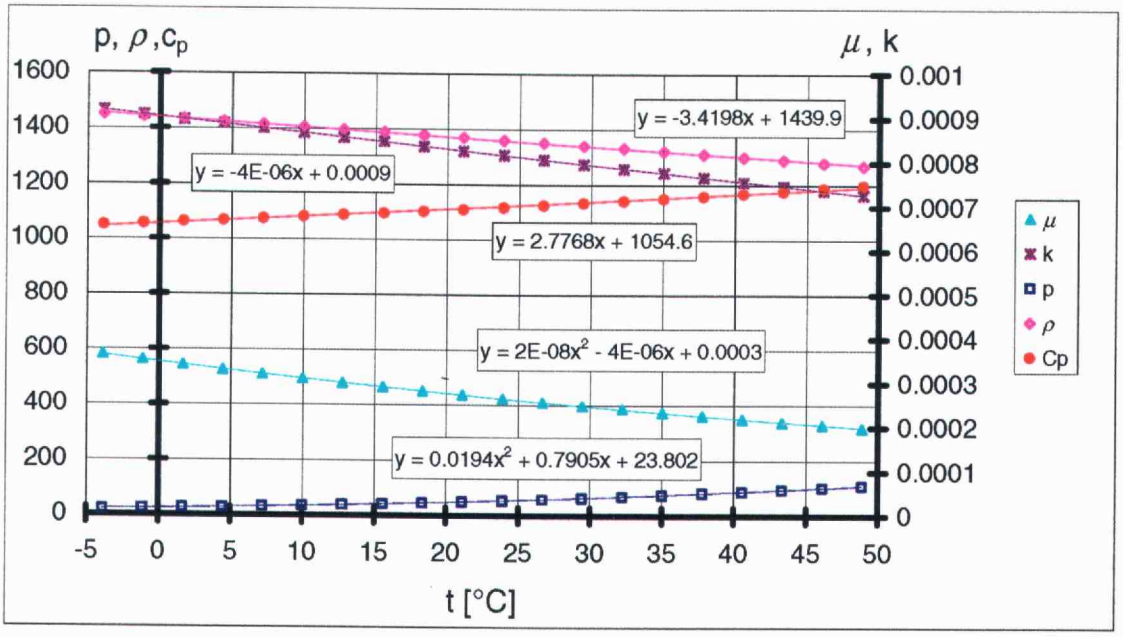

Figure 5.9. Physical properties of refrigerant R-124 and mathematical expressions of the trendlines

Except for pressure, expressed in British units, p [psia], all fluid properties are expressed in SI units, as follows: density, ρ [kg/m^3], specific heat, c_p [J/kg·°C], kinematic viscosity, μ [kg/m·s], thermal conductivity, k [W/cm·°C]. Temperature is expressed in degrees Celsius.

The computer code numerically determined the temperature field in several iterations, for each of them the properties being updated at each individual grid node, as functions of temperature.

For power input values several computations and estimates were required. The goal of heat transfer measurements was to simulate the uniform heat flux (Neumann) boundary condition for the heating surface. The rest of the channel walls were considered insulated, as the heat transfer coefficient is much lower compared with values obtained for the bottom of the channel.

The model took into account the fact that, on the vertical mid plane along the channel, the heating is not continuous. Two cases were studied:

- The actual heating process, were the heat input occurs periodically, alternating segments with non-zero heat input with segments with zero heat input. The latter represent the gaps between heaters, where the RTDs and the pressure taps are located, and the gaps in between the serpentines of the heater. To get heat flux values, the values for power supplied by data acquisition system are divided by the active surface area of one heater, 0.867 cm^2.
- The ideal heating process, with uniform heating over the entire surface studied. The heat flux value is obtained by dividing the sum of the individual power input (per heater) to the total surface area of the bottom of the channel.

A correction coefficient was introduced to account for heat losses. The partial differential equation solver from MATLAB (PDE toolbox) was used to estimate the heat losses. The scale representation of the heater plate and the bottom Lexan and stainless steel plates, as well as the properties of the materials were introduced in the solver.

Boundary conditions were specified for each individual surface. AP Armaflex insulation tape (TAP 18230 supplied by Armstrong World Industries, Inc.) was used to insulate the bottom side of the stainless steel plate, and thus this surface was considered perfectly insulated. The side surfaces for all three plates were exposed to the environment, whose temperature was measured to be 20°C during the experiment. The top surface of the heater plate was divided in three regions. For the middle region that represents the bottom of the channel a convective boundary condition was imposed along with heat generation, while the side regions, covered by the spacer, were considered insulated, due the low thermal conductivity of the polycarbonate.

Contact resistances between the plates depend on surface roughness, filling material, and pressure applied. They were estimated to be at least two orders of magnitude lower than the other thermal resistances and were neglected.

The physical problem presumes steady-state conditions, with constant values for parameters involved. The domain was discretized in a triangular mesh that could be refined for certain regions or over the entire domain. The resulting temperature distribution (Figure 5.10.) can be analyzed node by node, and temperature gradients or heat fluxes may be plotted. Analyzing the results for three cases, it was concluded that the heat losses are in the range of 1 – 4 percent of the total heat input. Therefore, for each particular case, corrected values were used.

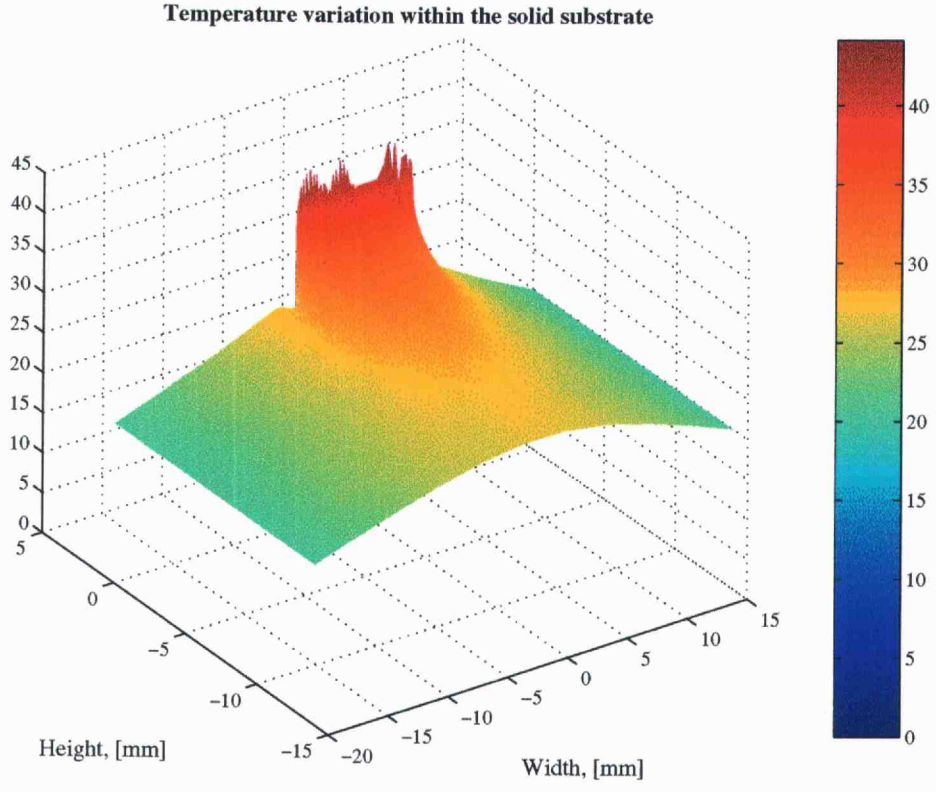

Figure 5.10. The output from PDE toolbox (MATLAB) from which the heat losses may be computed

Following the assumptions stated at the beginning of this subchapter, the particular form of the energy equation (3.27.) that applied was:

$$u \cdot \frac{\partial t}{\partial x} = \alpha \cdot \frac{\partial^2 t}{\partial y^2} \qquad (5.1.)$$

This is a second order, linear, homogeneous partial differential equation (PDE) that represents a steady propagation problem. The parabolic equation (5.1.) is first order in the x-coordinate and second order in y. To obtain a numerical solution of this equation, the continuous physical domain was discretized in a two-dimensional finite difference grid. Partial derivatives were then approximated by algebraic finite difference approximations, which were substituted in the original PDE to obtain an algebraic finite difference equation.

The rectangular finite difference grid is uniformly spaced in both x and y directions, but the grid step may be varied to assure that stability and convergence criteria are met. The x-direction grid step had to be small enough to account for all features of the heater plate, and it was chosen to be $\Delta x = 5\,\mu m$. The y-direction grid step was chosen either $\Delta y = 5\,\mu m$ or $\Delta y = 10\,\mu m$.

The parabolic PDE are solved numerically by marching methods. Explicit finite difference methods are conditionally stable and require a relatively small step size in the marching direction to satisfy stability criteria. Implicit methods are unconditionally stable, the step size being restricted by accuracy requirements, not stability requirements. For the implicit methods, finite difference equations are written for all nodes in a row, column, or for entire domain and then the system of equations is solved simultaneously. For this particular problem, due to the large number of nodes involved, an explicit solution method was chosen. Using Taylor series expansions of the dependent variable about a particular grid node a first-order forward finite difference approximation (FDA) in the x-direction and a second-order centered FDA for the y-direction were used:

$$t_x\Big|_{i,j}^{n} = \frac{t\Big|_{i+1,j}^{n} - t\Big|_{i,j}^{n}}{\Delta x} \quad ; \quad t_{yy}\Big|_{i,j}^{n} = \frac{t\Big|_{i,j+1}^{n} - 2 \cdot t\Big|_{i,j}^{n} + t\Big|_{i,j-1}^{n}}{\Delta y^2} \qquad (5.2.)$$

Defining the grid aspect ratio, β

$$\beta = \frac{\Delta x}{\Delta y}$$

the finite difference equation becomes

$$t\Big|_{i+1,j}^{n} = t\Big|_{i,j}^{n} + \frac{\alpha \cdot \beta^2}{u \cdot \Delta x} \cdot \left(t\Big|_{i,j+1}^{n} - 2 \cdot t\Big|_{i,j}^{n} + t\Big|_{i,j-1}^{n} \right) \qquad (5.3.)$$

In the above equations, t_x represents the first derivative of temperature with respect to x, t_{yy} represents the second derivative of temperature with respect to y, and subscripts i and j are identifiers for rows and columns, respectively. As several iterations are required to reach a solution, the superscript n denotes the iteration number. At the end of each complete iteration cycle, the error is checked for every node. Even though a thousandth of a degree represents enough accuracy for temperature, the benchmark error was set to $\varepsilon = 0.0002$.

From the stability analysis performed with a von Neumann method, it follows that the approximation used for equation (3.27.) is conditionally stable, with the condition

$$0 \le \frac{\alpha \cdot \beta^2}{u \cdot \Delta x} \le \frac{1}{2}$$

The solution obtained for the temperature profile on the vertical mid-plane of the channel was saved on disk, and then further analyzed to obtain the local values of the Nusselt number. In Figure 5.11 solutions for two specific cases are shown, all cases being analyzed using the same methodology. Solutions are for a 128-μm spacer, with flow rate of 40 ml/min, for actual and uniform heating, respectively.

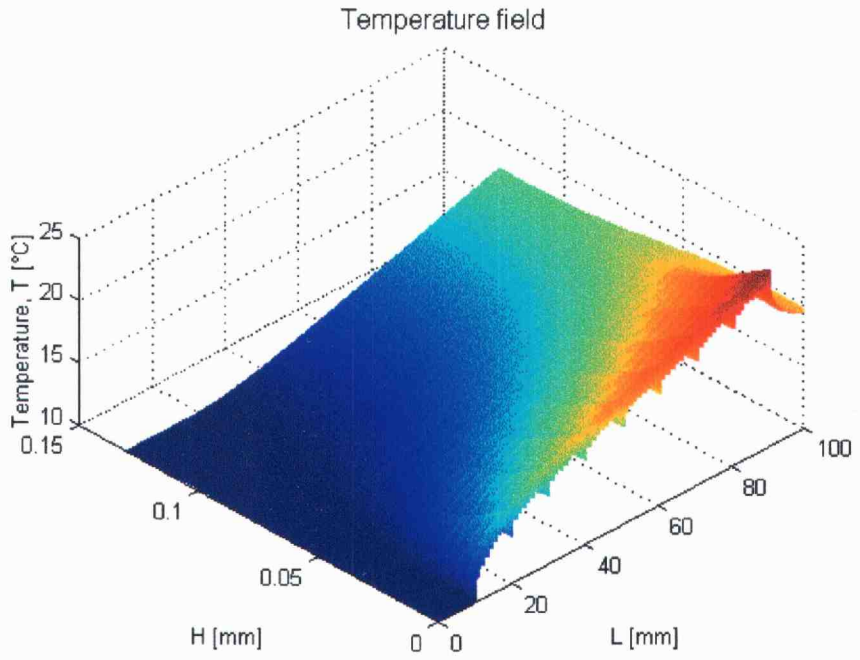

a)

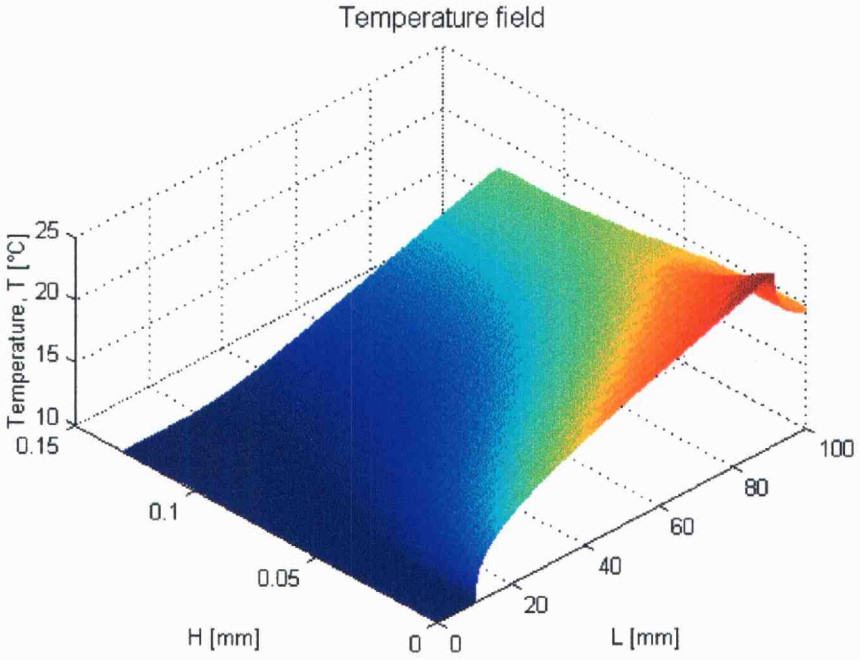

b)

Figure 5.11. The numerical solution for the temperature profile on the vertical mid-plane of the channel: a) actual heating; b) ideal uniform heating

The second part of the MATLAB program was that of computing the local values for Nusselt number. Using Simpson's $\frac{3}{8}$ rule, the temperature profile was numerically integrated and the bulk fluid temperature was computed. Having the surface temperature and the mixed mean fluid temperature, the local Nusselt number was computed using equation (3.35). The program lists the maximum or average values of parameters of interest: maximum fluid temperature, maximum surface temperature, and average values for thermal conductance, Reynolds number, and Prandtl number. Local values for temperatures and Nusselt number are saved in a data file. Values of interest for the 128-μm-spacer, with a flow rate of 40 ml/min are presented in Figure 5.12.

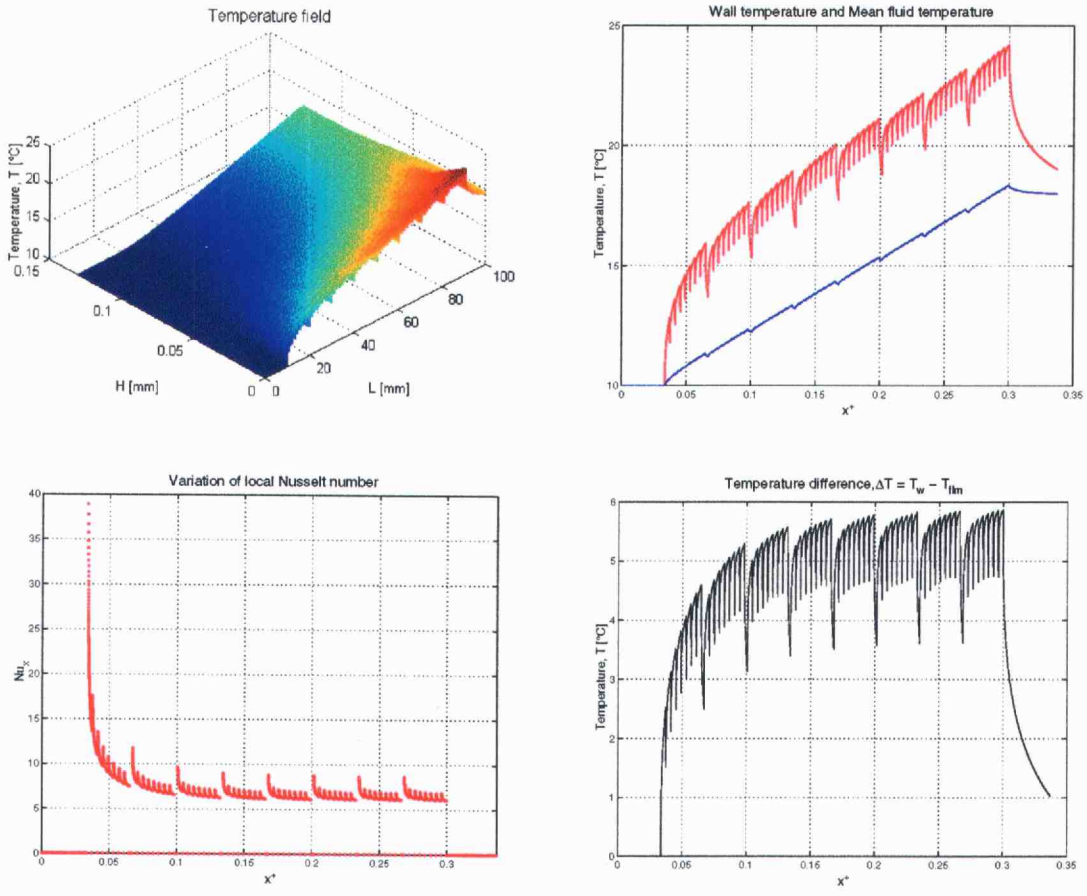

Figure 5.12. Graphic output of the numerical solution

5.3. Heat transfer. Local Nusselt number.

The local Nusselt number, Nu_x , was computed for each measuring point and plotted versus the dimensionless axial position, x^+. Figures in this section show experimental values for local Nusselt number and for wall temperature, along with the results of the numerical model, for the cases mentioned in previous subchapter.

As only the temperatures at the bottom surface were recorded, the bulk fluid temperature had to be determined analytically, using correlations from macroscale heat transfer theory. From the expression

$$q'' = \dot{m} \cdot c_p \cdot (t_m - t_{m,e}) \tag{5.4.}$$

where q'' is the heat input, $\dot{m}$ is the mass flow rate, c_p is the specific heat at constant pressure, and $t_{m,e}$ is the bulk fluid temperature at the channel entrance, the unknown bulk fluid temperature at a specific point along the channel, t_m, can be determined

$$t_m = t_{m,e} + \frac{q''}{\dot{m} \cdot c_p} \tag{5.5.}$$

The specific heat is temperature dependent, thus an iterative process was used. For a chosen value of fluid temperature, a value for specific heat was determined from property tables, and using equation (5.5.) the fluid temperature was computed. The mass flow rate was computed using the measured volumetric flow rate and the temperature corrected value for density.

Having evaluated the bulk fluid temperature, other fluid properties were computed; these being density, ρ, thermal conductivity, k, and viscosity, μ. Then, Reynolds number (Re) and Prandtl number (Pr), as well as the non-dimensional axial distance, x^+ were evaluated. Finally, local values for Nusselt number were computed using equation (3.35).

In the following figures results are plotted for three channel depths, 128 μm, 263 μm, and 521 μm, for flow rates up to 60 ml/min. Results for the large size channel, 521 μm, where experimental results coincide with numerical and theoretical predictions, indicated that it was unnecessary to perform experiments in the 1,050 μm deep channel.

For each channel size examined, the flow rate was varied from 20 to 60 ml/min in approximately equal 20 ml/min increments. In the range of flow rates examined, the flow regime was laminar, with Reynolds numbers between 300 and 1000.

Values of Prandtl number were in the range 3.7 – 3.9. From theoretical considerations presented in subchapter 3.2, for $Pr > 1$, the velocity profile develops more rapidly than the temperature profile, and for $Pr > 5$, the velocity profile leads the temperature profile sufficiently that a solution based on an already fully developed velocity profile will apply accurately, even though there is no hydrodynamic starting length. Therefore, the assumptions made in the numerical model are well founded, i.e. velocity profile is fully developed when the heating starts.

In all cases presented the power input was set at 1 W per heater. In computing the actual heat flux the same corrections regarding the actual surface area of the heater and heat losses were applied as for the numerical model.

In the literature, several researchers have reported asymptotic values for local Nusselt numbers vs. aspect ratio of rectangular channels. These apply to various channel configurations, as well as the number of walls heated.

Shah and London (1978) present values for the laminar Nusselt number for the heating case 1L (one wall heated, long side) that is applicable to the case studied in this work. Asymptotic values of local Nusselt number for the aspect ratios used in this experimental work were found using a least squares interpolation method for the values presented by Shah and London (1978).

Table 5.1. Values of laminar Nusselt number for the cases studied

Channel depth, [mm]	Aspect ratio, [-]	Nu, [-]
0.521	19.19 : 1	5.096
0.263	38.02 : 1	5.237
0.128	78.13 : 1	5.310

Should be noted that values presented in Table 5.1 apply for certain specific conditions (e.g., constant properties of the fluid). Therefore, asymptotic values shown in the following figures may differ, due to the fact that the computer program takes into account the variation of fluid properties with temperature. When run assuming constant fluid properties, the numerical model yielded values accurate within 0.1 percent of the values determined from macroscale theory.

A 521-μm thick spacer was used for the largest channel examined, with an equivalent hydraulic diameter of 0.99 mm. In Figure 5.13, Figure 5.14, and Figure 5.15 results are presented for various flow rates. For all cases, the channel was not long enough such that thermal fully developed conditions were achieved. The asymptotic value for the laminar Nusselt number in this case could not be determined.

Values for local Nusselt numbers obtained in this case compare closely with predictions from the numerical model. They accurately follow the predictions of the heating model that used the actual surface of the heater and macroscale correlations.

Values obtained at a flow rate of 20 ml/min closely match the numerical predictions. The overall uncertainty in local Nusselt number varied in the range of 4.2 – 4.7 percent, mainly influenced by uncertainties in temperature measurements and in channel depth measurements. Measured wall temperatures are slightly higher than numerical predictions. Uncertainties in temperature measurements, 1.8 – 3.1 percent, are due mainly to the calibration (±0.451°C). This had an influence on the values of thermal conductivity determined using the temperature dependent equation from Figure 5.9.

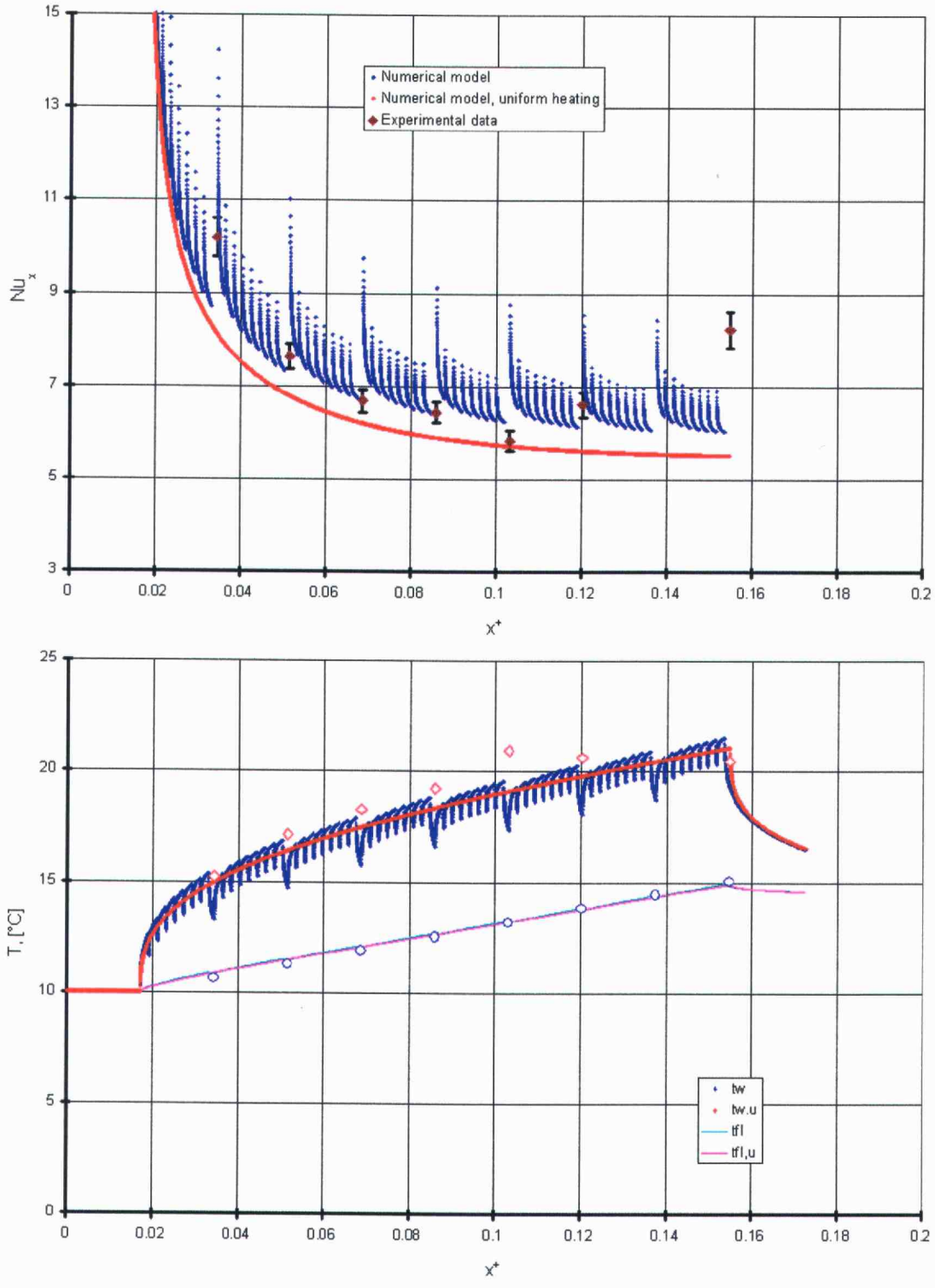

Figure 5.13. Case of 521 μm spacer, 20 ml/min; **top:** variation of local Nusselt number; **bottom:** variation of wall and fluid temperatures

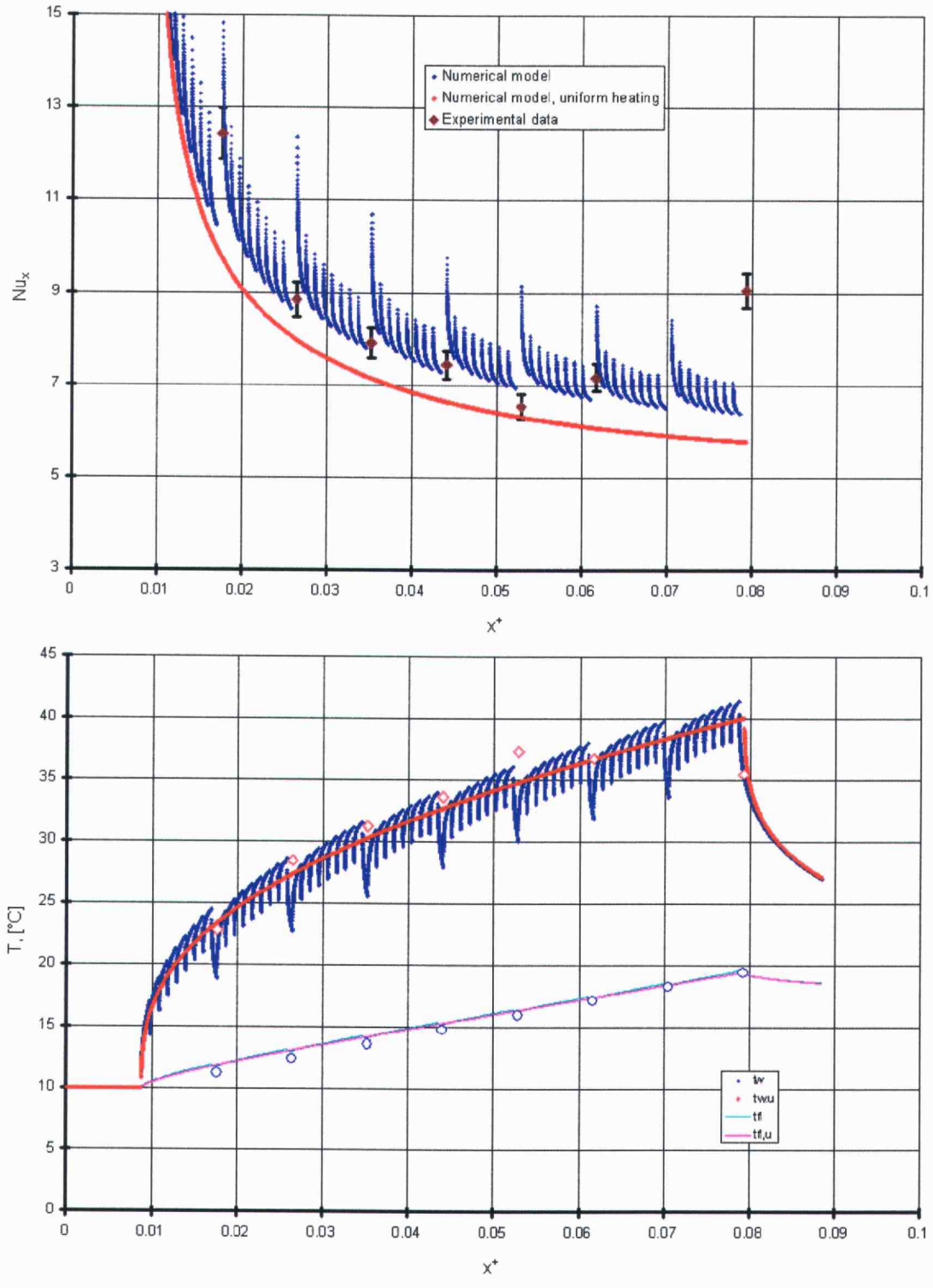

Figure 5.14. Case of 521 μm spacer, 40 ml/min; **top:** variation of local Nusselt number; **bottom:** variation of wall and fluid temperatures

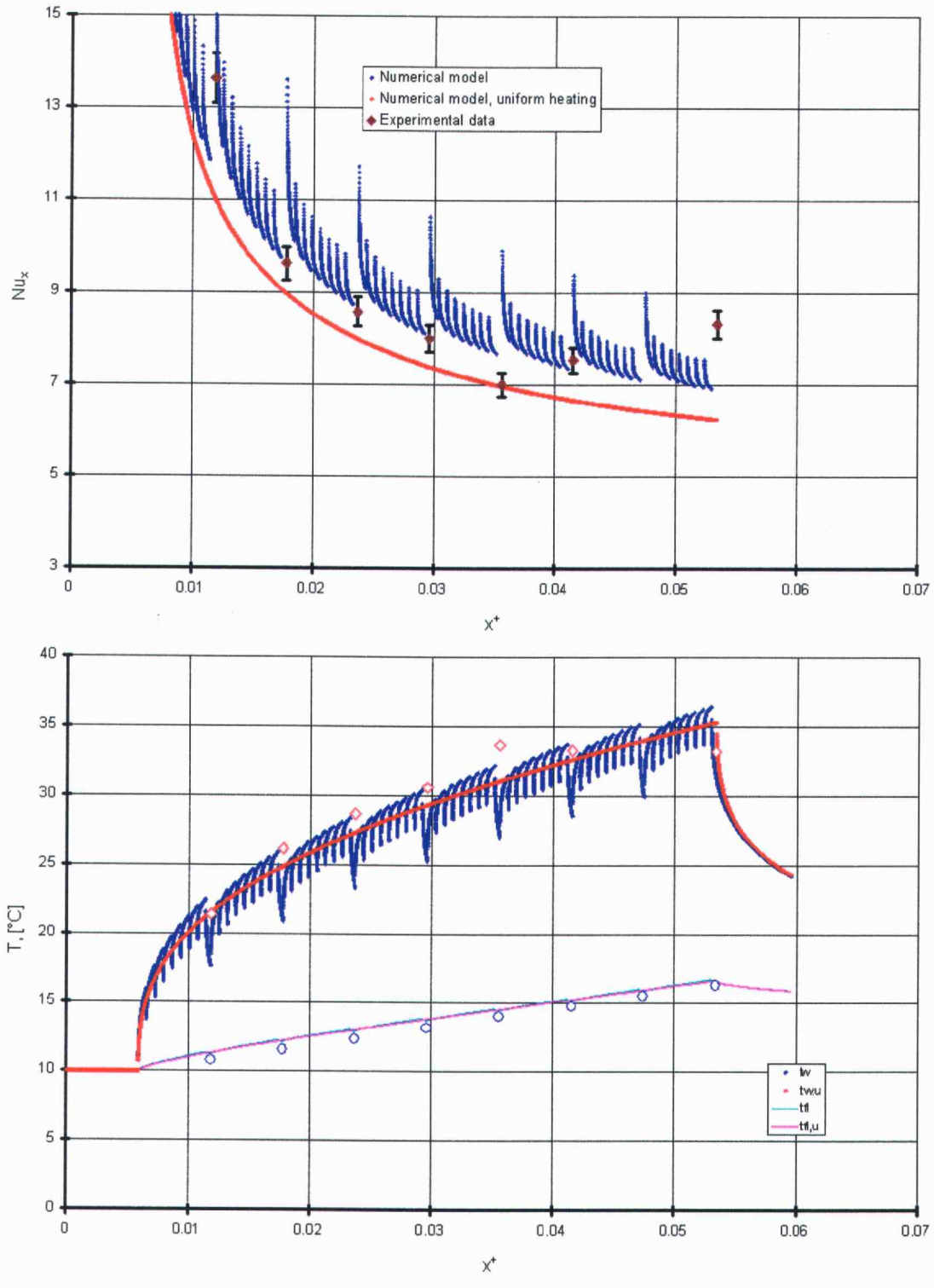

Figure 5.15. Case of 521 μm spacer, 60 ml/min; **top:** variation of local Nusselt number; **bottom:** variation of wall and fluid temperatures

Similar results were obtained at a flow rate of 40 ml/min, with the uncertainty in local Nusselt number values being 4.2 – 4.8 percent. Measured wall temperatures match numerical predictions with uncertainties within 1.2 – 3.9 percent; fluid temperature values are slightly lower than numerical predictions.

Figure 5.15 presents results for a flow rate of 60 ml/min, which are similar to the previous two cases. The overall uncertainty in local Nusselt number varied in the range of 3.9 – 4.5 percent, while the uncertainty in wall temperature measurements varied in the range 1.3 – 3.9 percent. Values for fluid temperatures were slightly lower than numerical predictions. It is seen that the confidence interval for the experimental data includes local Nusselt number values predicted numerically.

For the 263-μm deep channel, the experimental data showed the same general trend as for the previous case. Values of local Nusselt number were generally less than predictions from the numerical model, but the differences were not very large, in the range of 0 – 10 percent.

At a flow rate of 20 ml/min, local Nusselt numbers obtained from experimental measurements are in good agreement with numerical predictions, within the confidence interval determined from uncertainty analysis (Figure 5.16). The overall uncertainty varied in the range 5.2 – 6.1 percent, with uncertainty in temperature being the largest contributor. The calibration error was ± 0.733°C, representing the most significant part of the uncertainty in temperature.

Although similar observations may be made for the other two flow rates, 40 ml/min (Figure 5.17) and 60 ml/min (Figure 5.18), there is a slight decrease in values of local Nusselt number. A reduction of approximately 10 percent was observed in the case of the largest flow rate. The magnitude of the confidence interval remained roughly the same, between 5.2 – 6.9 percent, but this does not include the values predicted by the numerical model.

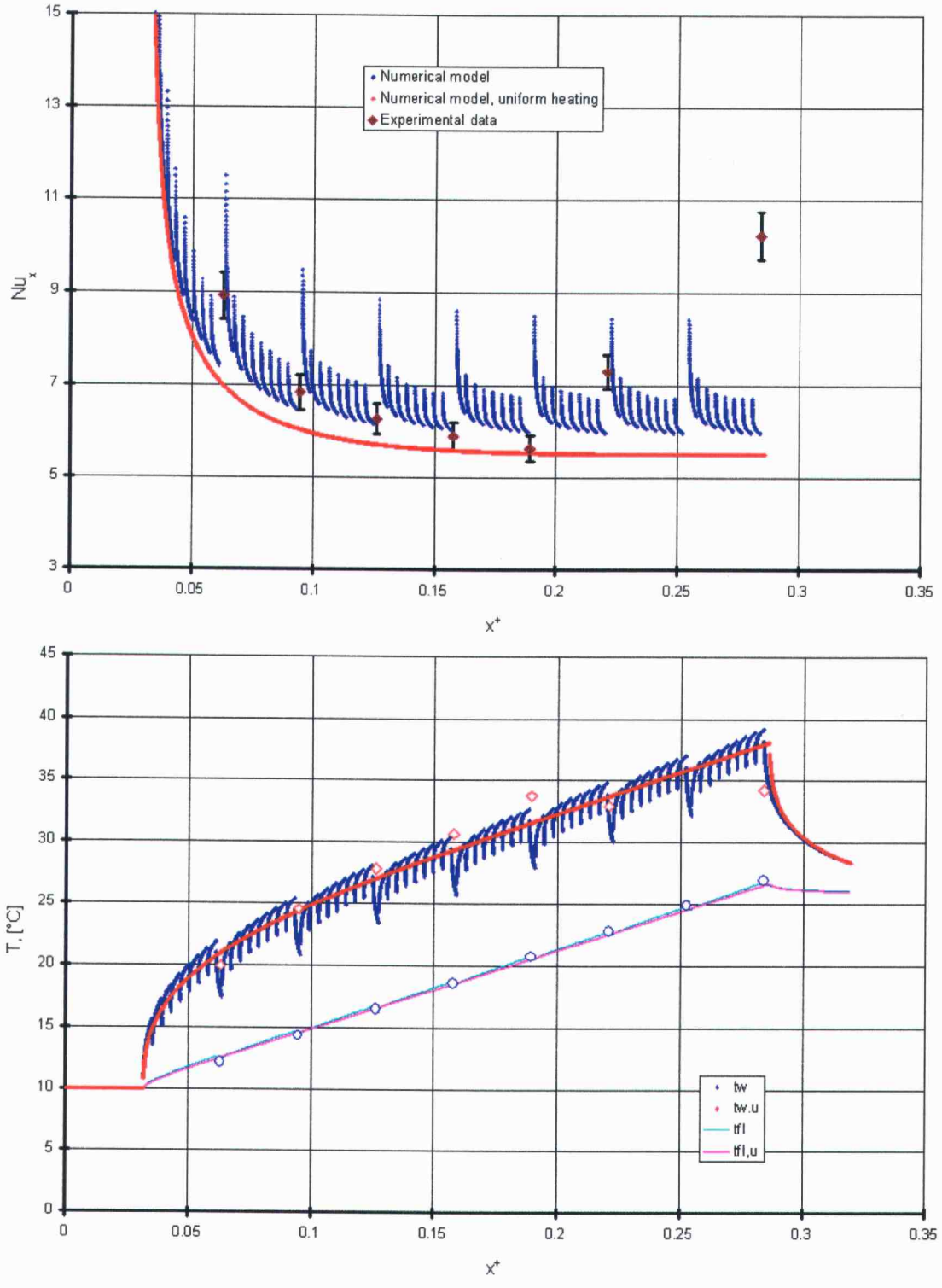

Figure 5.16. Case of 263 μm spacer, 20 ml/min; **top:** variation of local Nusselt number; **bottom:** variation of wall and fluid temperatures

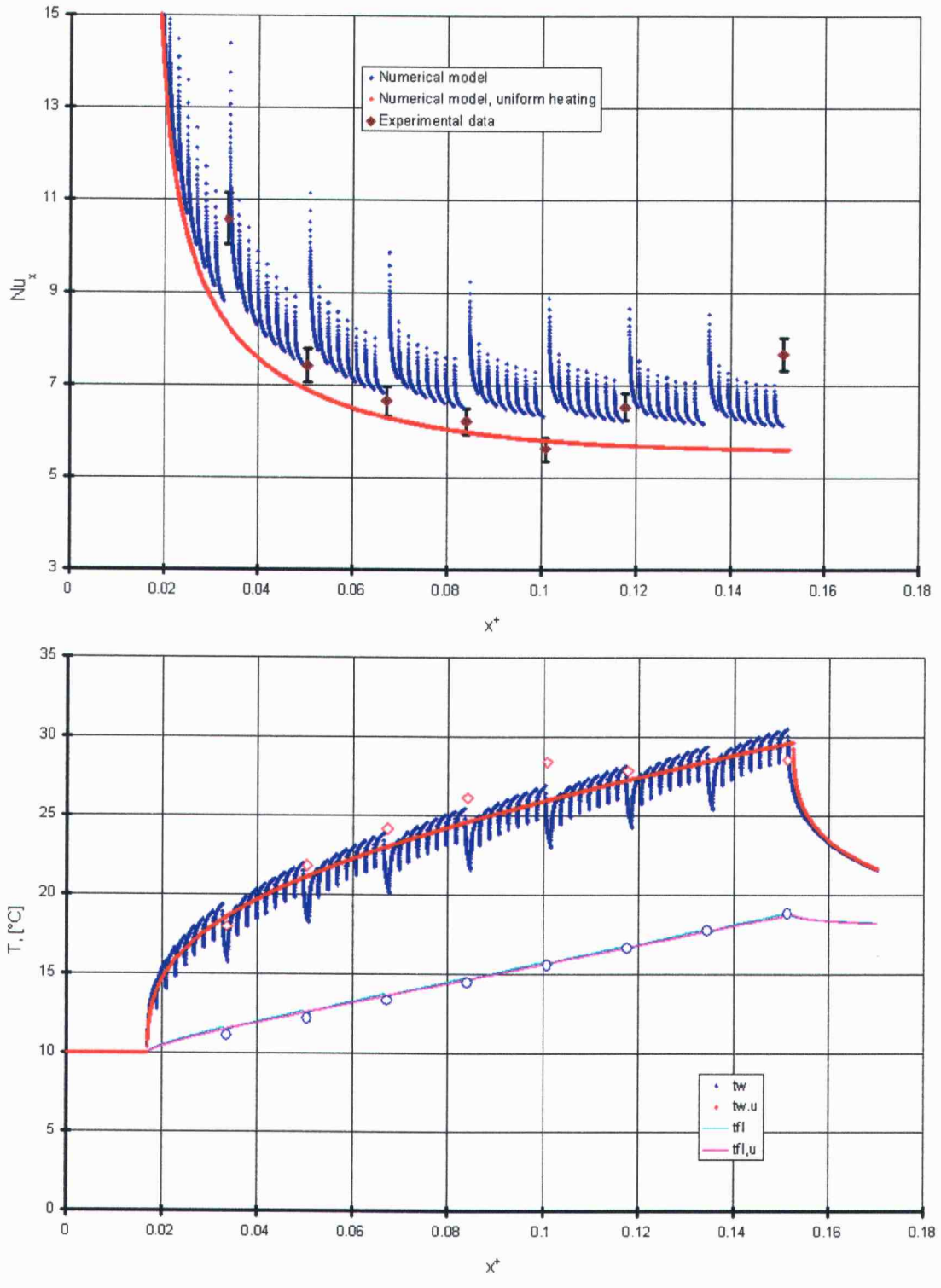

Figure 5.17. Case of 263 μm spacer, 40 ml/min; **top:** variation of local Nusselt number; **bottom:** variation of wall and fluid temperatures

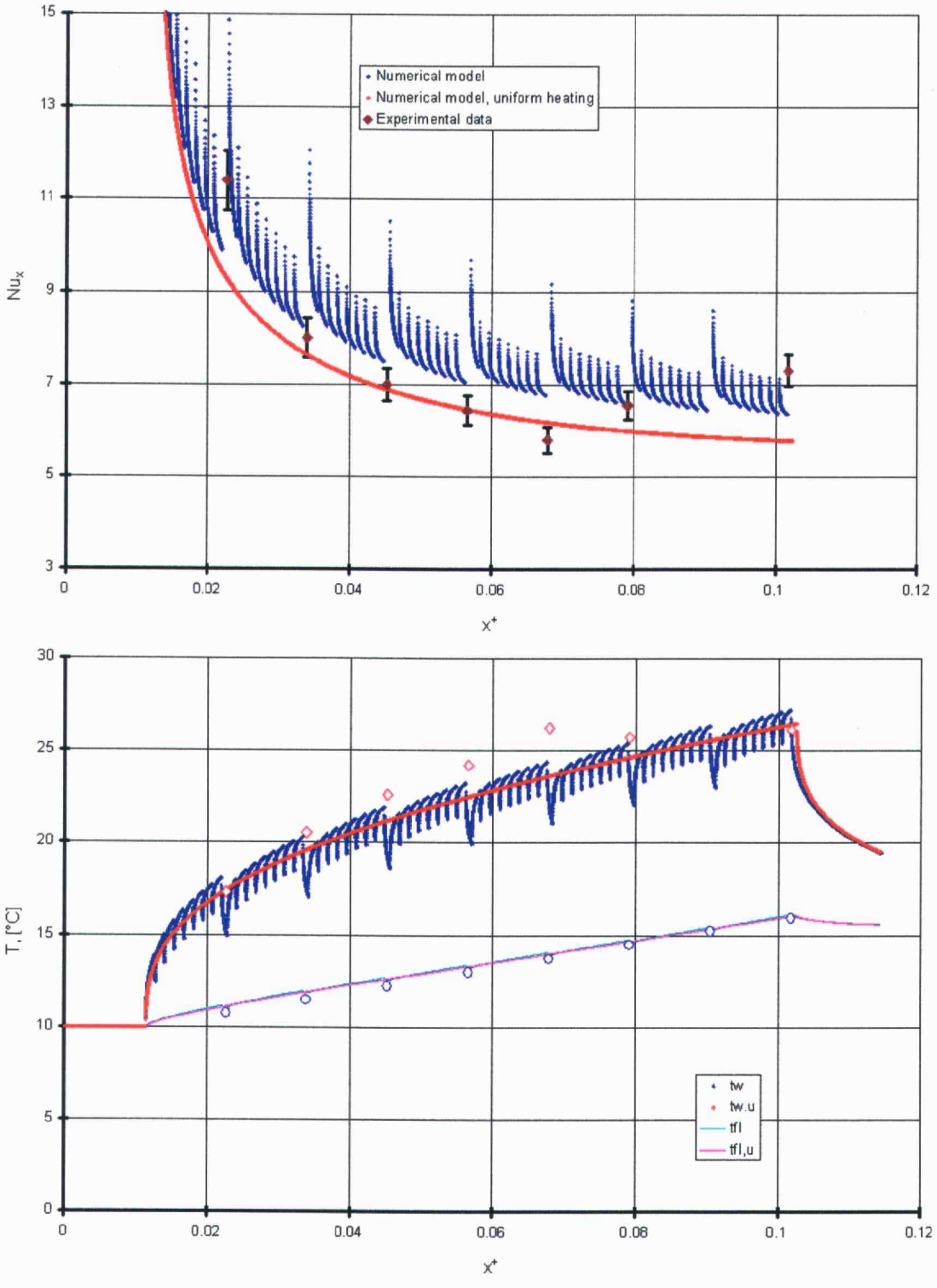

Figure 5.18. Case of 263 µm spacer, 60 ml/min; **top:** variation of local Nusselt number; **bottom:** variation of wall and fluid temperatures

For this channel size, it was possible to determine a value for the asymptotic laminar Nusselt number. As the non-dimensional axial length is inversely proportional to Reynolds number and channel geometry (hydraulic diameter), the asymptotic value was observed only for the lowest flow rate, 20 ml/min. The value obtained, Nu = 5.517, was 5.075 percent greater than the theoretical prediction of Nu = 5.237 (Table 5.1), which applies for constant fluid properties.

The smallest channel size analyzed was the 128-μm-deep microchannel. The data for three flow rates at this spacing exhibited a systematic departure from numerical predictions, i.e. from macroscale theory. Values obtained for local Nusselt number were significantly lower than predictions, in the range 15 – 25 percent.

For all cases studied for this channel size, the overall uncertainty in Nu_x was roughly the same, in the range 5.6 – 7.0 percent. The main effect was, again, the uncertainty in temperature, which varied in within 2.2 – 4.0 percent, but a large contributor was the uncertainty in channel depth measurement, 3.9 percent. The magnitude of the confidence interval was approximately the same for all three cases (Figure 5.19, Figure 5.20, and Figure 5.21). The temperature plots in these figures, show surface temperatures significantly higher than predicted from the numerical model.

An asymptotic value for the laminar Nusselt number was determined for this case as well. The numerically computed value of Nu = 5.63 was again greater than the theoretical value of Nu = 5.31.

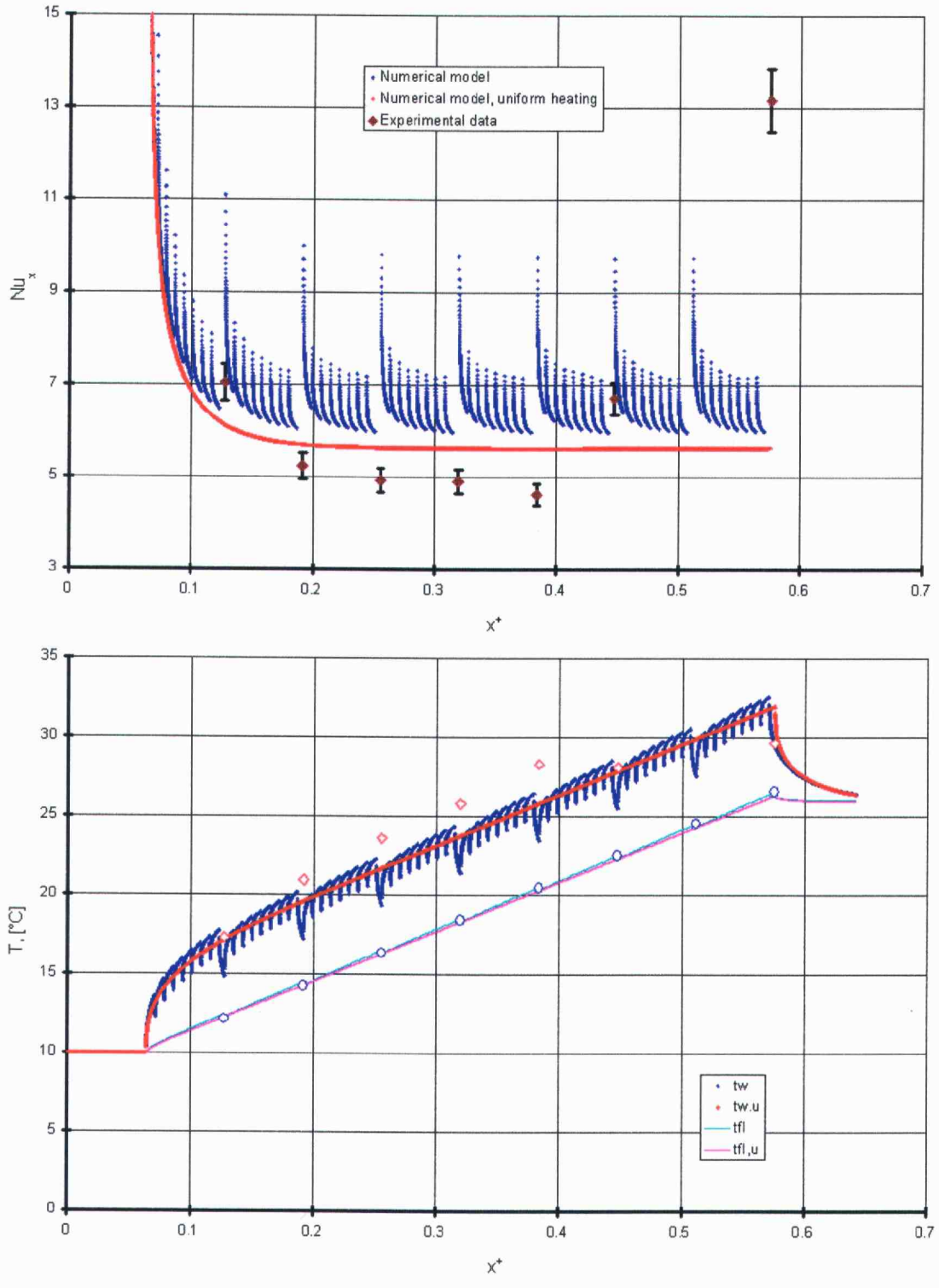

Figure 5.19. Case of 128 μm spacer, 20 ml/min; **top:** variation of local Nusselt number; **bottom:** variation of wall and fluid temperatures

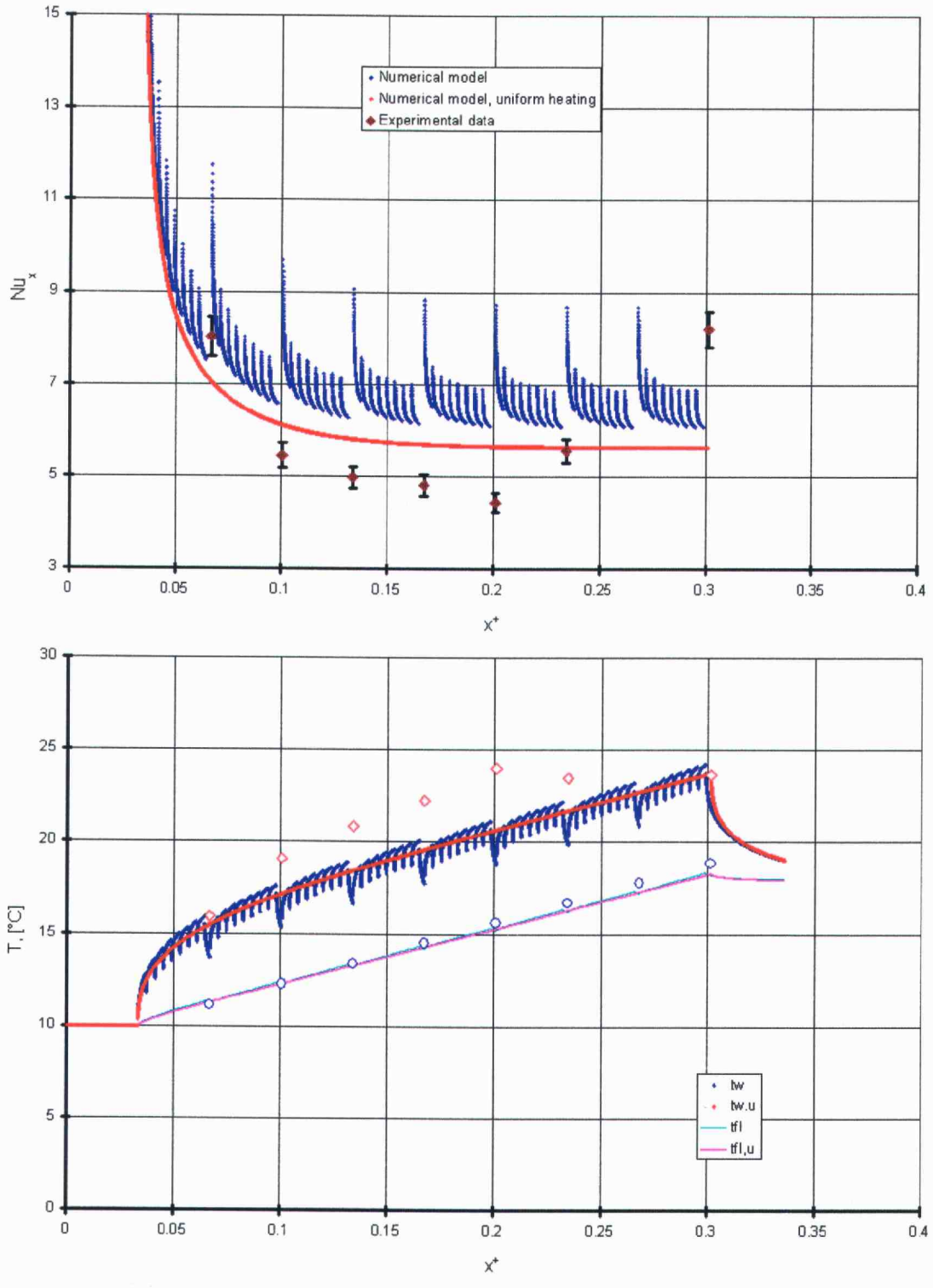

Figure 5.20. Case of 128 μm spacer, 40 ml/min; **top:** variation of local Nusselt number; **bottom:** variation of wall and fluid temperatures

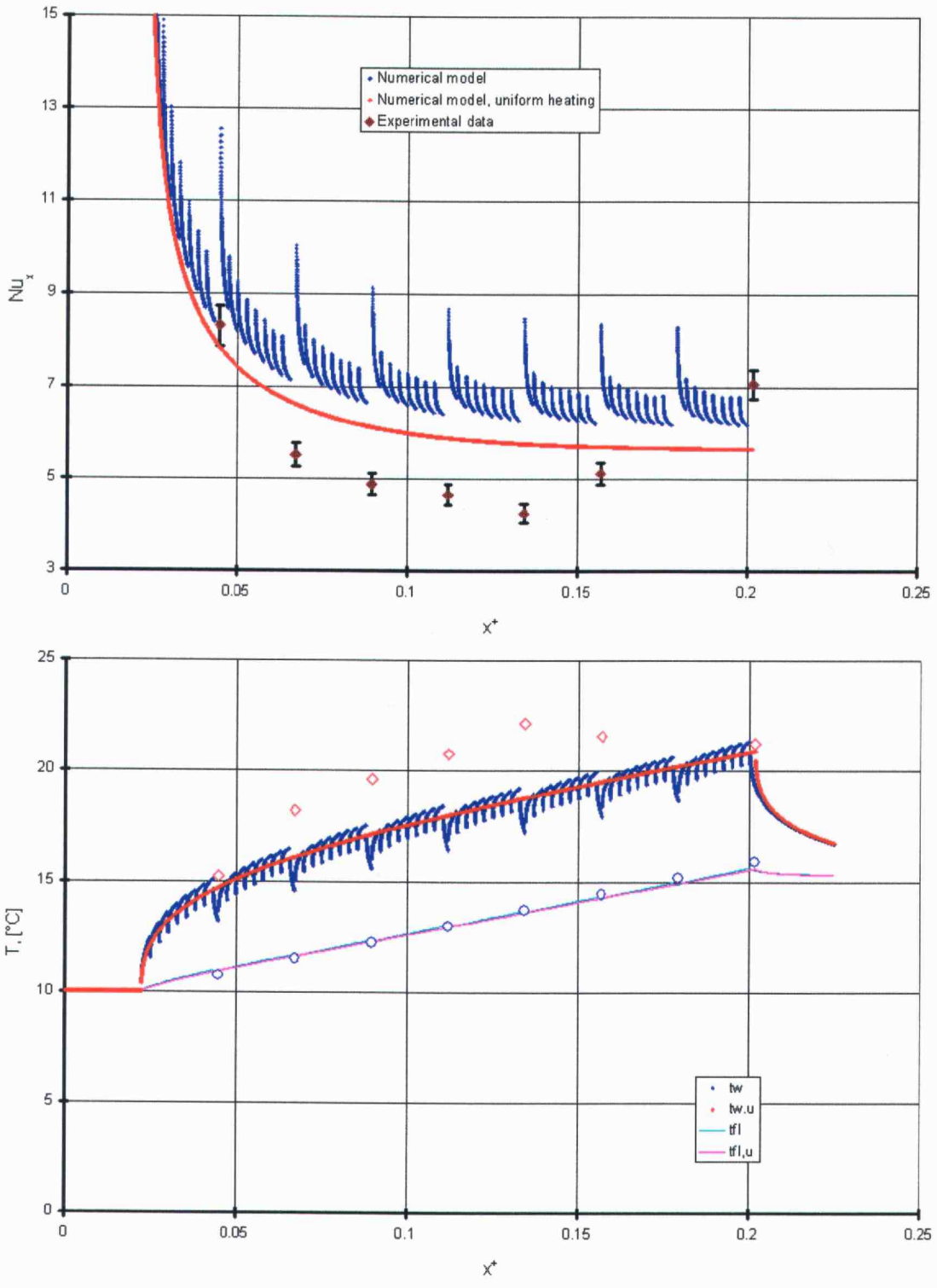

Figure 5.21. Case of 128 μm spacer, 60 ml/min; **top:** variation of local Nusselt number; **bottom:** variation of wall and fluid temperatures

6. CONCLUSIONS

Some studies in microscale fluid flow have reported friction factors that were greater than predictions from classical theory. Wu and Little (1983) measured friction factors in laminar and turbulent flow of gas in rectangular channels etched in silicon or abraded in glass. They found friction factors greater than classical values, though they made their comparison to the Moody chart for flow in round pipes. Pfahler *et al.* (1990a) reported friction factors up to 3 times larger than theoretical predictions, for laminar flow of n-propanol in large aspect ratio channels. A more common result reported in the literature describes measured friction factors in microchannels less than those predicted from classical hydrodynamics. Choi *et al.* (1991) and Yu *et al.* (1995) examined laminar flow of water in microtubes with diameters ranging from 3 μm to 102 μm and found that the friction constant was significantly lower than the classical value. Cuta *et al.* (1996) found friction factors for laminar flow of refrigerant R-124 less than theoretical, but comparison was made to flow in round pipes.

Peng *et al.* (1994a, 1994b) reported friction factors that were less than classical values in some cases, and greater in other cases. These authors examined the flow of water in rectangular channels and found that, only for specific aspect ratios, friction factors were less than classical predictions. Differences between their experimental and theoretical values increased as the dimensions of the channel were reduced.

A few papers reported more radical differences between theory and experiments of laminar flow in microchannels. Pfahler *et al.* (1990b) reported that the friction constant for flow of silicone oil was not constant for developed laminar flow, as predicted by theory (Shah and London, 1978). The authors note, though, that silicone oil is considered a non-Newtonian fluid. A unique result reported by Peng *et al.* (1994a) claims that laminar friction factors for water were proportional to $Re^{-1.98}$.

Although there has been a reasonable amount of work in this area, there is a clear lack of agreement on the magnitude of the friction constant, or values of Reynolds number at which transition to turbulence occurs. There is general agreement, however, that increased relative roughness reduces the critical Reynolds number. The unusual results reported have been attributed to channel size, aspect ratio, geometry, relative roughness, or fluid species. Unfortunately, these studies have left many variables uncontrolled or unmeasured, and thus, no firm conclusion can be reached.

The present work carefully identified and controlled the experimental variables, and experimental measurement errors were minimized. Pressure drops were measured within the channel itself, thus eliminating the need for correction factors for inlet or exit losses, pipes, bends or valves. Pressure variation along the channel was non-linear with distance from the inlet (Figure 4.6). Therefore, pressure drop measurements were made along the middle third of the channel, to exclude entrance and exit effects.

Some previous work has mentioned surface roughness as an important factor that influences fluid flow at microscale, but no accurate measurements were performed. In this work, the top and bottom surfaces of the channel were carefully characterized at several locations along the channel, using high-performance instruments.

The test section layout in this work allowed channel depth measurements *in-situ*. The test section was filled with liquid and pressurized, duplicating experimental conditions, and placed under the microscope. The micrometer stage of the microscope was used to focus on top and bottom surfaces for accurate channel depth measurements. The measurements were performed both across the channel width and down the length of the channel, for a better estimate of the uncertainty in the channel depth.

The test loop used was designed to augment quantitative experimental data with qualitative observations through flow visualization (video-photo-microscopy). Thus, laminar to turbulent transition was detected from both friction factor data analysis and flow visualization experiments. These transition-Reynolds-numbers are much larger than some experimental values of 200 – 900 reported in the literature. The transition distance approaches the classical value as channel depth increases.

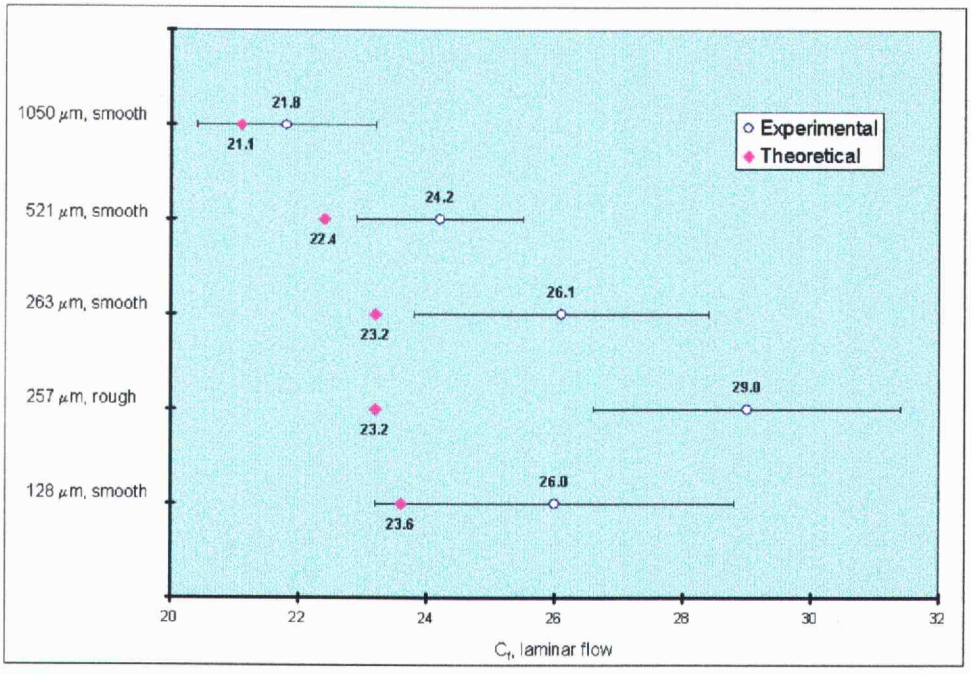

Figure 6.1. Confidence intervals on friction constant in laminar flow

Although each microchannel configuration exhibited significantly higher friction constants than predicted by macroscale laminar flow theory, it is not possible to conclude from these data that channel geometry or relative roughness were related to the higher constants. Overlapping of the confidence intervals precludes conclusions about the importance of these parameters. The range of possible values for $\overline{f \cdot Re}$ in laminar flow for each experiment is plotted in bar graph form in Figure 6.1.

Previous studies on single-phase heat transfer in rectangular microchannels have been focused on specific applications. Multiple channels were often used, with possible ill-distributed flow conditions. Typically, heat has been applied through a metal barrier. Wall temperatures were estimated from one- or two-dimensional conduction calculation. The nature of the wall heating condition was not known, and was modified by conduction in the metal. Channels were often too short to allow fully developed hydrodynamic conditions upstream of the heated surface. Many experiments were performed with water as working fluid, which requires high temperatures.

With few exceptions, measurements have been performed in the turbulent flow regime. It has been suggested that heat transfer tends to be lower than macroscale for $Re < 1000$, and higher for $Re > 1000$ (Peng and Wang, 1993; also, Wu and Little, 1984). At low Reynolds numbers (transition zone), Nusselt numbers were considered explicit functions of inlet velocity and temperature (Wang and Peng, 1994). Turbulent convective heat transfer coefficients have been hypothesized to be strong functions of aspect ratio and hydraulic diameter (Peng *et al.*, 1994). Recent experiments (Adams *et al.*, 1999) measured heat transfer coefficients for turbulent convection in microchannels that were higher than predicted by the standard Dittus-Boelter correlation.

In the present work a test section, specially designed for fundamental measurements in single-phase heat transfer, has been utilized. Heat was applied directly to the fluid, and temperatures at the heated surface were measured directly, without any intervening material. Axial conduction was minimized using an array of smaller heaters. Heat may be applied only in the hydrodynamically developed region, if that is desired.

The numerical model developed allows a wide range of input parameters, given that the stability criterion is satisfied. As an example, even though tests were conducted for flow rates larger than 20 ml/min, it is possible to use the code for lower flow rates to predict asymptotic values for laminar Nusselt number. This was the case for predicting Nusselt numbers for the 521-μm channel, where fully-developed laminar conditions could not be reached in the experiment (Figure 6.2).

Tests were conducted in laminar flow over a range of Re between 300 and 900. Prandtl number varied over the range $Pr = 3.6 - 3.8$. Plotted values for local Nusselt numbers demonstrate good agreement with numerical predictions for the larger channels, within the confidence interval. The minor increase relative to theoretical values may be due to the more realistic situation where fluid properties are temperature dependent. There is a significant decrease, up to 25 percent, in local Nusselt number for the smallest channel studied. Not enough channel sizes were examined to enable a firm conclusion regarding the critical hydraulic diameter at which macroscale theoretical predictions are no longer valid.

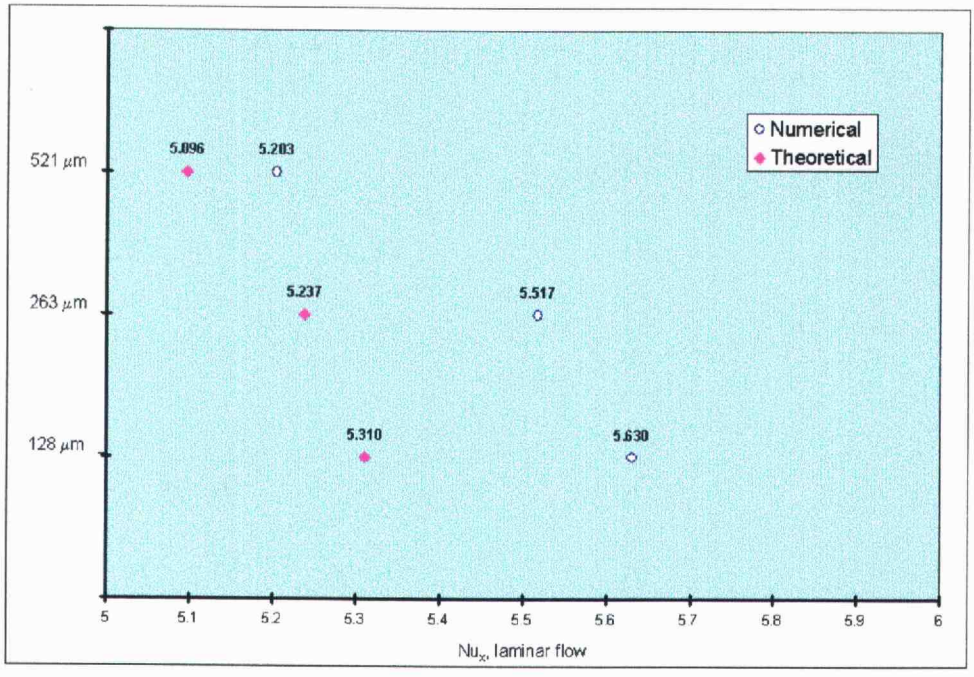

Figure 6.2. Asymptotic values for local Nusselt number, laminar flow

Overall, it can be stated that the heat transfer coefficient increased with reduction in hydraulic diameter.

Future work in this area might include:

- better understanding of flow development and transition in microchannel flow using particle image velocimetry (PIV) methods to study dynamic events during transition
- evaluate the influence of the relative roughness for a larger range of materials and surface characteristics
- document both hydrodynamic and thermal entrance lengths
- measure local heat transfer coefficients in both transitional and turbulent flow.

REFERENCES

Acosta, R. E., Muller, R. H., and Tobias, C. W., 1985, "Transport Processes in Narrow (Capillary) Channels", *AIChE J*, Vol. 31 (3), pp. 473-482.

Adams, T. M., Abdel-Khalik, S. I., Jeter, S. M., and Qureshi, Z. H., 1997, "An Experimental Investigation of Single-Phase Forced Convection in Microchannels", *AIChE Symposium Series – Heat Transfer, Baltimore 1997*, pp. 87-94.

Adams, T. M., Ghiaasiaan, S. M., and Abdel-Khalik, S. I., 1999, "Enhancement of Liquid Forced Convection Heat Transfer in Microchannels Due to the Release of Dissolved Non-condensibles", *International Journal of Heat and Mass Transfer*, Vol. 42, pp. 3563-3573.

Adler, J., 1997, "Three Magic Wands", *Newsweek*, Vol.130 (24-A), pp. 6.

Arpaci, V. S., 1992, "A Thermal Mesomicroscale for Turbulent Forced Convection", in: *Fundamental Issues in Small Scale Heat Transfer* (Edited by Y. Bayazitoglu), ASME HTD - Vol. 227, pp. 69-74.

Bailey, D. K., 1996, "An Apparatus for the Study of Friction and Heat Transfer in Microchannels", M.S. Thesis, Louisiana Tech University, May 1996.

Beskok, A., and Karniadakis, G. M., 1992, "Simulation of Slip-Flow in Complex Micro-Geometries", in: *Micromechanical Systems* (Edited by D. Cho *et al.*), ASME DSC - Vol. 40, pp. 355-370.

Bhatti, M. S., and Savery, C. W., 1977, "Heat Transfer in the Entrance Region of a Straight Channel: Laminar Flow with Uniform Wall Heat Flux", *Transactions of ASME, Journal of Heat Transfer*, Vol. 99, pp. 142-144.

Bhatti, M. S., and Savery, C. W., 1978, "Heat Transfer in the Entrance Region of a Straight Channel: Laminar Flow with Uniform Wall Temperature", *Transactions of ASME, Journal of Heat Transfer*, Vol. 100 (8), pp. 539-542.

Bier, W., Keller, W., Linder, G., and Seidel, D., 1990, "Manufacturing and Testing of Compact Micro Heat Exchangers with Volumetric Heat Transfer Coefficients", in: *Microstructures Sensors, and Actuators* (Edited by D. Cho *et al.*), ASME DSC - Vol. 19, pp. 189-197.

Bowers, M. B., and Mudawar, I., 1994a, "Two-Phase Electronic Cooling using Mini-channel and Micro-channel Heat Sinks - Part 2: Flow Rate and Pressure Drop Constraints", *Transactions of the ASME*, Vol. 116, pp. 298-305.

Bowers, M. B., and Mudawar, I., 1994b, "High Flux Boiling in Low Flow Rate, Low Pressure Drop Mini-channel and Micro-channel Heat Sinks", *International Journal of Heat and Mass Transfer*, Vol. 37 (2), pp. 321-332.

Choi, S. B., Barron, R. F., and Warrington, R. O., 1991, "Fluid Flow and Heat Transfer in Microtubes", in: *Micromechanical Sensors, Actuators and Systems* (Edited by D. Cho *et al.*), ASME DSC - Vol. 32, pp. 123-134.

Clark, S. H., and Kays, W. M., 1953, "Laminar-Flow Forced Convection in Rectangular Tubes", *Transactions of the ASME*, Vol. 75, pp. 859-866.

Cuta, J. M., McDonald, C. E., Shekarriz, A., 1996, "Forced Convection Heat Transfer in Parallel Channel Array Microchannel Heat Exchanger", *Advances in Energy Efficiency, Heat/Mass Transfer Enhancement*, ASME PID - Vol. 2 / HTD - Vol. 338, pp. 17-23.

Cotter, T. P., 1984, "Principles and Prospects of Micro Heat Pipes", *Proceedings of the 5th International Heat Pipes Conference*, Tsukuba, Japan, pp. 325-328.

Dario, P., Carrozza, M. C., Croce, N., Montesi, M. C., and Cocco, M., 1995, "Non-Traditional Technologies for Microfabrication", *Journal of Micromechanics and Microengineering*, Vol. 5 (2), pp. 64-71.

Ehrfeld, W., Bley, P., Götz, F., Hagmann, P., Maner, A., Mohr, J., Moser, H. O., Münchmeyer, D., Schelb, W., Schmidt, D., Becker, E. W., 1987, "Fabrication of Microstructures Using the LIGA Process", reprinted in: *Micromechanics and MEMS*, 1997, (Edited by Trimmer, W. S.), IEEE Press, pp. 623-633.

Flik, M.I., Choi, B.I., Goodson, K.E., 1991, "Heat Transfer Regimes in Microstructures", in: *Micromechanical Sensors, Actuators, and Systems* (Edited by D. Cho *et al.*), ASME DSC - Vol. 32, pp. 31-48.

Flik, M.I., Choi, B.I., Goodson, K.E., 1992, "Heat Transfer Regimes in Microstructures", *Transactions of the ASME, Journal of Heat Transfer*, Vol. 114 (8), pp. 666-674.

Frazier, A. B., Warrington, R. O., Friedrich, C., 1995,"The Miniaturization Technologies: Past, Present, and Future", *IEEE Transactions on Industrial Electronics*, Vol. 42 (5), pp. 423-431.

Gersey, C. O., and Mudawar, I., 1995a, "Effects on Heater Length and Orientation on the Trigger Mechanism for Near-Saturated Flow Boiling CHF - Part I: Photographic and Statistical Characterization of the Near-Wall Interfacial Features", *International Journal of Heat and Mass Transfer*, Vol. 38 (4), pp. 629-642.

Gersey, C. O., and Mudawar, I., 1995a, "Effects on Heater Length and Orientation on the Trigger Mechanism for Near-Saturated Flow Boiling CHF - Part II: CHF Model", *International Journal of Heat and Mass Transfer*, Vol. 38 (4), pp. 643-654.

Goldberg, N., 1984, "Narrow Channel Forced Air Heat Sink", *IEEE Transactions on Components, Hybrids, and Manufacturing Technology*, CHMT-7, pp. 154-159.

Hanemann, R., 1990, "Physical Technology and the Air Cooling and Interconnection Limits for Mini- and Microcomputers", in: *Advances in Thermal Modeling of Electronic Components and Systems* (Edited by Bar-Cohen and Kraus), ASME Press, New York, Vol. 2, pp. 1 – 40.

Harley, J., and Bau, H., 1989, "Fluid Flow in Micron and Submicron Size Channels", *IEEE Transactions*, THO249-3, pp. 25-28.

Harley, J., Pfahler, J., Bau, H., and Zemel, J., 1989, "Transport Processes in Micron and Sub Micron Channels", ASME HTD - Vol. 116, pp. 1-5.

Harley, J. C., Huang, Y., Bau, H. H., and Zemel, J. N., 1995, "Gas Flow in Micro-Channels," *Journal of Fluid Mechanics*, Vol. 284, pp. 247-274.

Harms, T. M., Kazmierczak, M., and Gerner, F. M., 1997, "Experimental Investigations of Heat Transfer and Pressure Drop Through Deep Microchannels in a (110) Silicon Substrate", in: *Proceedings of the ASME Heat Transfer Division*, ASME HTD - Vol. 351, pp. 347-357.

Hartnett, J. P., and Kostic, M., 1989, "Heat Transfer to Newtonian and Non-Newtonian Fluids in Rectangular Ducts", *Advances in Heat Transfer*, Vol. 19, pp. 247-356.

Hoopman, T. L., 1990, "Microchanneled Structures", *Microstructures Sensors, and Actuators* (Edited by D. Cho *et al*), ASME DSC - Vol. 19, pp. 171-174.

Hwang, L. T., Turlik, I., Reisman, A., 1987, "A Thermal Module for Advanced Packaging", *Journal of Electronic Materials*, Vol. 16(5), pp. 347-355.

Joo, Y., Dieu, K., and Kim, C. J., 1995, "Fabrication of Monolithic Microchannels for IC Chip Cooling," *IEEE Micro Electro Mechanical Systems Workshop*, Amsterdam, The Netherlands, Jan.-Feb. 1995.

Kaminsky, G., 1985, "Micromachining of Silicon Mechanical Structures", *Journal of Vacuum Science Technology*, Vol. B3 (4), pp. 1015-1024.

Kawano, K., Minakami, K., Iwasaki, H., and Ishizuka, M., 1998, "Micro Channel Heat Exchanger for Cooling Electrical Equipment", *Proceedings of the ASME Heat Transfer Division*, ASME HTD, Vol. 361-3 / ASME PID - Vol. 3, pp. 173-180.

Kays, W. M., 1966, "Convective Heat and Mass Transfer", McGraw-Hill, New York.

Kays, W. M., and Crawford, M. E., 1993, "Convective Heat and Mass Transfer', 3rd Ed., McGraw-Hill, New York.

Kishimoto, T., and Ohsaki, T., 1986, "VLSI Packaging Technique using Liquid-Cooled Channels", *IEEE Transactions on Components, Hybrids, and Manufacturing Technology*, Vol. 9, pp. 328-335.

Maddox, D.E., and Mudawar, I., 1989, "Single and Two-Phase Convective Heat Transfer from Smooth and Enhanced Microelectronic Heat Sources in a Rectangular Channel", *Transactions of the ASME, Journal of Heat Transfer*, Vol. 111 (11), pp. 1045-1052.

Mahalingham, M., 1985, "Thermal management in semiconductor device packaging", *IEEE Proceedings*, Vol. 73, pp. 1396-1404.

Marco S. M., and Han, L. S., 1955, "A Note on Limiting Laminar Nusselt Number in Ducts with Constant Temperature Gradient by Analogy to Thin-Plate Theory", *Transactions of the ASME*, Vol. 77, 625-630.

Missaggia, L. J., Walpole, J. N., Liau, Z. L., and Phillips, R. J., 1989, "Microchannel Heat Sinks for Two-Dimensional High-Power-Density Diode Laser Array", *IEEE Journal of Quantum Electronics*, Vol. 25(9), pp. 1988-1992.

Nayak, D., Hwang, L. T., Turlik, I., Reisman, A., 1987, "A High-Performance Thermal Module for Computer Packaging", *Journal of Electronic Materials*, Vol. 16(5), pp. 357-364.

Osborne, D. G., and Incropera, F. P., 1985, "Laminar, Mixed Convection Heat Transfer for Flow Between Horizontal Parallel Plates with Asymmetric Heating", *International Journal of Heat and Mass Transfer*, Vol. 28(1), pp. 207-217.

Papautsky, I., Brazzle, J., Ameel, T. A., and Frazier, A. B., 1998a, "Microchannel Fluid Behavior Using Micropolar Fluid Theory", IEEE#-98CH36176, Proceedings of the IEEE 11th Annual International Workshop on MEMS, 544-549.

Papautsky, I., Brazzle, J., Swerdlow, H., and Frazier, A. B., 1998b, "A Low-Temperature IC-Compatible Process for Fabricating Surface-Micro-Machined Metallic Micro-channels", *IEEE Journal of Microelectromechanical Systems*, Vol. 7 (2), 267-273.

Peng, X. F., and Peterson, G. P., 1995, "The Effect of Thermofluid and Geometrical Parameters on Convection of Liquid Flowing Through Rectangular Microchannels", *International Journal of Heat and Mass Transfer*, Vol. 38 (4), pp. 755-758.

Peng, X. F., and Peterson, G. P., 1996a, "Convective Heat Transfer and Flow Friction for Water Flow in Microchannel Structures", *International Journal of Heat and Mass Transfer*, Vol. 39 (12), pp. 2599-2608.

Peng, X. F., and Peterson, G. P., 1996b, "Forced Convection Heat Transfer of Single-Phase Binary Mixtures Through Microchannels", *Experimental Thermal and Fluid Science (International Journal of Experimental Heat Transfer, Thermodynamics, and Fluid Mechanics)*, Vol. 12 (1), pp. 98-104.

Peng, X. F., Peterson, G. P., and Wang, B. X., 1994a, "Frictional Flow Characteristics of Water Flowing Through Rectangular Microchannels", *Experimental Heat Transfer*, Vol. 7, pp. 249-264.

Peng, X. F., Peterson, G. P., and Wang, B. X., 1994b, "Heat Transfer Characteristics of Water Flowing through Microchannels", *Experimental Heat Transfer*, Vol.7, pp. 265-283

Peng, X. F., and Wang, B. X., 1993, "Forced Convection and Flow Boiling Heat Transfer for Liquid Flowing Through Microchannels", *International Journal of Heat and Mass Transfer*, Vol. 36 (14), pp. 3421-3427.

Peng, X. F., Wang, B. X., Peterson, G. P., and Ma, 1995, "Experimental Investigation of Heat Transfer in Flat Plates With Rectangular Microchannels", *International Journal of Heat and Mass Transfer*, Vol. 38 (1), 127-137

Peterson, G. P., Duncan, A. B., Ahmed, A. S., Mallik, A. K., and Weichold, M. H., 1991, "Experimental Investigation of Micro Heat Pipes in Silicon Wafers", in: *Micromechanical Sensors, Actuators, and Systems* (Edited by D. Cho *et al.*), ASME DSC - Vol. 32, pp. 341-348.

Pfahler, J., Harley, J., Bau, H., and Zemel, J., 1990a, "Liquid Transport in Micron And Sub-micron Channels", *Journal of Sensors and Actuators*, A21 - A23, pp. 431-434.

Pfahler, J., Harley, J., Bau, H. H., and Zemel, J., 1990b, "Liquid and Gas Transport in Small Channels", in: *Microstructures, Sensors, and Actuators* (Edited by D. Cho *et al.*), ASME DSC - Vol. 19, pp. 149-157.

Pfahler, J., Harley, J., Bau, H. H., and Zemel, J. N., 1991, "Gas and Liquid Flow in Small Channels", in: *Micromechanical Sensors, Actuators and Systems* (Edited by D. Cho *et al.*), ASME DSC - Vol. 32, pp. 49-60.

Pfund, D. M., Shekarriz, A., Popescu, A., and Welty, J. R., 1998, "Pressure Drop Measurements in a Microchannel", in: *Micro-Electro-Mechanical Systems (MEMS)*, ASME DSC - Vol. 66, 193-198.

Phillips, R. J., 1990, "Microchannel Heat Sinks", in: *Advances in Thermal Modeling of Electronic Components and Systems* (Edited by Bar-Cohen and Kraus), ASME Press, Vol. 2, pp. 109-185.

Rujano, J. R., Rahman, M. M., 1995, "Analysis and Computation of Conjugate Heat Transfer in Trapezoidal Microchannel Heat Sinks in a Silicone Substrate", *Proceedings of the 30th National Heat Transfer Conference*, ASME HTD - Vol. 305 (3), pp. 175-185.

Schmidt, F. W., and Newell, M. E., 1967, "Heat Transfer in Fully Developed Laminar Flow Through Rectangular and Isosceles Triangular Ducts", *International Journal of Heat and Mass Transfer*, Vol. 10, pp. 1121-1123.

Service, R. F., 1996, "Can Chip Devices Keep Shrinking? ", *Science*, Vol. 274(5294 – Dec.), pp.1834-1836.

Shah, R. K., and London, A. L., 1978, "Laminar Flow Forced Convection in Ducts", *Advances in Heat Transfer* (Edited by Irvine, T. F. and Hartnett, J. P), Academic Press, Suppl. 1, pp. 178-193.

Shih, J. C., Ho, C.-M., Liu, J., Tai, Y.-C., 1996, "Monoatomic and Polyatomic Gas Flow Through Uniform Microchannels", in: *Micro-Electro-Mechanical Systems (MEMS)* (Edited by C.-J. Kim *et al.*), ASME DSC - Vol. 59, pp. 197-203.

Sparrow, E. M., Patankar, S. V., 1977, "Relationship Among Boundary Conditions and Nusselt Numbers for Thermally Developed Duct Flows", *Transactions of the ASME, Journal of Heat Transfer*, Vol. 99 (8), pp. 483-485.

Sparrow, E. M., Baliga, B. R., Patankar, S. V., 1978, "Forced Convection Heat Transfer from a Shrouded Fin Array With and Without Tip Clearance", *Transactions of the ASME, Journal of Heat Transfer*, Vol. 100 (11), pp. 572-579.

Sturgis, C. J., and Mudawar, I., 1999a, "Critical Heat Flux in a Long, Rectangular Channel Subjected to One-Side Heating - I. Flow Visualization", *International Journal of Heat and Mass Transfer*, Vol. 42 (10), pp. 1835-1847.

Sturgis, C. J., and Mudawar, I., 1999b, "Critical Heat Flux in a Long, Rectangular Channel Subjected to One-Side Heating - II. Analysis of Critical Heat Flux Data", *International Journal of Heat and Mass Transfer*, Vol. 42 (10), pp. 1849-1862.

Tuckerman, D. B., and Pease, R. F. W., 1981a, "High Performance Heat Sinking For VLSI", *IEEE Electron Device Letters*, Vol. EDL-2 (5), pp. 126-129.

Tuckerman, D. B., and Pease, R. F. W., 1981b, "Errata to High Performance Heat Sinking For VLSI", *IEEE Electron Device Letters*, Vol. EDL-2 (8), pp. 213.

Tuckerman, D. B., and Pease, R. F. W., 1982, "Optimized Convection Cooling Using Micromachined Structures", *Journal of the Electrochemical Society*, Vol. 129 (3), pp. C98 (125).

Urbanek, W., Zemel, J., and Bau, H. H., 1993, "An Investigation on the Temperature Dependence of Poiseuille Numbers in Microchannel Flow", Journal of Micromechanics and Microengineering, Vol. 3, pp. 206-208.

van der Schoot, B. H., 1995, "Interfacing Micro and Macro Mechanical Worlds", *Journal of Micromechanics and Microengineering*, Vol. 5 (2), pp. 72-73.

Wang, B. X., and Peng, X. F., 1994, "Experimental Investigation of Liquid Forced Convection Heat Transfer Through Microchannels", *International Journal of Heat and Mass Transfer*, Vol. 37 (Suppl. 1), pp. 73-82.

Wang, J. H., Yeh, H. Y., and Shyu, R. J., 1991, "Thermal-Hydraulic Characteristic of Micro Heat Exchangers", *Micromechanical Sensors, Actuators, and Systems* (Edited by D. Cho *et al.*), ASME DSC - Vol. 32, pp. 331-339.

Webb, R. L., and Zhang, M., 1998, "Heat Transfer and Friction in Small Diameter Channels", *Microscale Thermophysical Engineering*, Vol. 2, pp. 189-202.

Wegeng, R. S., Drost, M. K., Ameel, T. A., and Warrington, R.O., 1995, "Energy System Miniaturization Technologies, Devices, and Systems", *Proceedings of the International Symposium on Advanced Energy Conversion Systems and Related Technologies,* RAN'95, The Society of Chemical Engineers, Nagoya, Japan, December 1995, pp.607-614.

Weisberg, A., Bau, H. H., and Zemel, J., 1990, "Micro-Heat Exchangers", in: *Microstructures Sensors, and Actuators* (Edited by D. Cho *et al.*), ASME DSC - Vol. 19, pp. 159-170.

Weisberg, A., Bau, H. H., and Zemel, J., 1992, "Analysis of microchannels for integrated cooling", *International Journal of Heat and Mass Transfer*, Vol. 35 (10), pp. 2465-2474.

Welty, J. R., Wicks, C. E., and Wilson, R. E., 1984, "Fundamentals of Momentum, Heat, and Mass transfer", 2nd Edition, John Wiley and Sons, New York.

Wise, K. D., 1991, "Micromechanical Sensors, Actuators, and Systems", in: *Micromechanical Sensors, Actuators, and Systems* (edited by D. Cho *et al.*), ASME DSC - Vol. 32, pp. 1-14.

Wu, P. Y., and Little, W. A., 1983, "Measurement of Friction Factor for the Flow of Gases in Very Fine Channels Used for Microminiature Joule-Thompson Refrigerators", *Cryogenics*, Vol. 23 (5), pp. 273-277.

Wu, P. Y., and Little, W. A., 1984, "Measurement of the Heat Transfer Characteristics of Gas Flow in Fine Channels Heat Exchangers Used for Microminiature Refrigerators", *Cryogenics*, Vol. 24 (8), pp. 415-420.

Yu, D., Warrington, R. O., Barron, R. F., and Ameel, T., 1995, "An Experimental and Theoretical Investigation of Fluid Flow and Heat Transfer in Microtubes", *Proceedings of the ASME/JSME Thermal Engineering joint Conference*, Vol. 1, pp. 523-530.

APPENDICES

APPENDIX A. TECHNICAL DATA AND CALIBRATION

A.1 Data Acquisition (DAQ) System

There is a built-in ADC with 12- or 16-bit resolution on the analog cards that resolves 1 count out of 2^{12} or 2^{16}, respectively. Resolution of ADC is 1/4096 (0.024%) or 1/65,536 (0.006%). One ACPC-16-16 and two ACPC-12-16 cards are used, with two terminal panels T21 for each card. Software selectable resolution is from 12 to 16 bits (ACPC-16) or from 9 to 12 bits (ACPC-12). Each card has sixteen differential analog inputs and sixteen digital inputs/outputs lines (ACPC-16-16 or ACPC-12-16). The acquisition speed varies from 10 – 2.5 kHz for ACPC-12 to 2.5 – 0.225 kHz at ACPC-16. On any terminal, maximum voltage is 150 V and maximum current is 1 A. Specified operating ambient temperature is 0 – 50°C, and RH is 0 – 90%, non-condensing.

ACPC uses a unique technique for high stability that requires no adjustments for years. Instead of using potentiometers to calibrate the card, the adjustment is entered in software, analog inputs being automatically recalibrated during the normal operation. The calibration numbers must be entered in the program in the setup mode, starting with the serial number for the analog card and then ACAL, BCAL, and DCAL. Then serial number and CCAL for the terminal panels are entered (Table A.1).

Table A.1. The calibration numbers used for DAQ setup

		ACPC - 16 - 16	ACPC - 12 - 16	ACPC - 12 - 16
		1	2	3
Card	S/N	15066	21601	22093
	ACAL	23686	23409	23583
	BCAL	29096	28849	29071
	DCAL	21620	21470	21631
Terminal Panel 1	S/N	15066	21601	22093
	CCAL	22975	22691	22910
Terminal Panel 2	S/N	15067	21602	22094
	CCAL	23150	22940	22886

A.2 Pressure transducers

The pressure sensors consist of a bridge of pressure sensitive resistors. Test loop configuration used a field selectable isolated strain gauge (bridge) to DC transmitter.

The ENDEVCO Model 8510C is a rugged, miniature, high resonance, high sensitivity piezoresistive pressure transducer, ideal for measuring dynamic pressure. It has a 10-32 mounting thread and 3.8 mm (0.15-inch) face diameter.

The pressure transducer features a four-arm strain gage bridge ion implanted into a unique-sculptured-silicon diaphragm for maximum sensitivity and wide band frequency response. Self-contained hybrid temperature compensation provides stable performance over the temperature range of -18°C to +93°C (0°F to 200°F). Also features excellent linearity (even to 3X range), high shock resistance, and high stability during temperature transients. Its vent tube may be connected to a standard reference manifold or used for differential pressure measurement. Table A.2 presents the general specifications supplied by manufacturer.

Table A.2. General specifications for ENDEVCO pressure transducers

Full Scale output (FSO)	225 mV typical (140 mV Min) at 10.0 Vdc
Supply Voltage	10 Vdc recommended, 15 V dc maximum
Electrical Configuration	Active four-arm piezoresistive bridge

	Units	**Model - 50**	**Model - 100**
RANGE	psig	0 - 50	0 - 100
POSITIVE SENSITIVITY	mV/psi (min)	4.5 (2.8)	2.25 (1.4)
ZERO MEASURAND OUTPUT	mV (max)	±20	±20
THERMAL ZERO SHIFT (-18°C to +93°C)	±% FSO (max)	3	3
THERMAL TRANSIENT RESPONSE	psi/°F	0.003	0.01
	psi/°C	0.005	0.02
WARM UP TIME	ms	1	1
BURST PRESSURE (Diaphragm/Reference Side)	psi (min)	250/300	400/300

The pressure sensors calibration (Figure A.1) was performed with transducers mounted in the test section pressurized with water. Transducer cases were properly grounded. Maximum pressure was 50 psig, as one of the transducers cannot be used over this pressure. Calibration standard was Standard Lab no. 535–31–04–044, using a HEISE H38591, 0 - 100 psi gage.

Transducer ENDEVCO 8510C – 100 (S/N 10540) used bridge transmitter model API 4058 G (S/N E 279 192) and box 1 of the terminal panel (T21) for the ACPC-12-16 DAQ Card (S/N 22093). Transducer sensitivity is 1.85 mV/psi, and excitation is 10 VDC. The bridge, made by Absolute Process Instruments, Inc., is a field selectable isolated strain gauge to DC transmitter, with standard power of 115VAC. The other pressure transducer, ENDEVCO 8510C – 50 (S/N 10001), used a similar bridge transmitter (model API 4058 G, S/N E 214 024), and the same terminal panel box and DAQ card. Transducer sensitivity is 4.13 mV/psi, and the excitation is 10 VDC.

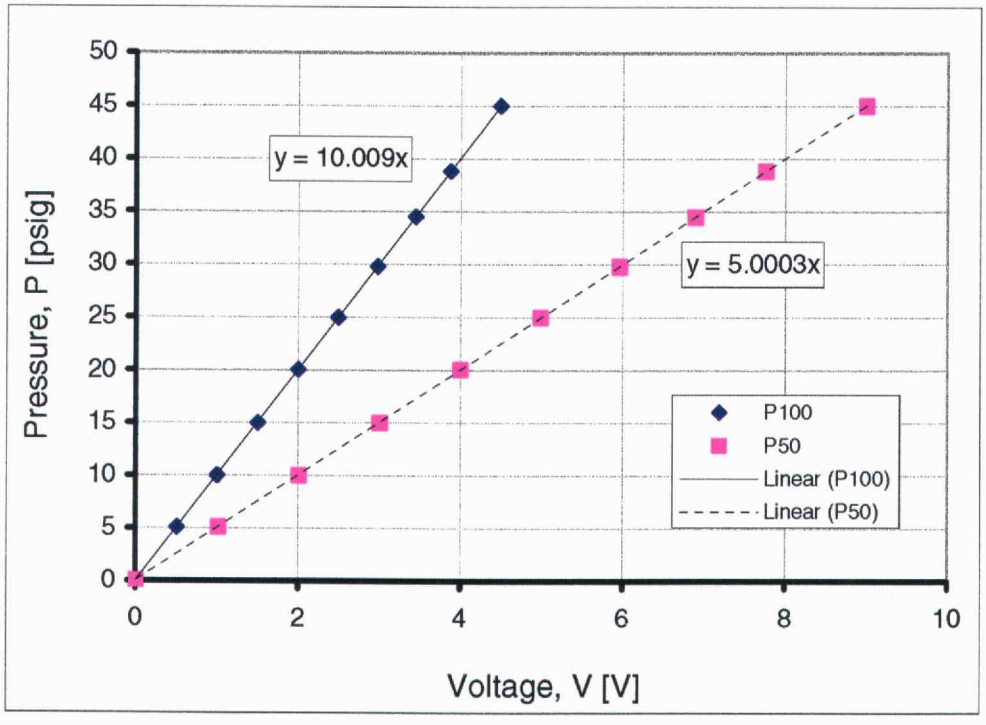

Figure A.1. Calibration curves for the piezoresistive pressure transducers

A.3 Flow meters

Turbine flow meters models 102-3P (13 – 100 ml/min of water) and 102-6P (60 – 1000 ml/min of water) were supplied by McMillan Company with NIST-traceable calibration and have a specified accuracy of 1% of full scale. The standard calibration (NIST 822/249862) used ambient pressure of 760 mm Hg, ambient temperature of 23 °C, and liquid of 23°C temperature. The Flo-Sensor uses a Pelton type turbine wheel and electro-optical detection to convert flow rates into a linear 0 to 5 VDC signal.

The "end-to-end" calibration of the meters (Figure A.2 and Figure A.3) was checked by flowing water into beakers placed on a balance, and comparing the totaled readings with the collected volume, at 12 – 13 points for each meter. The uncertainty in calibration curve for the model 102-3P was ± 0.2 ml/min (at the 95% confidence level), and for the 102-6P model was ± 3.2 ml/min. The uncertainty in individual measurements was ± 0.6 ml/min for the model 102-3P, and ± 11.5 ml/min for the model 102-6P. The water temperature measured with a hand-held thermocouple probe showed variation over a narrow range between 21°C and 24°C.

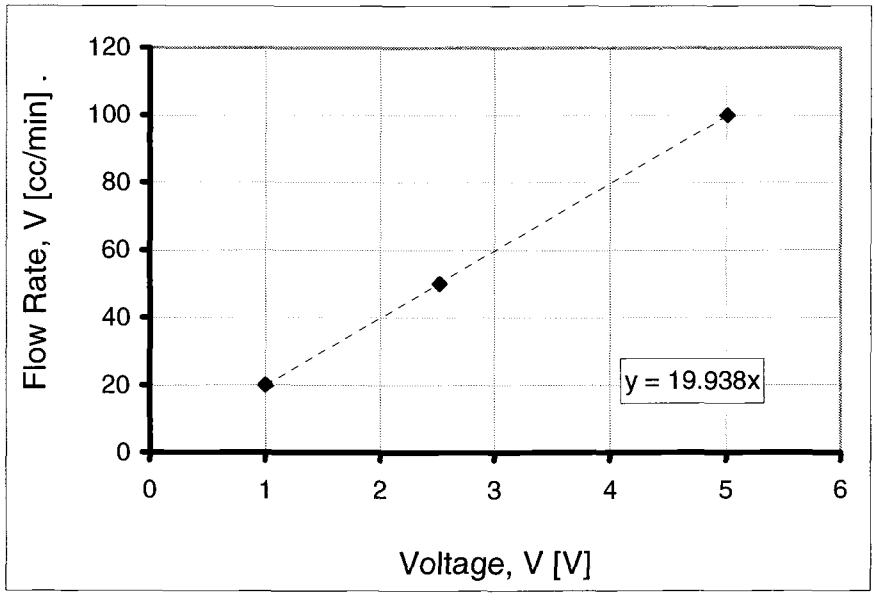

Figure A.2. Calibration curve for the flow meter model 102-3P S/N 1627

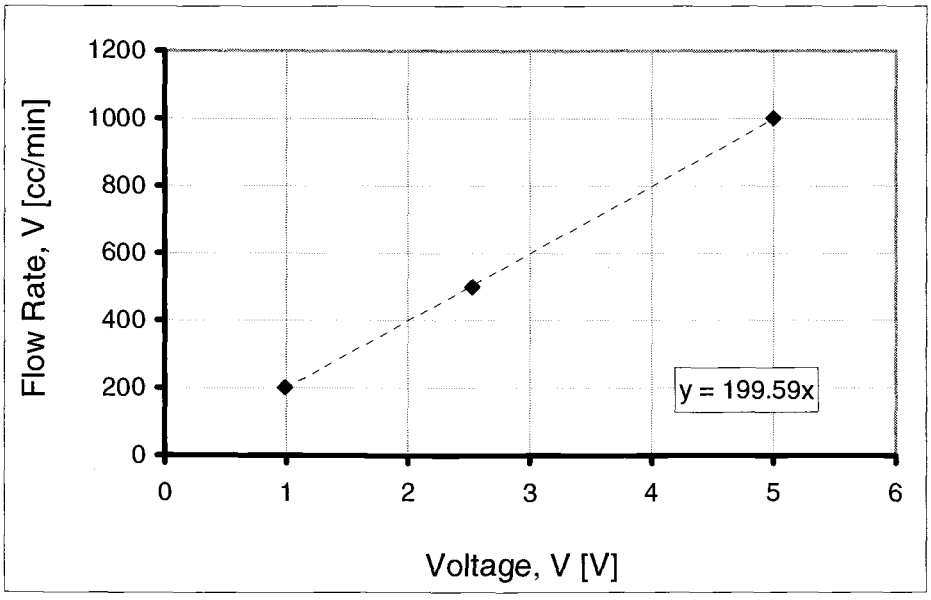

Figure A.3. Calibration curve for the flow meter model 102-6P S/N 1628

A.4 Ball valves and metering valves

The flow through the test loop is controlled with a number of 2-way, WHITEY ball valves, of type SS-43ES4, and 1/4 SWAGELOK connections. The codification is 316 Stainless Steel, Whitey's "40" Series, 4.8 mm orifice, 3000 psig (43), and 2-way, spring-loaded valve with UHMW Polyethylene seat packing (ES4). The unique top-loaded capsule packing allows reliable switching in the most compact design. Technical specifications, as presented by manufacturer, are

- pressure rating: 207 bar at 38°C (3000 psig at 100°F)
- flow data: pressure drop to atmosphere for water at 21°C is 7.5 psi for 10 gpm, 17 psi for 50 gpm and 24 psi for 100 gpm.

The flow rates are controlled with needle valves. The NUPRO Type "M" Series SS-4MG-EPMH is made of 316 Stainless Steel, with straight, 1/4 SWAGELOK connection, ethylene propylene material for O-ring, and factory-assembled vernier handle. The maximum working pressure at 21°C is 68 bar and the maximum flow

coefficient is $C_v = 0.03$. The orifice diameter is 1.42 mm. The calibrated nylon handle for repeatable flow adjustments can be read to $1/25^{th}$ of a turn (1/1000 of an inch). Flow data are as follows: pressure drop to atmosphere for water (21°C) is 1 psi for 0.03 gpm, 10 psi for 0.095 gpm and 100 psi for 0.3 gpm.

The NUPRO Type "M" Series SS-SS4-EPVH has the same characteristics, but the maximum working pressure at 21°C is 137 bar, while the maximum flow coefficient is $C_v = 0.004$. The orifice diameter is 0.81 mm. The pressure drop to atmosphere for water at 21°C is 1 psi for 0.004 gpm, 10 psi for 0.013 gpm and 100 psi for 0.04 gpm.

A.5 Surface characteristics of top and bottom plates

Mean amplitude of roughness on the polycarbonate top plate was ± 0.16 μm, with a maximum peak-valley height of 2.35 μm. Top plate was covered with approximately 0.5-μm deep scratches that were parallel to the flow axis. The scratches were spaced across the channel width at roughly 25 – 45 μm intervals.

Roughness on the smooth polyamide bottom plate consisted of irregular patches. Mean amplitude of the roughness was ± 0.09 μm, with a maximum height (peak-valley) of 2.99 μm.

The surface of rough polyamide was covered with a crosshatch of scratches resulted from been sanded with emery cloth (LP2 FINE grade). The scratches were roughly 3 μm deep, spaced 100 – 400 μm apart. The mean amplitude of roughness on the rough polyamide bottom plate was ±1.90 μm, with a maximum peak-valley height of approximately 14.67 μm.

Figures A.4 and A.5 present samples of the output of the ZIGO profilometer, for measurements performed to characterize the heater plate surface, while Figure A.6 presents measurements for the top plate.

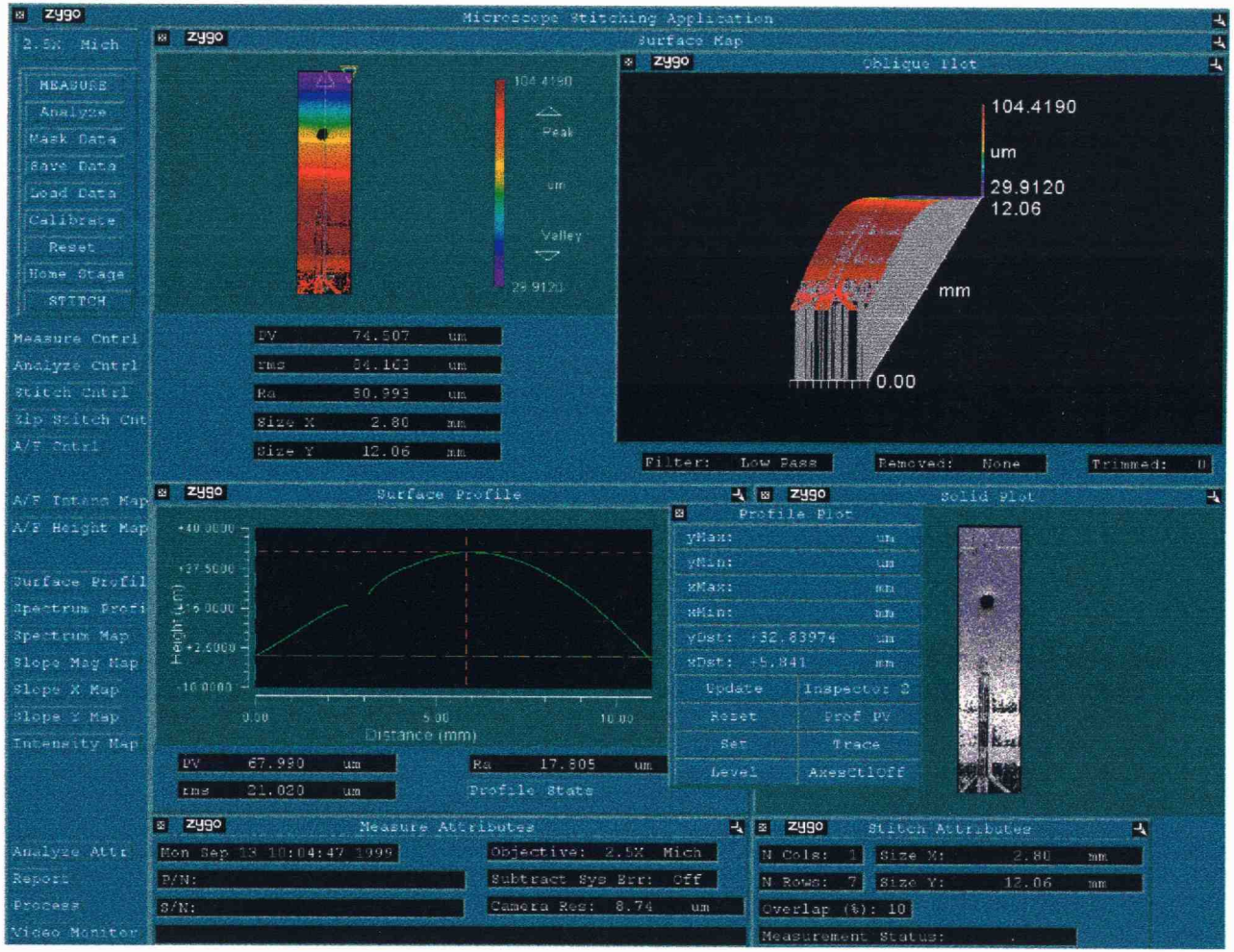

Figure A.4. Screen output of the ZIGO profilometer: surface characteristics across the channel

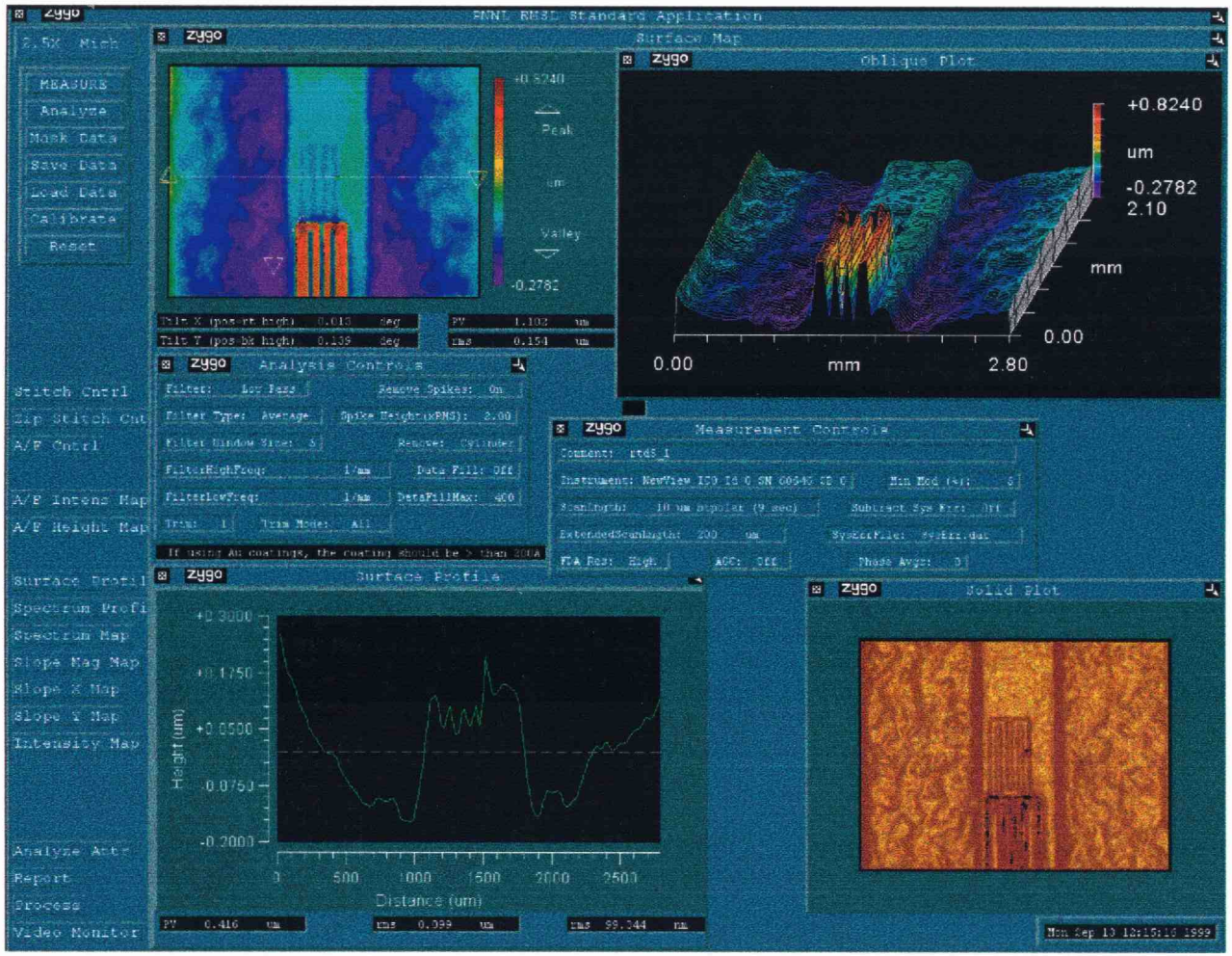

Figure A.5. Screen output of the ZIGO profilometer: surface characteristics across RTD#5

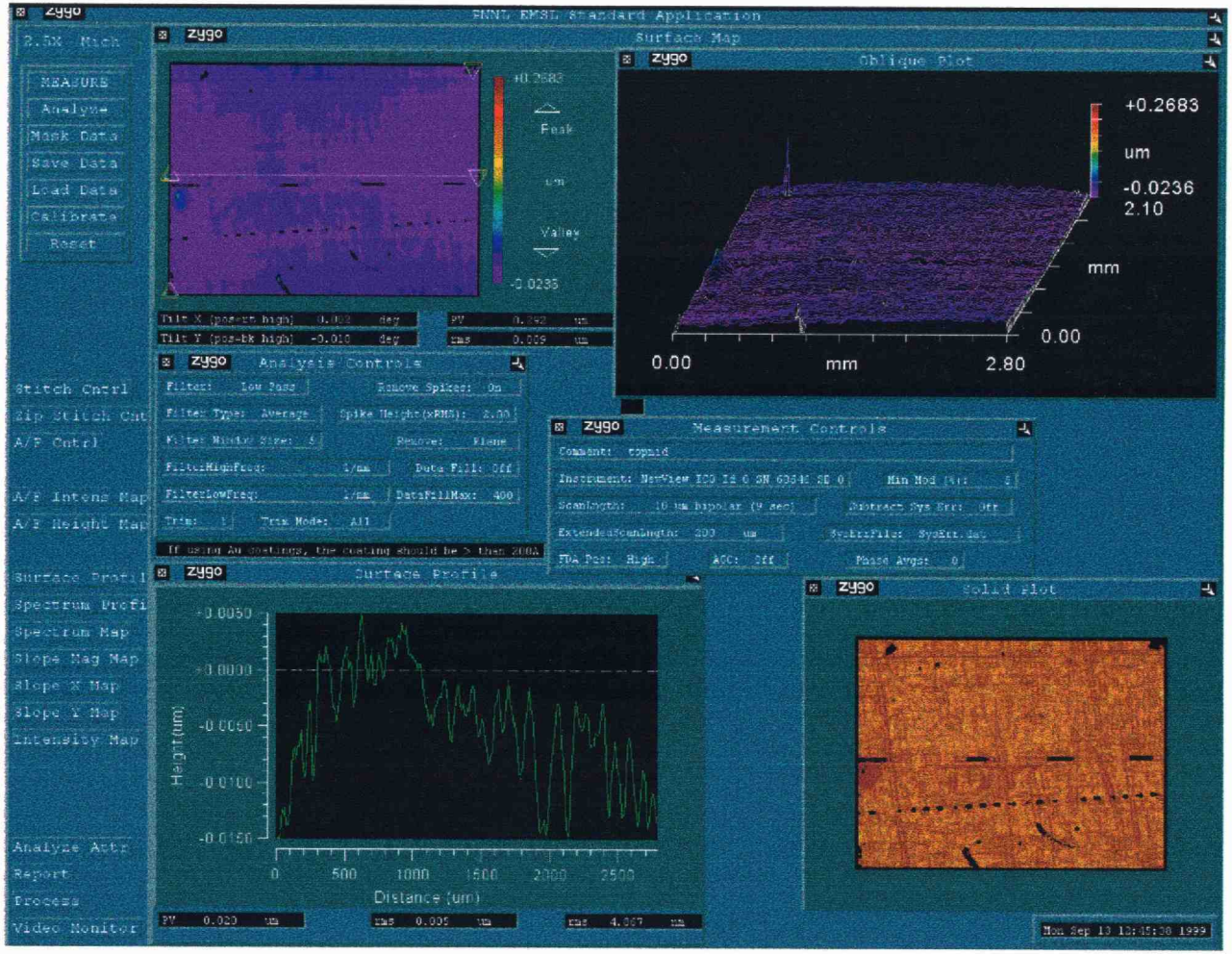

Figure A.6. Screen output of the ZIGO profilometer: surface characteristics of the top plate

APPENDIX B. UNCERTAINTY

B.1 Background

A short review of statistics and uncertainty will be presented to ease the understanding of the method used to compute uncertainties throughout this work.

The arithmetic mean of a sample of n measurements $y_1, y_2, \ldots, y_n$, is

$$\bar{y} = \frac{\sum_{i=1}^{n} y_i}{n} \tag{B.1}$$

The variance of a sample of n measurements $y_1, y_2, \ldots, y_n$, is defined to be

$$s^2 = \frac{\sum_{i=1}^{n} (y_i - \bar{y})^2}{n-1} = \frac{\sum_{i=1}^{n} y_i^2 - \frac{\left(\sum_{i=1}^{n} y_i\right)^2}{n}}{n-1} \tag{B.2}$$

The standard deviation of a sample of n measurements $y_1, y_2, \ldots, y_n$, is equal to the square root of the variance

$$s = \sqrt{s^2} = \sqrt{\frac{\sum_{i=1}^{n} (y_i - \bar{y})^2}{n-1}} \tag{B.3}$$

For a discrete random variable with probability distribution $p_{(y)}$, the expected value (mean) is defined as

$$\mu = E(y) = \sum_{\text{all } y} y \cdot p_{(y)} \tag{B.4}$$

whereas for a continuous random variable with density function $f_{(y)}$, the mean is

$$\mu = E(y) = \int_{-\infty}^{\infty} y \cdot p_{(y)} dy \tag{B.5}$$

$$\sigma^2 = E\left[(y-\mu)^2\right] = \sum_{\text{all } y}(y-\mu)^2 \cdot p_{(y)} = E(y^2) - \mu^2 \tag{B.6}$$

$$\sigma = \sqrt{\sigma^2} \tag{B.7}$$

For both types of variables, variance and standard deviation are defined by equations (B.6) and (B.7), respectively.

An empirical rule, based on the practical experience of researchers, describes a data set with normal distribution as

- approximately 68% of the measurements will lie within 1 standard deviation of their mean, i.e., within the interval $\bar{y} \pm s$
- approximately 95% of the measurements will lie within 2 standard deviations of their mean, i.e., within the interval $\bar{y} \pm 2 \cdot s$
- almost all the measurements will lie within 3 standard deviations of their mean, i.e., within the interval $\bar{y} \pm 3 \cdot s$

The standard error of a statistic is the standard deviation of its sampling distribution. A $(1-\alpha)\cdot 100\%$ confidence interval for the mean value of y for a particular value of x, $x = x_p$, is defined as

$$CI = \pm t_{\alpha/2} \cdot s \cdot \sqrt{\frac{1}{n} + \frac{(x_p - \bar{x})^2}{\sum_{i=1}^{n}(x_i - \bar{x})^2}} \tag{B.8}$$

where $t_{\alpha/2}$ is the student t distribution, and its value is determined as a function of the degrees of freedom $\nu = (n-1)$. Setting the confidence interval at 95%, then $\alpha = 0.05$. When population sample is large, the number of degrees of freedom $\nu \to \infty$, and $t_{0.025} = 1.96$. For sufficiently large n, the sampling distribution of the sample mean is approximately normal, and the following equalities hold true:

$$E(\bar{y})=\mu \quad \Rightarrow \quad \sigma_{\bar{y}}^2=\frac{\sigma^2}{n} \quad \Rightarrow \quad \sigma_{\bar{y}}=\frac{\sigma}{\sqrt{n}}$$

For a normal distribution, the area under the curve between $\mu-1.96\cdot\sigma_{\bar{y}}$ and $\mu+1.96\cdot\sigma_{\bar{y}}$ is 0.95. Thus, with probability 0.95 we expect the value of $\bar{y}$ to fall within 1.96 standard errors of μ. However, the value of σ, the population standard deviation, is usually unknown. When n is large, we can approximate its value with s, the standard deviation of the sample.

Having established the uncertainties for the measured variables, the uncertainty of the final result can be computed with the Kline-McClintock equation:

$$\omega_R=\left[\left(\frac{\partial R}{\partial x_1}\omega_{x_1}\right)^2+\left(\frac{\partial R}{\partial x_2}\omega_{x_2}\right)^2+\left(\frac{\partial R}{\partial x_3}\omega_{x_3}\right)^2+\ldots+\left(\frac{\partial R}{\partial x_n}\omega_{x_n}\right)^2\right]^{\frac{1}{2}} \tag{B.9}$$

where R is the result determined through a functional relationship between the independent variables $x_1, x_2, x_3, \ldots, x_n$, and $\omega_R, \omega_{x_1}, \omega_{x_2}, \omega_{x_3}, \ldots, \omega_{x_n}$ are uncertainties in $R, x_1, x_2, x_3, \ldots, x_n$, respectively (Kline and McClintock, 1953). The non-dimensional form of this equation is

$$\frac{\omega_R}{R}=\left[\left(\frac{\partial R}{\partial x_1}\frac{\omega_{x_1}}{R}\right)^2+\left(\frac{\partial R}{\partial x_2}\frac{\omega_{x_2}}{R}\right)^2+\left(\frac{\partial R}{\partial x_3}\frac{\omega_{x_3}}{R}\right)^2+\ldots+\left(\frac{\partial R}{\partial x_n}\frac{\omega_{x_n}}{R}\right)^2\right]^{\frac{1}{2}} \tag{B.10}$$

B.2 Fluid flow measurements

In fluid flow data analysis, there are uncertainty levels associated with measuring pressure drops, flow rates, channel dimensions, and fluid properties.

$$Re_{D_h}=\frac{\rho\cdot u_m\cdot D_h}{\mu}=\frac{\rho\cdot\dot{V}\cdot\left(4\cdot A/P\right)}{\mu\cdot A}=\frac{4\cdot\rho\cdot\dot{V}\cdot}{\mu\cdot P}=\frac{2\cdot\rho\cdot\dot{V}\cdot}{\mu\cdot(H+W)} \tag{B.11}$$

Combining equations (3.11.) and (3.16.), after mathematical manipulations, the friction coefficient becomes

$$\left(f \cdot Re_{D_h}\right) = \left(\frac{\Delta p}{L} \cdot D_h \cdot \frac{2}{\rho \cdot u_m^2}\right) \cdot \left(\frac{\rho \cdot u_m \cdot D_h}{\mu}\right) = \cdots = \frac{\Delta p}{L} \cdot \frac{8}{\mu \cdot \dot{V}} \cdot \frac{H^3 \cdot W^3}{(H+W)^2} \qquad \text{(B.12)}$$

Assuming no uncertainty associated with measuring the channel width, *W*, from equations (B.11) and (B.12) it can be inferred that

$$Re_{D_h} = \text{function}\left(\rho, \dot{V}, \frac{1}{\mu}, \frac{1}{H}\right) \quad \text{and} \quad \left(f \cdot Re_{D_h}\right) = \text{function}\left(\frac{\Delta p}{L}, \frac{1}{\mu}, \frac{1}{\dot{V}}, H^3\right)$$

and, therefore

$$\frac{\omega_{Re_{D_h}}}{Re_{D_h}} = \left[\left(\frac{\omega_\rho}{\rho}\right)^2 + \left(\frac{\omega_{\dot{V}}}{\dot{V}}\right)^2 + \left(\frac{\omega_\mu}{\mu}\right)^2 + \left(\frac{\omega_H}{H}\right)^2\right]^{\frac{1}{2}} \qquad \text{(B.13)}$$

$$\frac{\omega_{(f \cdot Re_{D_h})}}{(f \cdot Re_{D_h})} = \left[\left(\frac{\omega_{\Delta p/L}}{\Delta p/L}\right)^2 + \left(\frac{\omega_\mu}{\mu}\right)^2 + \left(\frac{\omega_{\dot{V}}}{\dot{V}}\right)^2 + \left(\frac{3 \cdot \omega_H}{H}\right)^2\right]^{\frac{1}{2}} \qquad \text{(B.14)}$$

Mean channel depths and uncertainties in the mean (at the 95% confidence level) are listed in Table B.1, together with the standard deviations of particular measurements. In general, the mean channel depth was measured within ± 5 to 8 μm, depending on the configuration.

Table B.1. Channel depth measurement and uncertainty

Spacer Thickness, [μm]	Bottom Plate, [surface]	Mean Depth, [μm]	Standard Deviation, [μm]
508	Smooth	521 ± 8	16.8
254	Smooth	263 ± 8	15.8
254	Rough	257 ± 7	14.5
128	Smooth	128 ± 5	9.9

For 128-μm smooth bottom surface, there were two sets of measurements performed with different flow meters. Table B.2 presents average values and uncertainty levels associated with measured and computed values.

Table B.2. Uncertainty levels associated with flow measurements for 128-μm channel

	Units	Average	Uncertainty	Average	Uncertainty
Height	[cm]	0.0128	$2.327 \cdot 10^{-4}$	0.0128	$2.327 \cdot 10^{-4}$
Flow rate	[ml/min]	100.0000	1.469	15.0000	0.235
Density	[g/cm^3]	0.9975	$1.200 \cdot 10^{-4}$	0.9973	$1.200 \cdot 10^{-4}$
Viscosity	[cp]	0.9381	$1.227 \cdot 10^{-2}$	0.9141	$1.256 \cdot 10^{-2}$
Δp/L	[psi/cm]	1.5416	$2.794 \cdot 10^{-3}$	0.2104	$3.237 \cdot 10^{-4}$
Re	[-]	350.0026	5.770	53.8637	0.429
$(f \cdot Re_{D_h})$	[-]	111.3204	6.295	103.9340	5.710

Table B.3 presents average values and uncertainty levels associated with measured and computed values for the middle-size channel, for which both smooth and rough surface were used.

Table B.3. Uncertainty levels associated with flow measurements for mid size channel

	Units	Average	Uncertainty	Average	Uncertainty
Height	[cm]	0.0263	$3.728 \cdot 10^{-4}$	0.0257	$3.433 \cdot 10^{-4}$
Flow rate	[ml/min]	100.0000	1.469	100.0000	1.469
Density	[g/cm^3]	0.9977	$1.200 \cdot 10^{-4}$	0.9973	$1.200 \cdot 10^{-4}$
Viscosity	[cp]	0.9628	$1.268 \cdot 10^{-2}$	0.9628	$1.268 \cdot 10^{-2}$
Δp/L	[psi/cm]	0.1761	$1.443 \cdot 10^{-4}$	0.2110	$1.163 \cdot 10^{-4}$
Re	[-]	366.5542	5.573	336.7790	5.552
$(f \cdot Re_{D_h})$	[-]	104.6296	4.707	117.0948	5.008

Average values and uncertainty levels associated with measured and computed values for the 521-μm channel are presented in Table B.4.

Table B.4. Uncertainty levels associated with flow measurements for 521 μm channel

	Units	Average	Uncertainty
Height	[cm]	0.0521	$3.955 \cdot 10^{-4}$
Flow rate	[ml/min]	100.0000	1.469
Density	[g/cm^3]	0.9977	$1.200 \cdot 10^{-4}$
Viscosity	[cp]	0.9503	$1.248 \cdot 10^{-2}$
Δp/L	[psi/cm]	0.0217	$5.580 \cdot 10^{-5}$
Re	[-]	332.6378	5.500
$(f \cdot Re_{D_h})$	[-]	96.7546	2.679

B.3 Heat transfer measurements

The uncertainty analysis for heat transfer data used results from fluid flow data analysis, and new variables with associated uncertainty levels. From equation (3.35), after mathematical manipulations, it follows

$$Nu_x = \frac{\left(q''/\Delta t\right)\cdot D_h}{k} = \frac{\left(q/A_{HX}\right)\cdot D_h}{k\cdot\Delta T} = \cdots = \frac{2}{k\cdot A_{HX}}\cdot\frac{U^2}{R}\cdot\frac{1}{\Delta t}\cdot\frac{H\cdot W}{(H+W)} \qquad \text{(B.15)}$$

Heater dimensions were measured with the same instrument, such that the uncertainty associated with heater area can be related to a length measurement

$$Nu_x = \text{function}\left(\frac{1}{k}, \frac{1}{(L_{HX})^2}, U^2, \frac{1}{R}, \frac{1}{\Delta t}, H\right) \qquad \text{(B.16)}$$

Thermal conductivity, k, and electrical resistance, R, are temperature dependent variables, and therefore, the associated uncertainty will be

$$\omega_k = \sqrt{\left(\omega_{t_{calibration}}\right)^2 + \left(\omega_{k_{curve-fit}}\right)^2} \quad \text{and} \quad \omega_R = \sqrt{\left(\omega_{t_{calibration}}\right)^2 + \left(\omega_{R_{curve-fit}}\right)^2}$$

The levels of uncertainty associated with temperatures measured with RTD probes are subject to uncertainties in calibration standard, curve-fitting, and actual measurements. The RTDs were calibrated by flowing two-phase fluid through the test section, measuring the pressure, and then assessing the temperature from fluid properties table. There is an uncertainty level associated with pressure measurement that propagates to the uncertainty level of indicated temperature. Also, there is an uncertainty level associated with curve fit for the calibration, as well as one associated with the actual measurement. Therefore, the uncertainty levels in temperature measurement were computed separately for each RTD in the form

$$\omega_t = \sqrt{\left(\omega_{t_{calibration}}\right)^2 + \left(\omega_{t_{curve-fit}}\right)^2 + \left(\omega_{t_{measurement}}\right)^2} \tag{B.17}$$

The calibration term has the largest contribution to the final result. Relative uncertainty in Nusselt number becomes

$$\frac{\omega_{Nu_x}}{Nu_x} = \left[\left(\frac{\omega_k}{k}\right)^2 + \left(\frac{\omega_R}{R}\right)^2 + \left(\frac{\omega_H}{H}\right)^2 + \left(\frac{2\cdot\omega_U}{U}\right)^2 + \left(\frac{2\cdot\omega_{L_{HX}}}{L_{HX}}\right)^2 + 2\cdot\left(\frac{\omega_t}{t}\right)^2\right]^{\frac{1}{2}} \tag{B.18}$$

Table B.5. Uncertainties associated with heat measurements for 128 μm channel

	Units	Average	Uncertainty
Temperature	[°C]	11.16 – 33.53	0.728 – 0.732
Voltage	[V]	10.16 – 10.80	$1.1\cdot10^{-3} - 1.6\cdot10^{-3}$
Electrical resistance	[Ω]	103.75 – 111.43	0.99 – 1.19
Thermal conductivity	[W/mK]	0.082 – 0.085	$7.2\cdot10^{-4} - 2.0\cdot10^{-3}$
Height	[mm]	0.128	0.005
Length (for A_{HX})	[mm]	10.000	0.001
Nusselt number	[-]	4.258 – 8.303	0.248 – 0.579

Table B.6. Uncertainties associated with heat measurements for 263 μm channel

	Units	Average	Uncertainty
Temperature	[°C]	11.05 – 41.28	0.735 – 0.739
Voltage	[V]	10.26 – 10.73	$9.4 \cdot 10^{-4} - 2.7 \cdot 10^{-3}$
Electrical resistance	[Ω]	103.75 – 111.43	0.14 – 0.15
Thermal conductivity	[W/mK]	0.081 – 0.085	$7.2 \cdot 10^{-4} - 2.0 \cdot 10^{-3}$
Height	[mm]	0.263	0.010
Length (for A_{HX})	[mm]	10.000	0.001
Nusselt number	[-]	4.258 – 8.303	0.298 – 0.795

Table B.7. Uncertainties associated with heat measurements for 521 μm channel

	Units	Average	Uncertainty
Temperature	[°C]	11.68 – 38.65	0.453 – 0.459
Voltage	[V]	10.24 – 10.74	$1.1 \cdot 10^{-3} - 1.7 \cdot 10^{-3}$
Electrical resistance	[Ω]	103.90 – 111.43	0.091 – 0.096
Thermal conductivity	[W/mK]	0.084 – 0.085	$6.2 \cdot 10^{-4} - 1.1 \cdot 10^{-3}$
Height	[mm]	0.521	0.008
Length (for A_{HX})	[mm]	10.000	0.001
Nusselt number	[-]	5.831 – 8.001	0.238 – 0.611

APPENDIX C. DIMENSIONAL DATA – TEST SECTION

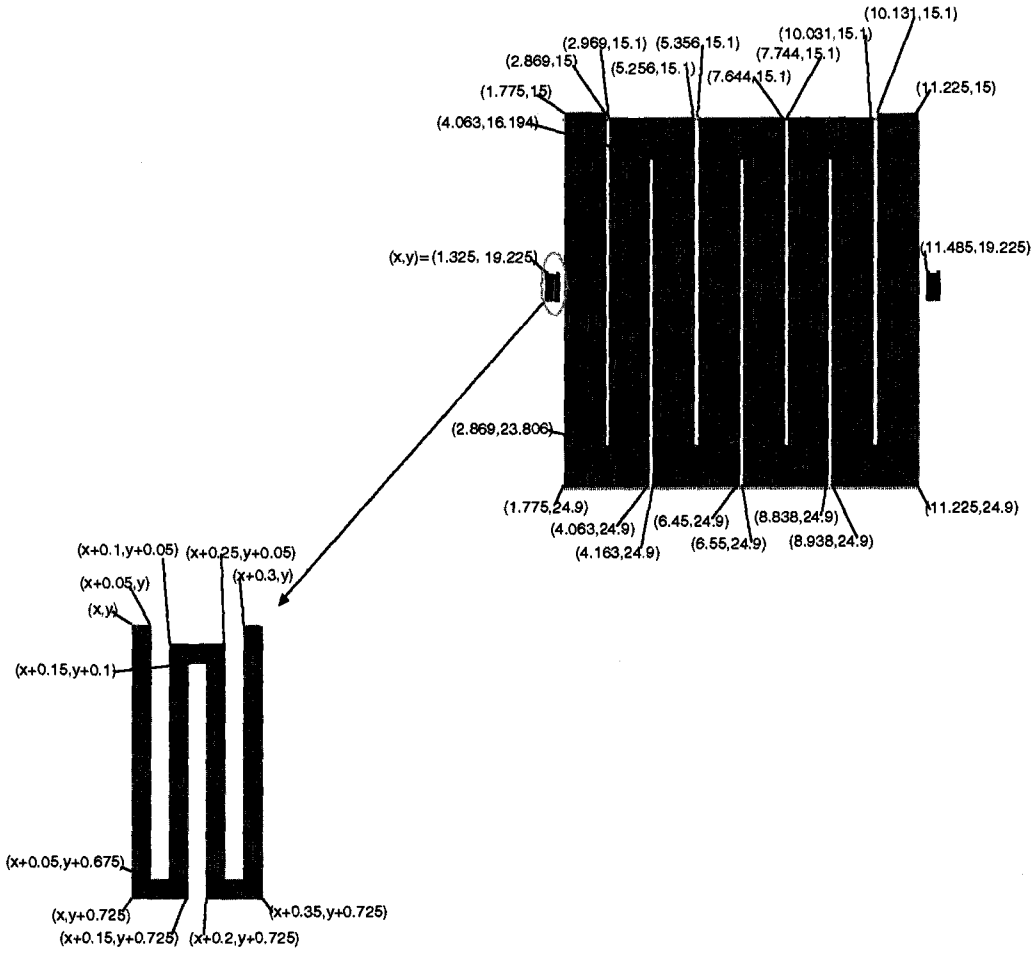

Figure C.1. Dimensional details of heater and RTD sensing element

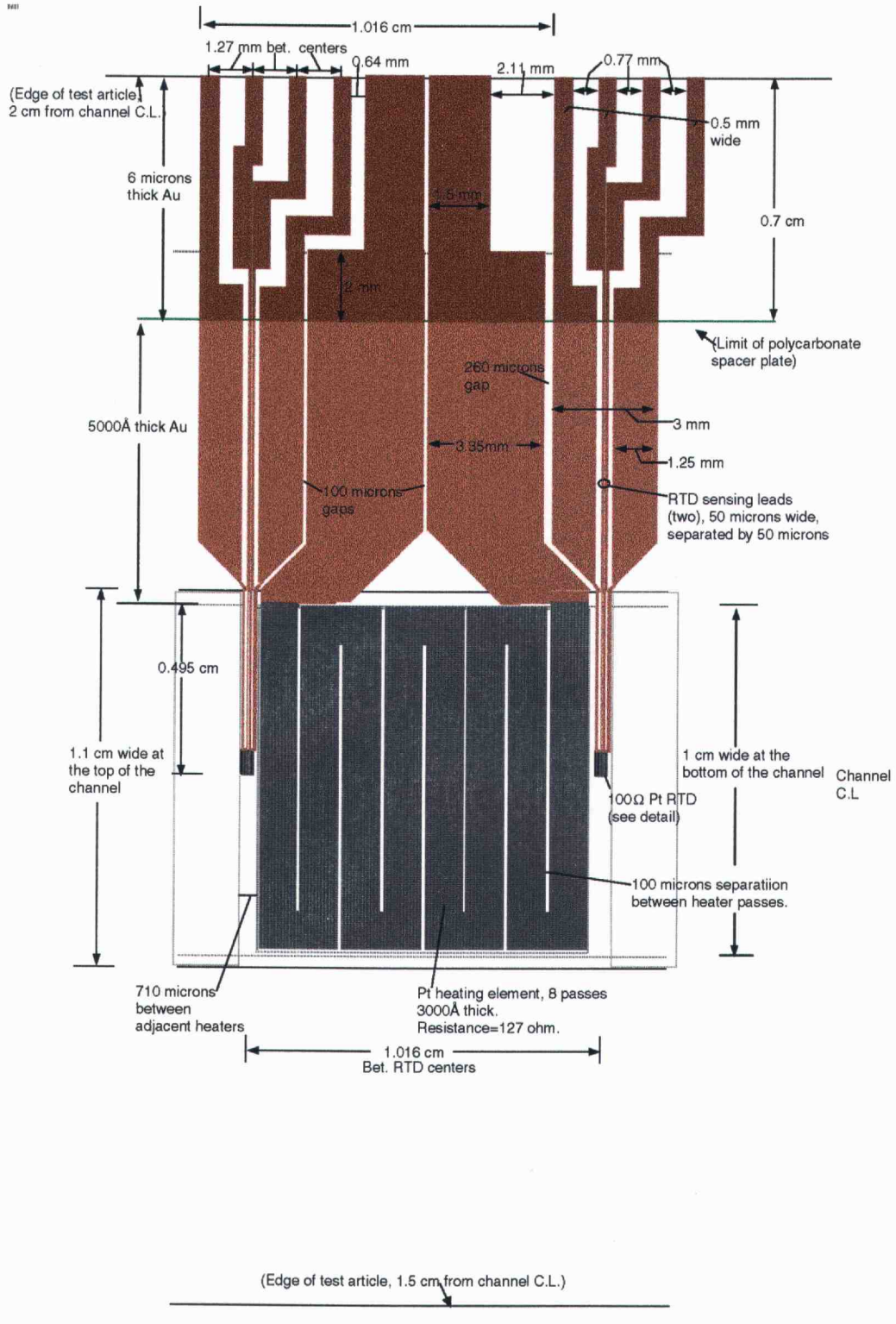

Figure C. 2. Dimensional details of heater and RTDs with leads

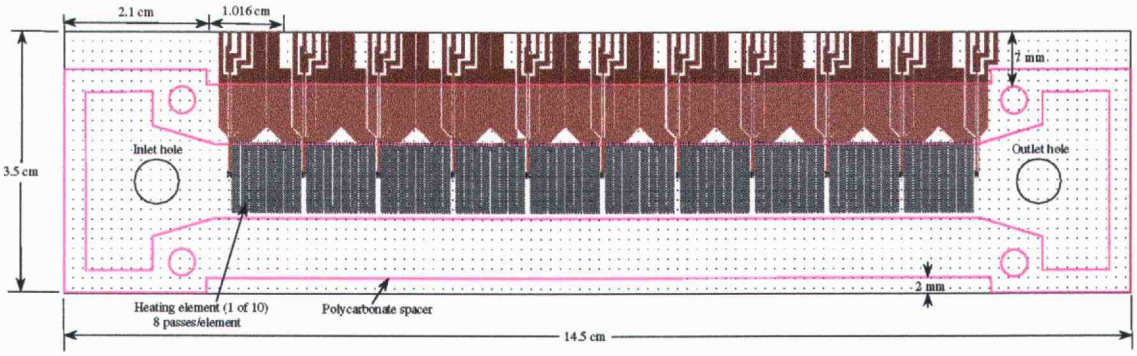

Figure C. 3. Dimensional details of heater plate and spacer

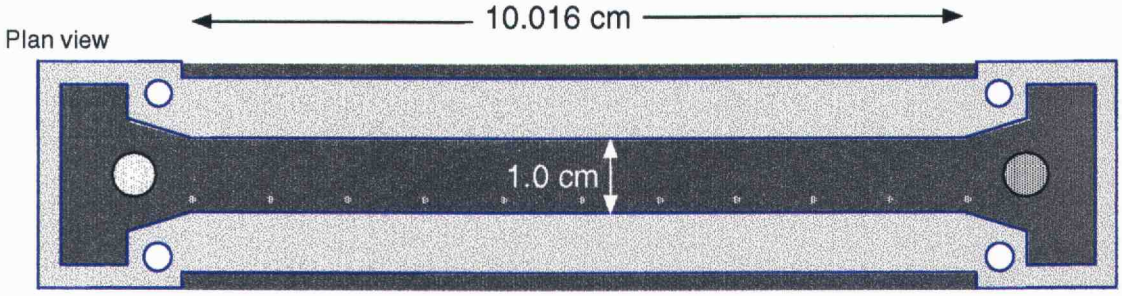

Figure C. 4. Dimensional details of the channel

APPENDIX D. NUMERICAL CODE

The MATLAB code "*ht_hx.m*" computes the temperature profile on the vertical mid-plane along the channel for the specified input conditions. This version of the code takes into account the actual heating mode according the geometric features of heaters.

```
clear all
format short;


%GLOBAL VARIABLES

global h to Vdot W;


% INPUT DATA

W      = 10;                    %Width of Channel          [mm]
L      = 102;                   %Length of Channel         [mm]
H      = 0.13;                  %Height of channel         [mm]
to     = 10;                    %inlet temperature         [°C]
qi     = 1.152;                 %power input               [W/cm^2]
Vdot   = 0.335;                 %volumetric flow rate      [cc/s]

nu     = 1.812*10^(-7);         %dynamic viscosity         [m2/s]

NoX = 10;                       %(# nodes in X-direction)/(50 um))
NoY = 10;                       %(# nodes in Y-direction)/(50 um))

dx = 50/(1000*NoX);
dy = 50/(1000*NoY);
b = dx/dy;

Vdot = Vdot*10^3;
qo = qi/10^2;


% MATRICES INITIALIZATION

I = (L/dx) + 3;                 %# nodes in X- direction
J = (h/dy) + 1;                 %# nodes in Y- direction

u = zeros(I,J);
v = zeros(I,J);
t = to*ones(I,J);

```

```
for j = 1:J
  u(:,j) = Uin((j-1)*dy);                          %velocity profile from "Uin" function
end

tk = t;
err = 100; count = 0;


% MAIN LOOP

tic
while err > 0

  count = count+1

  rho = (-0.00853*(t.^2) - 3.03852*t + 1437.79)/10^9;%density                [kg/mm^3]
  cp  = (1.44368e-2)*(t.^2) +2.12719*t + 1058.18;    %specific heat          [J/kg K]
  kfl = (2.68315e-11)*(t.^2) - (3.57389e-7)*t + (9.01388e-5); %thermal conductivity, [W/mm K]
  alf = kfl./(rho.*cp);                            %thermal diffusivity    [mm^2/s]

  j = 1;
  for i = 2:I
    tk(i,j) = (2*dy*semn((i-1)*dx)*qo/kfl(i,j) + 4*t(i,j+1) - t(i,j+2))/3;
  end

  for i = 1:I-1
    tk(i+1,2:J-1) = tk(i,2:J-1) + (alf(i,2:J-1)*b*b./(dx*u(i,2:J-1)))...
      .*(tk(i,3:J) - 2*tk(i,2:J-1) + tk(i,1:J-2));
  end

  tk(2:I,J) = (4*tk(2:I,J-1) - tk(2:I,J-2))/3;

    ET = abs((tk - t)./tk);                        %Update the error matrix

  if all (ET < 0.0002)                             %Compare errors for each node
    err = 0;
  else
    err = 1;
  end

  t = tk;

end
toc

spa = num2str(h*1000);
flo = num2str(round((Vdot*6)/100));
hea = num2str(qo*10000);
file_t = cat(2,'save c:/th_',spa,'_',flo,'_',hea,'.txt t -ascii -tabs')

surf(t,'EdgeColor','none')
```

For the cases modeling ideal uniform heating, the function "*semn*" in line 63 is re-written as another function, "*semn_unif*", or to reduce the computational time (each time the function is called), several extra lines can replace line 63:

```
x = (i-1)*dx;
if and(x >= 10.16, x <= 91.43)
  s = 1;
else
  s = 0;
end
tk(i,j) = (2*dy*s*qo/kfl(i,j) + 4*t(i,j+1) - t(i,j+2))/3;
```

The user-defined functions in lines 42 (*Uin*) and 63 (*semn*) are listed below:

```
function [U] = Uin(y)

% This function returns the velocity of the flow as a function of cross-stream position.

global h to Vdot W;

if and(y >= 0, y <= h)
  U = (6*Vdot/(W*h^2))*(y - y^2/h);
else
  U = 0;
end
```

```
function [s] = semn(x)

% This function returns the sign for heating input at bottom of the channel as a function of position

global h Vdot W;

if x > 10.16 & x < 91.44
  x = x - 10.16*floor(x/10.16);
  if x <= 9.42
    if x - 1.19*floor(x/1.19) <= 1.09
      s = 1;
    else
      s = 0;
    end
  else
    s = 0;
  end
else
  s = 0;
end
```

The second part of the code (*nu_hx.m*) is using the temperature profile previously determined, computes the mean fluid temperature at each location along the *x*-axis, and then the local values of the Nusselt number.

```
clear
format short;


% INPUT DATA

W           = 10;                                   %Width of Channel       [mm]
L           = 102;                                  %Length of Channel      [mm]
H           = 0.13;                                 %Height of channel      [mm]
to          = 10;                                   %inlet temperature      [°C]
Vd          = 0.335;                                %volumetric flow rate   [cc/s]
qi          = 1.152;                                %power input            [W/cm^2]


%READ TEMPERATURE PROFILE

dx = 0.005; dy = 0.005;
b = dx/dy;
[t] = textread('t_130_20_1152.txt', '%f', -1);
tfl = reshape(t, h/dy+1, L/dx+3);
tw  = tfl(1,☺);


%RE-SHAPE MATRICES

n = size(tfl,1) – 1;
m = size(tfl,2);
odev = abs(n/2 – round(n/2));
Dh = 2*W*h/(W+h);
rez = [];
Vdot = Vd*10^3;
qo   = qi/10^2;


%FLUID PROPERTIES (TEMPERATURE DEPENDENT)

rho = (-0.00853*(tfl.^2) – 3.03852*tfl + 1437.79)/10^9;          %density                [kg/mm^3]
cp  = (1.44368e-2)*(tfl.^2) +2.12719*tfl + 1058.18;              %specific heat          [J/kg K]
kfl = (2.68315e-11)*(tfl.^2) – (3.57389e-7)*tfl + (9.01388e-5);%thermal conductivity [W/mm K]
alf = kfl./(rho.*cp);                                            %thermal diffusivity,   [mm^2/s]
mu  = (1.71287e-11)*(tfl.^2) – (3.83854e-9)*tfl + (3.45822e-7);%kinematic viscosity  [kg/mm s]
nu  = mu./rho;                                                   %dynamic viscosity     [mm^2/s]
Rex = (Vdot*Dh/(W*h))./mean(nu);
Prx = mean(nu)./mean(alf);

num = mean(nu); alfm = mean(alf); rom = mean(rho); cpm = mean(cp); kflm = mean(kfl);
Rem = (Vdot*Dh/(W*h))/mean(num)
Prm = mean(num)/mean(alfm)

```

```
50
51  %MAIN LOOP
52
53  if odev == 0
54    for j = 1:m
55      sum = 0;
56      sum = tfl(1,j) + 4*tfl(2,j) + tfl(n+1,j);
57
58      for i = 3:2:n-1
59        sum = sum + 2*tfl(i,j) + 4*tfl(i+1,j);
60      end
61
62      tflm(j) = sum*dy/(3*h);
63    end
64
65    tf = (tw + tflm)/2;
66    kflf = (2.68315e-11)*(tf.^2) - (3.57389e-7)*tf + (9.01388e-5);
67
68    for j = 1:m
69      if semn((j-1)*dx) == 0
70        nuss(j) = 0;
71      else
72        nuss(j) = qo*Dh/((tw(j) - tflm(j))*kflf(j));
73      end
74      rez = [rez; [tw(j) tflm(j) nuss(j)]];
75    end
76  else
77    for j = 1:m
78      sum = 0;
79      sum = tfl(1,j) + 3*tfl(2,j) + 3*tfl(3,j) + tfl(4,j);
80      area1 = 3*sum*dy/8;
81      sum = tfl(4,j) + 4*tfl(5,j) + tfl(n+1,j);
82
83      for i = 6:2:n-1
84        sum = sum + 2*tfl(i,j) + 4*tfl(i+1,j);
85      end
86      area2 = sum*dy/3;
87
88      tflm(j) = (area1+area2)/h;
89    end
90
91    tf = (tw + tflm)/2;
92    kflf = (2.68315e-11)*(tf.^2) - (3.57389e-7)*tf + (9.01388e-5);
93
94    for j = 1:m
95      if semn((j-1)*dx) == 0
96        nuss(j) = 0;
97      else
98        nuss(j) = qo*Dh/((tw(j) - tflm(j))*kflf(j));
99      end
100     rez = [rez; [tw(j) tflm(j) nuss(j)]];
101   end
102 end
103
```

```
104
105  %RESULTS PRESENTATION / SAVING
106
107  kave = (max(kflf)+min(kflf))/2
108  temper = [max(tw) max(tflm) max(tf)]
109  dtemp = tw - tflm;
110
111  X = [0:dx:(m-1)*dx];
112  XP = 2*X/(Rem*Prm*Dh);
113  Y = [0:dy:n*dy];
114
115  figure(1)
116    surf(X,Y,tfl,'EdgeColor','none')
117    xlabel('L [mm]'); ylabel('H [mm]'); zlabel('Temperature, T [°C]')
118    title('\fontsize{12} Temperature field')
119
120  figure(2)
121            plot(XP,tw,'r',XP,tflm,'b'); grid on
122            title('\fontsize{14} Wall temperature and Mean fluid temperature')
123            xlabel('\fontsize{12} x^+'); ylabel('\fontsize{12} Temperature, T [°C]')
124
125  figure(3)
126            plot(XP,nuss,'.r'); grid on
127            axis([0 max(XP) 0 40])
128            title('\fontsize{14} Variation of local Nusselt number')
129            xlabel('\fontsize{12} x^+'); ylabel('\fontsize{12} Nu_x')
130
131  figure(4)
132            plot(XP,dtemp,'k'); grid on
133            title('\fontsize{14} Temperature difference, \DeltaT = T_w - T_f_l_m')
134            xlabel('\fontsize{12} x^+'); ylabel('\fontsize{12} Temperature, T [°C]')
135
136
137  spa = num2str(h*1000);
138  flo = num2str(round((Vdot*6)/100));
139  hea = num2str(qo*100000);
140  file_ts = cat(2,'save h:/rezu_',spa,'_',flo,'_',hea,'.txt rez -ascii -tabs')
```

The function "*semn*" has to be changed in both lines 69 and 95 with function "*semn_unif*".

```
function [s] = semn_unif(x)

% This function returns the sign for uniform heating input at bottom of the channel as a function
% of position

global h Vdot W;

if and(x >= 10.16, x <= 91.43)
  s = 1;
else
  s = 0;
end
```